Politecnico di Milano

SCHOOL OF INDUSTRIAL AND INFORMATION ENGINEERING
Master of Science in Energy Engineering

Master Thesis

Influence of clouds passing on the dynamic thermal performances of a tower receiver with heat storage system

Supervisors
Prof. Giampaolo Manzolini
Prof. David Sanchéz Martinéz

Student
Andrea Toscani
ID n.836718

Anno Accademico 2015–2016

Politecnico di Milano:
www.polimi.it

School of industrial and information engineering:
www.ingindinf.polimi.it

Ringraziamenti e dedica

In un momento così importante della mia vita è giusto fermarmi, fare un bel respiro e analizzare, passo dopo passo, il percorso che mi ha portato fino a qui. Chiudendo gli occhi quasi non mi riconosco più in quel bambino che al primo giorno di università non sapeva come affrontare la montagna impervia che si trovava di fronte a sè. Ora 3 città, 5 anni e 300 crediti dopo vedo un ragazzo felice e soddisfatto che, nonostante le mille difficoltà, rifarebbe ogni passo di questo lungo e faticoso percorso universitario. Si, perchè solo alla fine ci si accorge quanto il "Poli" sappia donarti da un punto di vista formativo ed umano.

Tutto ciò non sarebbe stato però possibile senza l'amore incondizionato della mia famiglia e di Rachele. A loro dedico questo mio lavoro di tesi e li ringrazio in primis per il loro fondamentale aiuto in tutti questi anni.

In particolare ringrazio i miei genitori, Paola e Fabio, per avermi dato la possibilità di intraprendere la carriera universitaria e per avermi supportato (o sopportato?!) incondizionatamente fin da piccolo nonostante i miei momenti no. Il loro esempio rimarrà sempre nel mio cuore e per questo, a loro dedico i frutti che spero otterrò da questi anni di duro lavoro. Allo stesso modo ringrazio Rachele, la mia ragazza, per il suo affetto, il suo supporto emotivo e la sua presenza solare, elementi constanti in questi anni difficili. Nononostante le varie sessioni d'esame, le mie ansie e le mie preoccupazioni mi è sempre stata accanto, spronandomi a dare il meglio di me, anche se ciò significasse sacrificare alcuni momenti insieme per lasciare spazio allo studio. Senza di lei non sarei qui ora. Una menzione particolare per mio fratello Luca, il cui esempio è sempre stato di riferimento fin dalla mia infanzia. A lui vanno i miei migliori auguri per l'importante passo che si accinge a compiere con Valentina.

Desidero inoltre ringraziare per l'affetto dimostrato in tutti questi anni gli altri componenti della mia famiglia: Nonna Romea, Zia Renata, Zio Antonio e Alessandra.

Un ringraziamento speciale va al mio relatore, il professor Giampaolo Manzolini, la cui cortesia e disponibilità ha permesso lo sviluppo di questo lavoro. Lo vorrei ringraziare particolarmente per la fiducia ed il supporto dimostratimi a distanza, fondamentali per motivarmi e fornirmi gli spunti giusti per condurre al meglio quest'analisi. Allo stesso modo vorrei ringraziare il professor David Sanchéz per avermi ospitato all'interno della *Universidad de Sevilla* e per la disponibilità dimostratami in ogni momento di difficoltà. La sua preparazione e i suoi consigli sono stati determinanti per il buon esito di questo lavoro di tesi.

All'interno del *Grupo de Maquinas y Motores Termicos de Sevilla* un grazie di cuore è rivolto a Francesco e José Maria. Li vorrei ringraziare in particolare per il

loro aiuto quotidiano, per i mille consigli che hanno saputo donarmi e per la capacità di rincuorarmi nei momenti di difficoltà. Senza di loro non ce l'avrei mai fatta a realizzare questo difficile lavoro.

Vorrei ringraziare inoltre il professor Luigi Colombo, la cui gentilezza e disponibilità risultò fondamentale in un momento di sconforto dovuto alle difficoltà tecniche.

Numerossime sono poi le persone che meriterebbero una citazione particolare in questa sezione. Nuovi amici, amici di sempre, tutte persone fantastiche che ho avuto il piacere di conoscere e con cui spero di poter condividere molte altre esperienze di vita. Perchè nulla sarebbe uguale senza di loro.

Moira che sicuramente starà già piangendo. Un grazie di cuore a lei, senza dubbio la mia migliore amica, per ogni chiacchierata (o meglio definibile "spetegules"), passeggiata, consiglio, risata (vogliamo parlare di lacrime?!) e qualsiasi altra cosa che abbiamo condiviso insieme in tutti questi anni di sincera amicizia.

Paolo, Paolo e Filippo per aver allietato questi anni difficili con sane risate e serate indimenticabili. Alcuni momenti passati con loro rimarrano indelebili nella mia memoria. Con loro identifico poi i cestisti del gruppo "L'importante è ..." perchè ad elencarli tutti sarebbe impossibile.

Alvaro (o Alvarello?!?), perchè senza di lui Siviglia non sarebbe mai stata la stessa cosa per me. Grazie per avermi accolto nella sua famiglia, aprendomi il suo mondo come mai nessun'altro aveva fatto. Giorno dopo giorno ho scoperto in lui un secondo fratello.

Daniele ed Enrico, due "regali" che l'esperienza universitaria ha saputo donarmi. Grazie di cuore per ogni sorriso, ogni risata e le innumerevoli gioie condivise nel corso dei vari semestri. Spero vivamente che, nonostante la distanza e le diverse scelte di vita che ci accingiamo a compiere, la nostra amicizia possa essere solo all'inizio di un lungo cammino insieme.

Michele, Emanuele, Simone, Camilla, Francesco, Stefano, Ettore, Nicola, Irene, Eleonora, Matteo, Giulio, Luca e tutti gli altri amici dell'università. A loro è rivolto un grazie sincero e consapevole, perchè la loro presenza ha sempre addolcito i momenti difficili e la loro amicizia ha dato un significato speciale alla mia esperienza universitaria, riuscendo nell' impossibile missione di colorare il grigiume della Bovisa.

Tommaso, Michele, Andrea, Martina, Silvia, Andrea, Alberto, Andrea e tutti gli amici di sempre. Nonostante con alcuni mi sia perso un pò di vista è impossibile dimenticare la loro importanza all'interno del mio percorso di crescita.

Borja, Lucas, Jesùs, Rafa, Claudia, Trini, Paola, Isabel, Noelia, Ana, Pilar, Leandro, Amelia, Gonzalo e Cristina. Ultimi, ma non per importanza, vorrei citare gli amici, i coinquilini e i colleghi che ho avuto il piacere di conoscere negli ultimi sette mesi a Siviglia. Un grazie sincero per aver arricchito in maniera speciale la mia esperienza in Andalusia.

Siviglia, Aprile 2017 Andrea

"Sky is the limit"

Extended Abstract

Starting from the last decade RES (Renewable Energy Sources) exploitation has been strongly introduced in the energy market. Principally in Europe, the attention was in fact focused on reducing pollution emissions, especially carbon dioxide (CO_2), imposing eco-friendly regulating rules in a wider scenario of a renovated environmental policy.

The main issue related to renewable sources and to their diffusion on a large-scale on the energy market is their unpredictability. Due to their characteristic fluctuations, mainly depending on the weather conditions for solar and wind technologies, they introduce instability and uncertainty in the energy system. This increases the need for regulation and reserves in orders to manage the electrical grid with security and stability for the transmission and distribution system operators. These characteristics impose energy backups usually provided by conventional technologies constituting the main reason for the inability of a complete switch towards renewable energy sources exploitation. In this context, the application of storage systems to renewable sources is likely to be the most reliable solution in order to smooth their fluctuations of power produced, making the management and operation of the electrical network easier. In particular, from a solar power plant perspective, the most suitable solution is the application of a thermal storage system in which energy is conserved through an hot fluid accumulation. This fluid could be directly expanded in a turbine for electric energy generation or it can be used as a thermal medium to warm up another fluid (usually water-steam). In the latter case, the power plant is subdivided in two main circuits and the power block is linked to the receiver through an heat exchanger.

On this matter, the present work proposes a thermodynamic model of an existing CSP plant characterised by two huge tanks used as heat storage systems. In particular, attention is hereby focused on the Gemasolar Power Plant, property of the society *Torresol Energy Investments*.

The plant, located in Fuente de Andalucia close to Seville (Spain), can rely on perfect weather and radiation conditions for the thermal energy exploitation and represents an interesting case for the investigation. The main aim of this dissertation is to provide a tool for the plant performances simulation in both steady and transient conditions that will be useful for further investigations regarding for instance thermal and stress issues.

The source code used for the simulation has been autonomously filled up using the software Matlab as compiler. As starting point, data regarding radiation

conditions and clouds modelling have been taken from two previous thesis works (De Giorgi and Crespi-Zani) that focused their attention on the same Gemasolar power plant. In particular the main input is constituted by a radiation map changing in time according to different clouds model available. The theoretical basis of the whole dissertation is represented by a time-scale analysis of the main element of the plant. In fact, through the investigation on both the capacity and the process rate parameters it was possible to determine the intrinsic inertia and the characteristic response time for each of the main thermal and mechanical processes that occurs in the power plant with respect to the considered time-frame of a cloud passage.

Once demonstrated that in case of heat storage system the power block can be decoupled from the thermal fluid circuit, attention was focused on the solar receiver. In this regard, the receiver geometry was characterised by available information from literature and suitable design assumptions, later on verified from a fluid perspective considering the safe working conditions limits. In this regard, particular attention has been paid in order to avoid degradation ($T > 600°C$) and solidification ($T < 290°C$) problems, conditions for which the molten salts loss their thermal properties compromising the system stability.

Successively the receiver stationary model was designed according to the thermal equilibrium in both axial and tangential direction for each of the flux units in which all the receiver pipes were subdivided. An overall receiver system constituted by 4032 flux units has been developed with the final aim of a good accuracy. In this regard, the overall receiver system was simulated as an 18 panels series, each of them characterised by 24 parallel pipes. Each pipe was further subdivided in 28 axial and 8 circumferential flux units. According to the radiation map discretisation, only one pipes for each panel has been considered for the thermal balance. In this way, an equivalent circuit was built linking all the considered pipes from inlet to outlet section, simplifying the global structure complexity.

Furthermore, particular attention was paid to the code modelling because more than one parameters was initially unknown requiring, as a consequence, different iterative cycles in order to obtain the solution of the problem with a fluid production rate in compliance with respect to the desired temperatures conditions.

Afterwards, the stationary model was used to analyse different solar field aiming strategies confirming Crespi-Zani results also from a receiver thermal efficiency perspective. Aiming strategy 6 is in fact demonstrated to assure lowest peak radiation values but also a 2% higher receiver thermal efficiency and a 1% greater molten salts production rate (423 vs 420 kg/s) with respect to the second best strategy. As a consequence, the former has been selected as the best strategy for the solar field setting and it has been kept as default in the following analyses.

In a later stage, the stationary solution was considered as the starting condition for the further transient model development. In this regard, a preliminary heat capacity analysis, showed the possibility of simplify the system considering transient performances only for the molten salts assuming pipe wall surface in quasi-steady state conditions. This strong assumption has been considered in order to reduce the

computational cost required for the solution of the differential equations system. In this regards, Matlab PDEPE function was used as tool for the solution of the fluid energy equation in dynamic conditions.

$$\frac{\partial(\rho_f \cdot Cp_f \cdot T_f)}{\partial t} + \frac{\partial}{\partial x}(\rho_f \cdot Cp_f \cdot \overrightarrow{v} \cdot T_f) = \frac{\partial}{\partial x}\left(k_f \cdot \frac{\partial T_f}{\partial x}\right) + h_{conv} \cdot (T_{wall} - T_f) \quad (1)$$

Furthermore, the developed tool provides the possibility to incorporate two different control schemes: feed-back control whereby the volumetric flow rate of molten salts is controlled by the receiver outlet temperature, and feed-forward control whereby the flow of salts depends on lookup tables calculated a priori. A further detailed analysis led through the demonstration of the former as the best strategy for the system controlling, optimizing the receiver performances guaranteeing a 25% temperature gradient reduction and lowering degradation risk by a 4.2% outlet temperature decrease.

Exploiting the tool potential, the controller has been tested according to the system response with respect to 70% and 100% steps perturbation in the incoming radiation . In a later stage, a clouds comparison has been proposed in order to understand how different weather conditions affect the system stability from both a thermal and dynamic perspective.

The next step was the power block modelling in nominal working conditions. Gemasolar power block is modelled as SH+RH Rankine cycle in which steam expansion is subdivided in a high and low pressure steam turbine. Steam evaporation and superheating are assured by the amount of heat provided by the molten salts in a three section heat exchanger.

After the complete behaviour definition for all of the power plant portions according to the characteristics energy balances, the various models were linked together according to the plant characteristics and complex scenarios were simulated to analyse the overall system performances. In particular, morning start-up process has been simulated using seven different radiation maps from 6.30 am to 12 am. Finally, two general conditions has been test: the hot tank charge and discharge processes respectively in case of a spring sunny day and a winter cloudy one.

In conclusion, considerations have been done regarding the importance of the heat storage system as the state of the art technology from a solar energy exploitation perspective. Possible tool improvements has been recommended in order to achieve a higher accuracy level. Finally, future works based on the present tool have been proposed in order to investigate additional developments that would push this technology to make a further step and gain importance in the global energy scenario.

Sommario Esteso

La rapida diffusione delle fonti di energia rinnovabile (RES), eccezione fatta per l'idroelettrico, ha avuto inizio al principio dello scorso decennio e ha riguardato principalmente i paesi europei. Da questo punto di vista, il Vecchio Continente si è fatto promotore di una nuova politica ambientale volta alla riduzione dello sfruttamento delle fonti convenzionali con l'obiettivo principale di limitare l'emissione di sostanze inquinanti e di anidride carbonica.

Il maggior problema legato ad un massiccio impiego delle fonti rinnovabili è rappresentato tuttavia dalla difficoltà nel prevederne il profilo di potenza prodotta. Queste tecnologie sono infatti fortemente legate alle condizioni atmosferiche (in particolare il solare e l'eolico), che costituiscono una fonte di notevole variabilità per la produzione energetica e causano quindi indirettamente instabilità nella rete elettrica dovute ad un profilo di potenza immessa soggetto ad importanti fluttuazioni. Questo accresce il bisogno da parte dell'operatore del sistema di trasmissione di approvvigionarsi di riserve di energia al fine di gestire in maniera sicura e stabile la rete elettrica. In questo contesto, l'accoppiamento dei sistemi di accumulo alle tecnologie basate su fonti rinnovabili appare come la soluzione più credibile al fine di armonizzarne le fluttuazioni di potenza e semplificare la gestione della rete elettrica.

Dal punto di vista di un impianto solare termico, la migliore soluzione tecnologica é rappresentata dall'adozione di un sistema di accumulo termico. Al suo interno é possibile infatti accumulare energia sotto forma di calore attraverso un fluido mantenuto ad alta temperatura. Quest'ultimo può direttamente essere lo stesso fluido di lavoro che verrà poi espanso in turbina o può avere solo una funzione termovettrice. Nel secondo caso il fluido in questione, generalmente costituito da sali fusi, viene utilizzato come fonte di calore per il processo di produzione di vapore all'interno di un apposito scambiatore.

A questo proposito, il presente lavoro di tesi propone un modello termodinamico completo basato su di un impianto CSP realmente esistente caratterizzato da un sistema di accumulo termico. Gemasolar, l'impianto oggetto dell'analisi, è proprietà della società *Torresol Energy Investment* ed è situato a circa 40 km da Siviglia (Andalusia, Spagna), una zona caratterizzata da perfette condizione climatiche e meteorologiche per una centrale solare termica. Lo scopo principale della presente trattazione è la realizzazione di un modello per la simulazione delle prestazioni della centrale in condizioni di funzionamento stazionarie e transitorie. Lo strumento svillupato si presuppone come base per future analisi riguardanti le condizioni di

stress termico e meccanico determinate da un profilo di radiazione variabile.

Il software Matlab è stato utilizzato come base per la realizzazione di ogni parte del modello termodinamico e per la successiva fase di simulazione. In primo luogo, attraverso i risultati di due precendenti lavori di tesi (De Giorgi e Crespi-Zani) é stato possibile ricavare i dati riguardanti le condizione climatiche, i valori di radiazione e le differenti tipologie di puntamento utilizzate come input per il presente modello. L'intera trattazione é basata su una prima analisi teorica focalizzata sul calcolo del tempo di risposta caratteristico di ogni elemento tecnico della centrale. Infatti, attraverso la definizione di un parametro capacitivo e di un termine caratteristico dell'evoluzione del processo è stato possibile valutare l'inerzia del sistema e il tempo di risposta rispetto alle perturbazioni climatiche del periodo di osservazione per ciascuno dei processi meccanici e termici che è possibile osservare nella centrale.

Una volta dimostrato che in una configurazione con sistema di accumulo termico il blocco di potenza può essere sempre caratterizzato da condizioni di funzionamento nominale, in un secondo momento l'analisi é stata concentrata sul ricevitore solare. Prima di tutto, attraverso le informazioni disponibili in letteratura, arricchite con alcune necessarie ipotesi simplificative, è stata definita la struttura geometrica del ricevitore. La stessa è stata poi testata attraverso una verifica di sicurezza per quanto riguarda le condizioni di funzionamento del fluido termovettore.

Il passo successivo prevede la realizzazione di un modello steady-state del ricevitore solare. A questo proposito la risoluzione dell' equilibrio termico é stata impostata considerando gli scambi di calore in direzione assiale e tangenziale tra ciascuna delle unità di flusso in cui sono stati suddivisi i tubi del ricevitore. Il ricevitore solare è stato modellizzato secondo una struttura di 18 pannelli in serie, ciascuno dei quali costituito da 24 tubi in parallelo. La particolare struttura della mappa di radiazione ha poi permesso di considerare la risoluzione di un solo tubo all'interno di ogni pannello, in maniera tale da semplificare il complesso sistema iniziale. Ogni tubo è stato poi discretizzato in 28 sezioni assiali a loro volta suddivise in 8 unità circonferenziali.

Particolare attenzione è stata poi necessaria per la scrittura del codice di simulazione in quanto, all'inizio dell'analisi, più di un parametro del problema risultava essere incognito. Un ciclo iterativo esterno ha permesso infine il calcolo della portata di sali fusi prodotti alle condizioni di temperatura richieste. Successivamente il modello sviluppato è stato utilizzato per analizzare le differenti strategie di puntamento, confermando la strategia numero 6 come la migliore tra le varie a disposizione, garantendo un 2% aggiutivo per quanto riguarda l'efficienza termica del ricevitore solare e una produzione di sali fusi più grande del 1% (423 contro 420 kg/s) rispetto alla seconda migliore strategia.

In seguito, la soluzione del caso stazionario é stata considerata come condizione iniziale per il successivo sviluppo del modello transitorio. Dopo un'analisi preliminare riguardante le differenti capacità termiche del tubo e dei sali fusi, la funzione PDEPE di Matlab e uno specifico ciclo iterativo sono stati utilizzati per la soluzione dell'equazione dell'energia in regime dinamico per quanto riguarda il fluido termovet-

tore (pedice f):

$$\frac{\partial(\rho_f \cdot Cp_f \cdot T_f)}{\partial t} + \frac{\partial}{\partial x}(\rho_f \cdot Cp_f \cdot \overrightarrow{v} \cdot T_f) = \frac{\partial}{\partial x}\left(k_f \cdot \frac{\partial T_f}{\partial x}\right) + h_{conv} \cdot (T_{wall} - T_f) \quad (2)$$

La superficie di parete dei tubi è stata invece considerata in regime quasi-stazionario.

Attraverso una selezione iniziale, il modello permette di impostare la regolazione del sistema secondo due differenti schemi di controllo: *feed-back*, secondo cui la portata massica di sali fusi circolanti nel ricevitore è controllata dalle condizioni di temperatura all'uscità, o *feed-forward*, secondo cui invece il flusso di sali fusi è direttamente impostato a priori a partire da una *look-up table* calcolata in funzione della radiazione incidente. In un secondo momento é stata sviluppata un'analisi dettagliata dei due sistemi di controllo dimostrando come il primo risulti essere il migliore per una corretta gestione del sistema e per un'ottimizzazione termica del ricevitore solare, garantendo una riduzione del 25% del gradiente massimo di temperatura nei tubi del ricevitore e riducendo del 4.2% le temperature massime dei sali in regime transitorio limitando così il rischio di degradazione degli stessi.

Il sistema di controllo é stato poi testato rispetto a condizioni di radiazione a gradino caratterizzate da bruschi sbalzi per quanto riguarda il flusso termico incidente sul ricevitore. Sfruttando le potenzialitá e la versatilà del modello sono state poi condotte varie simulazioni volte ad analizzare la risposta del sistema nei confronti di differenti variazioni climatiche. In questo modo é stata ottenuta la tipologia di nube critica per la stabilità del sistema.

Infine, attraverso la simulazione delle condizioni di funzionamento nominali del blocco di potenza è stato possibile collegare i diversi modelli termodinamici sviluppati e realizzare simulazioni più complesse nel caso di scenari climatici reali.

In conclusione, il presente lavoro di tesi dimostra come l'applicazione di un sistema di accumulo termico accoppiato ad una centrale CSP rappresenti lo stato dell'arte della tecnologia solare a concentrazione. Come ultimo elemento di spunto sono stati proposti poi alcuni possibili progetti futuri basati sull'utilizzo del presente modello e volti all'approfondimento di alcune tematiche di ricerca che sicuramente rappresenteranno un ulteriore passo in avanti per la tecnologia CSP all'interno di un ottica di sviluppo nel mercato energetico globale.

Contents

List of Tables

Listings

Abstract

Concentrated solar power (CSP) is expected to play a key role in the necessary energy transition towards more sustainability. However, this type of system is inherently subject to transient boundary conditions such as varying solar irradiation. In this regard, heat storage system can be coupled to traditional plants in order to reduce the intrinsic source unpredictability.

In the described context, advanced control strategies are required to maintain safe operating conditions and to maximize power generation exploiting the system potential. In order to define, implement and test these control strategies, dynamic models of the system must be developed.

In particular, this thesis aims to develop a model through which simulate the performances of an existing CSP plant with heat storage system (*Gemasolar*, Fuente de Andalusia, Seville - Spain) according to real weather conditions.

In a first step, a power plant time-scale analysis has been developed in order to demonstrate how the receiver processes mostly characterise the overall dynamic system performances according to the considered time-frame. Then, starting from a a technical background composed by two previous works, the developed tool takes as input radiation map according to different aiming strategies and variable weather conditions. The receiver model has been designed according to proper assumptions and both stationary and transient performances have been analysed. In a later stage, the whole model, enriched with a suitable control system logic, is exploited to investigate the receiver response with respect to the clouds perturbations. Once linked receiver and power block substructures complex scenarios have been simulated focusing the attention on the heat storage system filtering function. This work has been conduced using the software Matlab, implementing autonomously all the source codes.

Keywords: PoliMi, Master Thesis, heat storage systems, operating control systems, receiver dynamic thermal model, solar energy, CSP technology.

Sommario

La tecnologia CSP riveste un ruolo fondamentale nel lento ma graduale processo di transizione volto a ridurre la dipendenza dalle risorse fossili e favorire lo sfruttamento di fonti di energia sostenibili. Tuttavia, questa tipologia di impianto risulta essere fortemente influenzata dalla disponibilità della radiazione solare. A questo proposito, particolari sistemi di accumulo termico possono essere utilizzati per ridurre l'impatto causato dall'imprevedibilità della risorsa primaria e incrementare la produzione di energia elettrica.

In questo contesto tecnologico sono neccessari sistemi di controllo e modelli di simulazione avanzati con i quali analizzare nuove possibili strategie di gestione dell'impianto in modo da massimizzarne le prestazioni, garantendo allo stesso tempo ragionevoli condizioni di sicurezza. L'obiettivo del seguente lavoro consiste in particolare nella realizzazione di un modello termodinamico con il quale simulare le prestazioni di un impianto CSP realmente esistente (*Gemasolar*, Fuente de Andalucia, Siviglia - Spagna) secondo le diverse condizioni meteorologiche.

In primo luogo é stata sviluppata l'analisi dei tempi di risposta caratteristici di tutti gli elementi tecnici presenti nella centrale, dimostrando come il comportamento dinamico del ricevitore solare risulti essere determinante in termini di prestazioni generali dell'impianto. Utilizzando come input i risultati di due precedenti lavori di tesi (De Giorgi e Crespi-Zani) é stato possibile considerare mappe di radiazione solare variabili nel tempo a seconda dell'ora del giorno, del periodo dell'anno e delle condizioni meteorologiche. In un secondo momento, utilizzando le poche informazioni disponibili in letteratura e applicando alcune ipotesi semplificative, é stato progettato il modello geometrico del ricevitore Successivamente sono stati sviluppati autonomamente due diversi codici per la soluzione del problema termico in regime stazionario e transitorio del ricevitore. Il modello globale, ottimizzato con un apposito sistema di controllo, é stato poi utilizzato per analizzare gli effetti provocati sul sistema da differenti tipologie di nubi. Infine, una volta analizzate le condizioni di funzionamento nominale del blocco di potenza della centrale, é stato possibile simulare in maniera completa diversi scenari metereologici, valutando in entrambi i casi l'utilitá del sistema di accumulo termico. Il software Matlab é stato utilizzato per tutte le simulazioni numeriche citate.

Parole chiave: PoliMi, Tesi Magistrale, sistemi di accumulo termico, strategie di controllo, modello termodinamico del ricevitore, energia solare, tecnologia CSP.

Introduction

Since the beginning of time, people have been fascinated by the sun. Ancient civilizations personified the sun, worshipping it as a God or Goddess.
Throughout history, farming and agriculture efforts have relied upon the sun's rays to grow crops and sustain populations. Only recently, however, human knowledge has developed the ability to harness the sun's awesome power. In fact, the first attempt in the electrical energy production dates back in 1958 when NASA scientist used PV modules to supply power to spaceships once in space environment. The resulting technologies have promising implications for the future of renewable energy and sustainability especially in the last decade in which renewable energies have strongly penetrated in the energy market thanks to incentives, governing laws and high fossil fuel cost.

The most common way of harnessing energy from the sun is through photovoltaic (PV) panels both in small domestic and large scale power plant configuration. These panels operate as conductors, exploiting the photovoltaic effect available in particular materials that produce current and therefore electrical energy.

On the other hand, solar radiation can be also exploited as heater capacity in a solar thermal power plant in which most of the time the radiation is reflected and concentrated in a unique place in order to achieve an higher working fluid temperature and therefore improve efficiency. In this regard, research in Concentrated Solar Power fields and related thermodynamic cycles started more than 40 years ago, and in the last decade this technology has undergone a huge growth in the commercial applications. A lot of thermo-economic analyses have been done, and in 2007 the first commercial plant started its energy production: PS10, located in Sanlúcar la Mayor, Seville, Spain. This is a 10 MWel power plant characterized by a north field and a cavity receiver configuration in which is directly produced saturated steam that is send to a steam tubine.

A few years later, in 2011, a new commercial solar tower was launched: Gemasolar, situated in Fuentes de Andalucia, Seville, Spain. This plant differs both in size and configuration from PS10: it provides a production of 19.9 MWel, with a surrounding field and an external receiver tower. Moreover it uses molten salts as heat transfer

fluid and has a heat storage system. These particularities allow the plant power block to work in nominal conditions even with variable radiative condition or in case of radiation absence, assuring the plant to be partially independent with respect to the solar source.

The importance of this second plant configuration can be understood having in mind one of the worst problems that affect renewable energy source: unpredictability. In fact, renewable energy exploitation introduces uncertainty and instability in the energy system due to characteristics of the source. This increases the need for regulation of power and requires reserves in different time-frames (minute to hours). These backups are usually provided by conventional technologies; actually, for every GW of wind installed more or less 17 MW of spinning reserves are needed ([10] and [41]). From this point of view, the addition of a heat storage system in a thermal solar power plant could be a reliable solution to improve the production profile and exploit as best as possible solar source.

In the described context, the present dissertation proposes to realise a model able to analyse the transient performances of a solar power plant with heat storage system in case of variable solar radiation condition due to single or multiple clouds passage. The tool developed aims to a better understanding of the dynamic behaviour that affects such a plant and could be used as a base model through which investigating how to increase plant competitiveness and improve plant management. Furthermore with this model it would be possible to simulate and evaluate new operational strategies especially in off-design condition.

In order to have a precise information background, this work uses as reference case the Spanish Gemasolar power plant. This selection is not casual: in fact, a solar radiation tool enriched with different clouds models was already available for the solar field of this plant ([19]) providing an advanced and useful starting point for the present research.
As theoretical basis, a time-scale analysis of the main power plant processes is realised in order to focus the attention on the phenomena that really affects the general behaviour of the system with respect to the characteristic time-frame of the problem. Proceeding using as input the results coming from the solar model mentioned above, a simulation code has been autonomously generated using the software Matlab as compiler. First of all, the tower receiver has been modelled using the information available in literature regarding the reference plant. Afterwords, a thermal model has been developed both in stationary and dynamic condition in order to analyse the evolution of the system depending on the clouds passage. This procedure was accomplished to describe with accuracy the thermodynamic behaviour both of the

solar receiver and the molten salts produced within.

Successively, the algorithm describing the control system of the whole receiver was defined. In particular, through its implementation it was possible to select and simulate different control theories applicable for this case of study. Once defined the whole system behaviour, the attention was then focused on the analysis of the system performances according to single and multiple clouds inputs composed to create a complex scenario.

Outline

The thesis work will be structured as follows:

In the first chapter an overview about the solar energy source is given. Lately, the radiation and clouds tools available in a previous thesis work are analysed in order to better understand the input data needed by the present model. A general review of the literature analysis regarding power plant transient behaviour is then proposed. Finally a time-scale analysis of the reference plant main processes is developed in details.

In the second chapter the main model assumption and all the receiver geometrical characteristics are introduced. The developed algorithm regarding the heat transfer in the receiver is then widely analysed and described in order to illustrate how the model works. This is the core section of the thesis since it presents how both the stationary and transient study have been developed characterizing all the parameters and quantities involved in the analysis.

In the third chapter different control system methods are introduced, then developed inside the model and finally analysed in order to select the best option for the reference case.

In the fourth chapter power block is finally taken into account and analysed in its nominal condition. Lately, the whole receiver model previously developed and the power block are bounded together. In this way, the complete behaviour of the plant is finally simulated in the case of complex scenario.

Chapter 1

State of the art

In this chapter a general review concerning the state of the art of CSP technology is proposed. The first section is dedicated to the solar energy both in terms of source and technology available. Successively the radiation and clouds tools developed in the previous works is presented ([19]), representing, as already said, the basis of the present dissertation. Finally a time-scale analysis of the main thermodynamic processes is developed with respect to the transient problem nature.

1.1 Solar Energy

In this section the solar energy source is introduced together with a description of the available technologies to exploit it.In particular the analysis is focused on the Concentrating Solar Power plants and, even more specifically, on the Solar Tower which is the main topic of this work.

1.1.1 Solar radiation

The energy flow within the Sun results in a surface temperature of around 5780 K. This flow is generated in the core by several fusion reactions, in particular the fusion of 4 protons (Hydrogen nuclei) into 1 Helium atom. The energy is then transferred from the interior to the external surface by a succession of radiative and convective processes. The energy is finally released at a rate of $3.824 \cdot 10^{20}$ MW but, due to the high distance between the Sun and the Earth ($1.495 \cdot 10^{11}$ m) and the dimensions of the two bodies, only $172.5 \cdot 10^{9}$ MW are intercepted. Considering the earth dimensions, this means an incident radiation of 1367 W/m^2 (power per unit area normal to the propagation direction) outside the atmosphere, a value called "*Solar Constant*". The presence of the atmosphere causes a further reduction in the radiation value effectively incident on the earth surface, mainly due to two phenomena: absorption and scattering. The first consists, as the word says, in the absorption of part of the

radiation by the particles composing the atmosphere, in particular water, molecular oxygen and ozone. The scattering, instead, is another type of interaction between the radiation and particles: water, dust and air molecules deflect part of the radiation, creating the diffuse radiation. The reduction to the irradiation introduced can vary between the 30% (perfectly sunny days) and 90% (cloudy days). Therefore the solar energy presents the problems of dilution, discontinuity and unpredictability.

1.1.2 Available technologies

The energy radiated by the Sun and intercepted by the Earth's surface can be exploited mainly through two technologies: Photovoltaic and Solar Thermodynamic.

The first has seen a great expansion in the last years and performs a direct conversion between solar and electrical energy using the "Photovoltaic Effect", i.e. the ability of the photons composing the solar beams to increase the energy state of the electrons when hitting particular semi-conductors materials. With the right geometrical disposition of these materials a voltage is established between two electrodes. The strength of this technology is the ability to use both the direct and the diffuse radiation; the weakness, on the other side, is the low efficiency of the process "solar to electricity", limited to 17-18% for the most expensive photovoltaic cells.

The second type of conversion is thermodynamic: firstly the solar energy is converted into thermal energy by heating a vector fluid, successively the latter could be directly expanded in a power plant cycle to produce electricity or used in a heat exchanger to warm up the power block working fluid. A further division can be made in terms of the use of the solar radiation. In fact, the radiation coming from the sun can directly heat the vector fluid to increase its enthalpy, or can be concentrate in smaller areas. The latter is the category called "*Concentrating Solar Power*" (CSP), which is the object of the present study.

1.1.3 Concentrating Solar Power

In order to study the CSP, a brief introduction needs to be done. The main purpose of concentrating the radiation from a Collecting Area (C_A) to a smaller Absorbing Area (A_A) is the growth of the heat fluxes employed to increase the vector fluid enthalpy. This leads to the achievement of higher temperatures and, consequently, higher efficiencies of the thermodynamic cycles of the power plant. In addition, the smaller the surfaces at high temperature, the smaller the heat losses towards the atmosphere. The ratio between the areas described constitutes a fundamental parameter for these plants, called Concentration Ratio (C_R):

$$C_R = \frac{A_C}{A_A} \tag{1.1}$$

The efficiency of a receiver has an optimum point depending on the Concentration Ratio and the temperatures. Therefore this parameter is a crucial variable in the optimization process of the receiver. The conversion of solar thermal electricity is mainly based on four CSP technologies:

- parabolic disch collector (PDC);
- linear Fresnell collectors (LFC);
- central tower system (CTS);
- parabolic trough collectors (PTC).

Linear Fresnel and parabolic trough collectors are line-focusing concentrators and need a single-axis tracking system (East-West, i.e. azimuth angle variation, or North-South, i.e. elevation angle variation). Their CR result to be lower than 100 and are characterized by medium temperature levels up to 550° C. On the other hand, parabolic dish and central tower systems are point-focusing concentrators featuring a two-axis tracking system. They can reach CR greater than 1500 and high temperatures above 1000°C ([14]). Due to this fact, the latter are expected to achieve higher efficiencies of energy conversion. Currently, the annual solar-to-electricity efficiency may achieve 13% for LFC plants, 11% to 16% for PTC, 12% to 25% for PDC, and 7% to 20% for CRS according to [4].

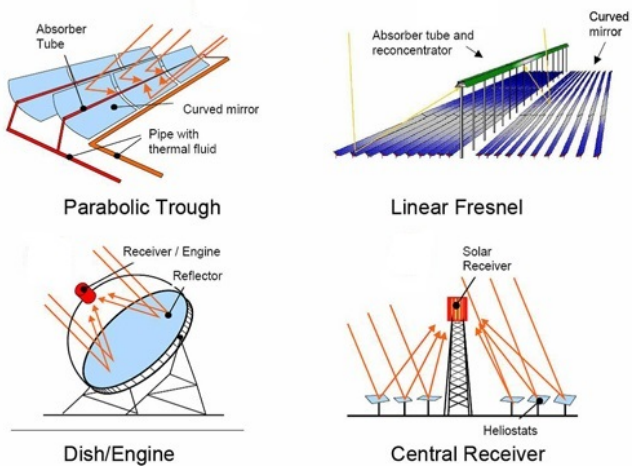

Figure 1.1: Different Concentrating Solar Collectors. Source: [54].

Regarding the cost of electricity, nowadays only PTC and CRS plants are developed enough to provide an estimate of their range of cost: respectively 0.14 €/kWh

to 0.36 €/kWh, and 0.17 €/kWh to 0.29 €/kWh. Looking at the medium-term, a series of potential cost improvements have been identified, leading for instance to a projected cost of 0.08 €/kWh for central tower plants by 2020 ([20]). Even more challenging, the SunShot initiative launched by the US Department of Energy (DOE) in 2011 aims at grid parity for CSP in general with 5-6 €/kWh without subsidies ([30]), which requires disruptive rather than incremental technological advancements over the current decade ([7]). In the following table 1.1 are synthesized the main technical and economic characteristics of the main collector type available in the market:

Collector	Focus	Tracking	C_R	T [°C]	$\eta_{sol-to-el}$ [%]	LEC [€/kWh]
Linear Fresnel	line	single-axis	10-40	60-500	13	-
Parabolic through	line	single-axis	10-85	60-550	11-16	0.14 - 0.36
Parabolic dish	point	two-axis	600-2000	100-1500	12-25	-
Central tower	point	two-axis	300-1500	150-2000	7-20	0.17 - 0.29

Table 1.1: Concentrating solar collector main characteristic from [27].

In the last years, as a result of more stringent regulations on the emission of greenhouse gases, the research attention has been focused on central tower plants due to its low CO_2 emissions (18 g/kWh) compared to fossil fuels (130-900 g/kWh). A great advantage of this technology is the possibility to build a thermal storage system and to use the heat at a later time independently from the sunshine. Such a thermal storage has a cost significantly lower with respect to batteries which are required for technologies producing the electricity directly such as wind turbines or photovoltaic systems ([10]). Moreover the technology benefits of a learning rate of 12% which will presumably lead in 2050 to an energy production cost of 0.04 - 0.06 €/kWh. As central tower plants result to be the technology that shows the highest potential improvement at both the energy and the economic level, they are the object of the present study.

1.1.4 Solar Tower Power Plants

Solar Tower power plants consist of fields of mirrors, called heliostats, collecting the solar radiation and reflecting it towards a receiver situated at the top of the tower. There the incoming radiation is transferred to a fluid through a heat exchanger and the obtained thermal energy is converted into electricity in a power cycle.

Power Cycles

Nowadays, there are four main conversion cycles experimented, and only two of them are used on an industrial and commercial scale:

- pressurized air cycles, experimental (e.g. Solugas [40]);
- atmospheric air cycles, experimental (e.g. Julich [42]);
- direct steam cycles, used in commercial operations (PS10 [2], PS20 [3], Sierra Sun Tower [17], Coalinga [8] and under construction plant Khi Solar One [56]);
- molten salts cycles, used in commercial operation (Gemasolar [44] and Kaxu Solar One [55]).

As shown in Figure 1.2, in the case of a *pressurized air cycle* the air is firstly pressurized in the turbo-compressor of a gas turbine block and then it is heated in a pressurized receiver at temperatures of 800-900°C and sent to a combustion chamber, where the fuel is added and the mixture goes through a combustion process. Therefore, this type of power plant exploits both the solar energy and the natural gas. Then, the exhaust gases are expanded in a turbine and then cooled in a steam generator (HRSG) of a Rankine cycle, allowing the increase of the overall efficiency with a combined cycle.

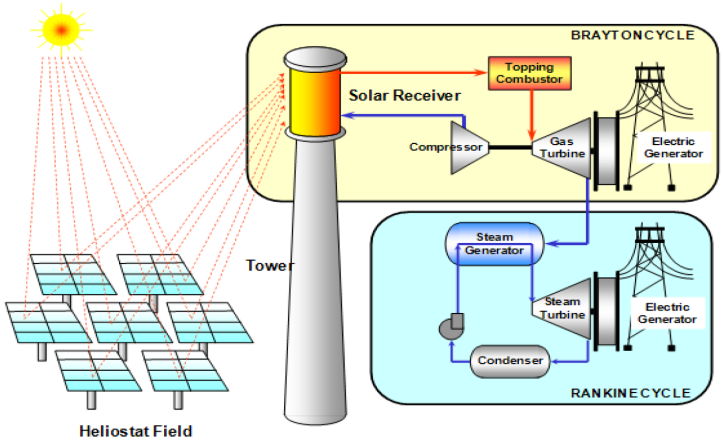

Figure 1.2: Pressurizes air cycle power plant layout. Source: [48].

In the atmospheric air cycle plant, as reported in figure 1.3, the ambient air passes through a volumetric receiver where is heated by the solar radiation up to 680-950°C, and then it could be directed either through a packed bed storage unit, during the charge process, or through a steam generator during the discharge. Afterwards, the air returns to the inlet of the receiver, with the possibility of a re-cycle of the 45%.

Direct steam cycle power plants are different from the previous ones, because the fluid expanded in the steam turbine is the same that is heated in the receiver. In the figure 1.4 it can be seen that the feed water is pumped and passes through the receiver, where it is evaporated typically up to a steam quality of 0.2-0.3. Afterwards, the fluid goes to a steam drum that divides the steam from saturated water. Then

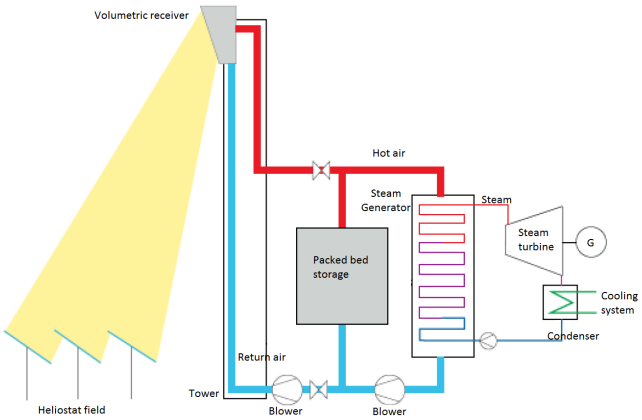

Figure 1.3: Atmospheric air-based cycle plant layout. Source: [48].

the steam, maintained at saturation conditions (250°C and 40 bar [2], is accumulated back to the ground in a short-time buffer tank that allows a regulation capacity of about 45 minutes at half nominal power. After that, the steam is expanded in the turbine, condensed at about 0.06 bar and 50°C and finally pumped up in the tower again.

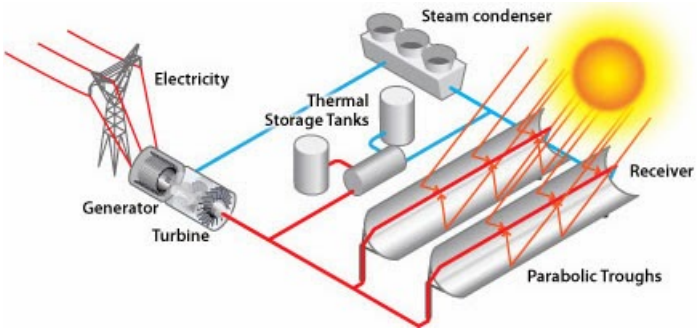

Figure 1.4: Direct steam cycle plant layout. Source: [48].

The molten salt cycle is the conversion cycle used in the commercial plant Gemasolar in the province of Seville, Spain. Its main feature is the storage system that results to be one of the most important topics of research and development for the future of this technology and object of the present work. The molten salt (also called HTF, acronym if Heat Thermal fluid) is pumped from the cold storage tank (290°C) to the receiver, where it is heated up to 565°C and then is stored in the hot storage tank (1.5). Afterwards, the molten salt passes through a steam generator in order to run a conventional steam cycle, and finally returns to the cold storage tank. Depending on the amount of molten salt used, the storage capacity may reach 15 hours per day, allowing 24 hours of operation on a summer day. Moreover, the molten salt cycle is very useful to reduce the discontinuity and unpredictability of the solar energy source.

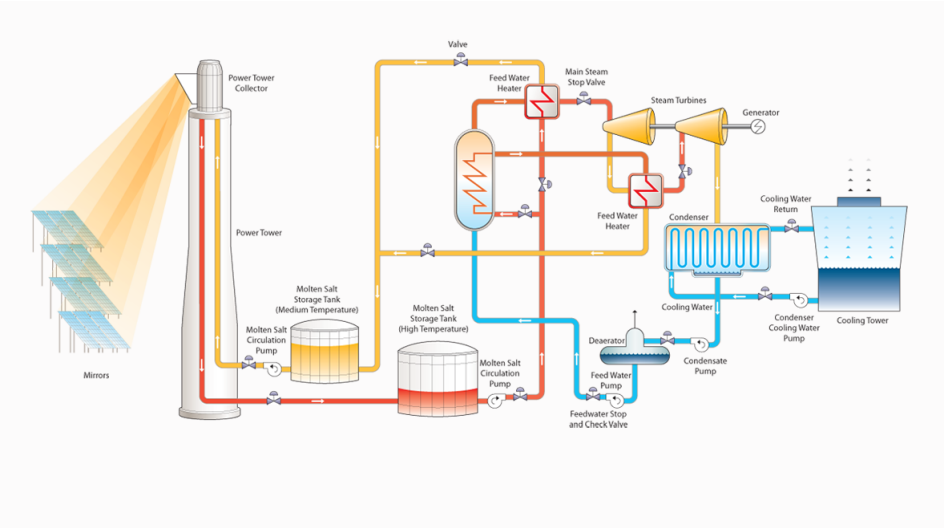

Figure 1.5: Molten salts cycle plant layout.Source: [48]

.

Heliostat fields

In the last forty years more than thirty solar fields have been designed and built worldwide, but only a few of them are for industrial commercial facilities. The majority are experimental fields, of medium-small size, constructed in order to start the tests on the CSP technology, such as the CRTF in Albuquerque, USA (1978) or the Thémis tower in Targassonne, France (1982). Moreover, a few pilot plants were commissioned as well, such as Solar One and Two in Barstow, USA (1982 and 1996) or the SEDC in the Negev desert, Israel (2008) in the recent past. As regards the commercial plants, the first one ever built and started-up is the PS10 in Sanlúcar la Mayor, Spain (2007). Since this moment, several commercial facilities have been designed and built, and they can be categorized according to their total reflective area ([7]): small-scale (<10.000 m^2), medium-scale (10.000-100.000 m^2), and large-scale facilities (>100.000 m^2). The aim of small-scale facilities such as the Solastor field in Lake Cargelligo, Australia (2011) is to provide electricity and/or heat to relatively small communities. Medium-scale facilities like the Sierra SunTower in Lancaster, USA (2009) are designed to satisfy the demand of local industrial scenarios. Finally, large-scale facilities such as PS20 and Gemasolar in Spain (2009 and 2011) and Ivanpah in California (2013), run towards heliostat fields with more than 1.000.000 m^2 of total reflective area, in order to satisfy greater electrical demands.

It can be easily observed from figure 1.6 that the majority of the Heliostat fields are situated in developed countries, especially in areas characterized by high values of DNI, at least 2500 kWh/m^2. Existing commercial facilities can be found in western USA, eastern Australia, southern Spain and middle-east, but not yet in the Sahara zone, southern Africa, Mongolia, Chile, Argentina or Brazil. This is due to the

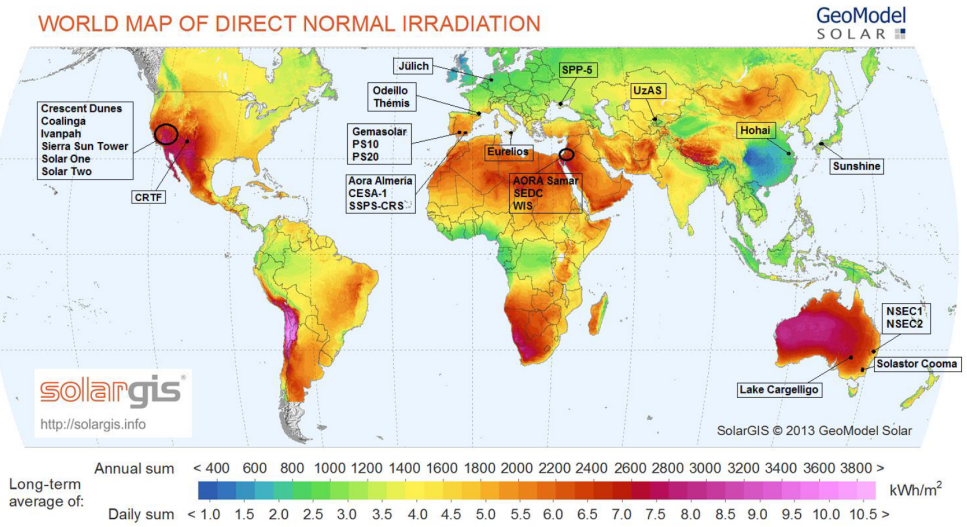

Figure 1.6: Map of heliostat fields worldwide. Source: [52].

fact that DNI is not the only parameter to take into account but also topology, hydrography, land cover and power network, along with a social and political point of view, have to be considered [42]. Basically, the field layouts can be divided in two main categories: North-field (or South, considering the Southern hemisphere) or surrounding field. The former presents the whole group of heliostats only on one side of the central tower and are normally coupled with cavity receivers, whereas the latter is characterized by mirrors that completely surround the tower and are coupled with external receivers. The selection of the layout mostly depends on the site's latitude and on the chosen receiver: the North-fields normally are coupled with cavity receivers, surrounding ones with external receivers. The experimental facilities normally feature a North-field layout, the commercial ones can present both of them (e.g. PS10 and PS20 north-field, Gemasolar and Ivanpah surrounding field). Another distinction could be made on the disposition of the mirrors in the field layout: grid and circular layouts. The first ones present heliostats disposed by a simple grid of W-E and S-N rows; the second ones by concentric circles whose centre is the tower base. In both cases, the spacing between rows increase with the distance to the tower base in order to decrease interferences between neighbouring heliostats, for example shadowing. Nevertheless, the final layouts are normally calculated via software with a techno-economical optimization: the results are irregular shapes characterized by a higher presence of mirrors in the Northern part of the field (considering the Northern hemisphere), due to the better incident angles of the sun. The heliostats require high values of reflectivity, a good tracking system with a great accuracy, wind resistance and low specific costs. In fact the cost of the heliostat field is predominant in a solar tower power plant due to the huge number of mirrors (from hundreds to thousands) and the bi-dimensional driving system. This driving system allows the

heliostats to move in two directions (azimuth-elevation) in order to follow the sun both in the daily and seasonal motion in the sky and intercept the radiation with the highest possible normal surface component. Heliostats can be composed of a single mirror panel or an assembly of several panels, mounted on a frame supported by an horizontal and vertical axis. The panels, both of rectangular or circular shape, can present a slight convex curvature in order to obtain a more focused image on the receiver. Moreover periodical washings to clean the mirrors and reduce the fouling effect are required. Finally wind results to have a considerable impact on the mirrors, causing them to oscillate and therefore reduce the accuracy.

Receiver

The receiver of a central tower is a delicate component, due to the fact that it receives the concentrated solar radiation and is therefore subject to great thermal fluxes and stresses. There are two main kinds of receiver: cavity and external. In a cavity receiver the absorbing surface is located inside the tower, and the radiation enters through an aperture. This allows to greatly reduce the convection and radiation losses but, at the same time, the acceptance radiation angle is also decreased. For this reason, cavity receivers are normally used only in north-field plants, for example PS10 or PS20. External receivers are more exposed to thermal losses, either convection and radiation but on the other hand, they have no limitations on the acceptance angle and thus are implemented in surrounding fields, such as Gemasolar. Moreover, the receiver elements can be attached together in different overall pattern, the most used are flat and cylindrical geometry. The former can be oriented towards the field to improve the capture of the radiation; the latter can be either a half-cylinder cavity receiver, or a full cylinder external receiver. Considering the plant of interest for this work, Gemasolar presents a 16 m tall external cylindrical receiver.

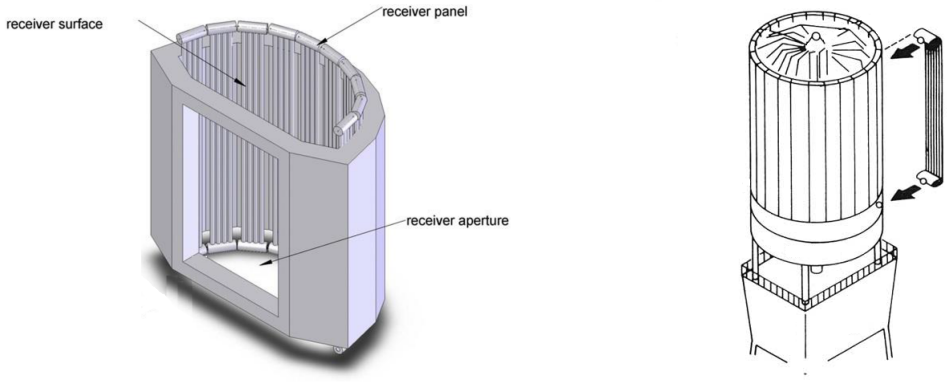

(a) **(b)**

Figure 1.7: Tower receiver configurations: cavity (a) and external receiver (b).

Solar Tower

(a) **(b)**

Figure 1.8: Solar Tower: concrete [Gemasolar](a) and lattice [Ivanpah] (b).

The central tower presents the receiver at its top and needs to reach a considerable height, at least around 100 meters, in order to allow the furthest heliostats to create a sufficiently good reflected image on the receiver. At the same time it has to contain all the pipes in which the fluid flows. Moreover, the tower has also the essential task of transferring the heat to the fluid in the best way. In particular it has to guarantee the appropriate insulation in order to reduce heat losses by convection to the atmosphere and by conduction through the structure. Finally, the tower should also be designed taking into account the sensitivity to wind, the shadows projected onto the field and the visual impact on the landscape in the distance. The structure of the central tower could be made either of reinforced concrete or steel lattice. The former is the most used by the commercial plants, due to the better pipe insulation and wind resistance with the addition that the buildings have rooms dedicated to various experiments. The latter presents, on the contrary, less shadows with an improving of the reflected image on the receiver.

1.1.5 Energy performance of a solar tower

The solar tower, where the receiver and the pipes are located, is one of the most important component of the plant and it is very important to understand its behaviour and thermal losses in order to achieve a better planning and working of the whole plant.

Thermal losses

The performance of the solar tower is affected, as already said, by several losses; the main are: convection, reflection and radiation towards the ambient. They are related to the kind of receiver used (cavity or external) and to the temperature of the receiver. There are also conductive and radiative losses through the tower itself but they are smaller than the former.

- *Convection losses*: some of the energy is lost because the air close to the receiver surface is heated and natural circulation phenomena occur. Basically with cavity receivers only natural convection is taken into account because cavity receivers are thought to reduce the effects of forced convection. On the contrary external receivers are subjected to the wind action and so the convection is forced determining higher convection losses;

- *Reflection losses:* a part of the incident radiation is not absorbed but is reflected even if the pipe surfaces are coated with a high absorptivity paint that minimizes this loss. They may increase throughout the lifespan, due to the degradation of the coating itself;

- *Radiative losses towards ambient*: Stefan-Boltzmann equation says that each body at a temperature greater than 0 K emits energy in the form of electromagnetic radiation. The receiver is subjected to high temperatures due to the strong energy incoming from the field and therefore loses energy emitting radiations in the infrared and visible light. These losses are lower with a cavity receiver since the part at high temperature is shielded against the sky (lower view factor);

- *Radiative losses through the interior*: in order to reduce these losses, a sheet of insulating material coated with a very high reflectivity metal sheet covers the part of the pipe not subjected to the solar irradiation. This obviously reduces the thermal losses and increases the efficiency of the heat exchange;

- *Conduction losses*: the amount of losses through the interior in a tower is very low compared to the external ones and is related to the heat flow rate flowing through the insulation layers to the ambient, finally lost by convection and radiation.

Transient events

A solar receiver undergoes frequent transient events and the nature of these is very different with respect to a conventional thermal power plants. The plant operates

during the day when heat from the sun is available and is off during the night. Along with the daily start-up and shut-down, it also undergoes various other transient events including short or long cloud passages followed by hot-start, partial load transient during light cloud events, cold start-up transients (after extended shut-down events). Moreover the fast changing of the heat flux and receiver temperature leads to great thermal stresses on the material that could be very dangerous for the plant life time. One of the main purposes of this work is therefore studying the transient response of the solar tower in order to optimize the power production avoiding the mentioned problems.

1.1.6 Gemasolar power plant

The present study carries on an analysis of the Spanish **Gemasolar** solar power plant. A detailed description is included in the following paragraphs, with a detailed discussion of the main characteristics, from the dimensions, through the receiver shape and the heat exchange fluid up to the heat storage system and the power block.

Figure 1.9: Gemasolar power plant.

Gemasolar became operative in 2011 and employs an innovative technology. It has a nominal power of 19.9 MW but presents a storage system dimensioned for a continuous operation of the plant (15 hours storage for a 24 hours a day working [44]), where the only stops are made for maintaining or for prolonged bad weather conditions. The resulting yearly working hours are about 6.500 and the energy production is 110 GWh/year. The heat exchange fluid is the same of the storage, i.e. a mixture of molten salts. The two tanks of the storage are kept at 565°C and 290°C.

This allows the production of a steam that enters the turbine at 100 bar and 540°C, resulting in good efficiencies of the steam cycle (40%). The heliostat field surrounds the tower and is composed of 2.650 mirrors (for an overall surface of 185 Ha, almost 2 km^2, of which the 15.6% reflective); the receiver is therefore external cylindrical. The tower is 147 meters high while the receiver has an height of 16 meters with a diameter of 8 meters.

1.1.7 Purpose of the thesis

In this thesis it has been decided to analyse the performance of a solar tower during design and off design operating conditions. In particular, once the stationary conditions of the receiver are obtained, the transitory phenomenon and the control system are modelled for the Gemasolar reference plant.

Starting from previous studies done on nominal and partial load operations, a further improvement has been accomplished. It has been studied how the shadow on the solar field affects the receiver and thus how the temperature map of the latter changes during cloudy days. It is also analysed the whole working fluid behaviour in the receiver and how it affects the heat storage system, since its evolution is the base of the power production. Even if the plant studied receives at least 9 hours of sunshine 320 days per year, with 15 hours per day in midsummer, this aspect is very important to understand the thermal behaviour of the system and the related stresses on the solar receiver. The latter is one of the key equipment in a solar tower power plant that operates under extremely non-uniform heat flux, cyclic weather and cloud transient conditions. Very high and quick changes of radiation lead to sudden variations of heat flux. Despite the null "fuel" cost, the kWh cost resulted to be twice the mean traditional plants kWh cost ([49]).The objective of this work is to analyse how the clouds affect the molten salts production and to provide all the information about the receiver temperatures in order to allow a future thermal stress analysis. On the other hand, the bounded analysis of the heat storage system and the power block allow to investigate the capacity of the plant to remain partially independent with respect to the solar source oscillation.

Different scenarios are simulated choosing the most common and unfavourable weather conditions for the specific plant studied.

1.2 Optical and clouds models

In this section the models developed in previous works will be described in order to provide more details about the present study. In particular the aiming strategies and the cloud models are described.

The radiation input data are created using *Delsol 3* software as source ([1]) and are successively processed by the Crespi-Zani's *Solar Tool 5* ([19]). The latter uses the field and receiver geometrical approximations made by De Giorgi ([22]) and introduces the clouds model. At the end of the described software sequence, *Solar Tool 5* provides as output the solar radiation distribution on the receiver surface according to the aiming strategy selected and the clouds evolution taken into account.

1.2.1 Solar field

In order to create a series of suitable aiming strategies, first of all a good solar field discretisation has to be made.

The Gemasolar's field is divided in 128 zones according to [19].This choice is the result of a trade off process considering field size, the accuracy of the clouds passage simulation and the computational time required by *Matlab* to solve the problem. As reported in figure 1.10, a division in 8 circular rows and 16 azimuthal sectors is the resulting framework.

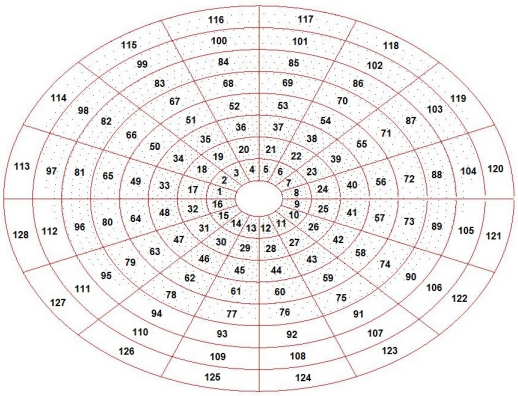

Figure 1.10: Gemasolar power plant.

In order to allow the representation of the flux maps, the receiver surface has been divided in three parts. Due to its cylindrical geometry, three sectors of 120° have been defined, starting from the south and proceeding with clockwise direction (panels 000-120-240). Moreover, 9 points in each panel of the receiver have been

defined in order to achieve the zone aiming. The point number 5 coincides with the center of the panel, and the location of the others can be defined with the values for the horizontal and vertical displacement. In this way the desired aiming strategy can be defined: associating a number from 1 to 9 to each zone, all the heliostats included in that zone will aim to the point of the receiver that corresponds to that number. If the number 0 is chosen, the heliostats will aim to a point considerably far from the receiver (100 meters higher): in this way it has been possible to simulate the shadowing of clouds, simply de-focusing the heliostats.

1.2.2 Aiming strategies adopted

The possible aiming configurations are hereunder detailed.

- *Aiming strategy 1*
  It has the result to reduce the peak flux with a low variation of the total energy absorbed.

- *Aiming strategy 2*
  It allows a strong peak reduction with a small loss of energy.

- *Aiming strategy 3*
  The results obtained with this strategy look like the previous ones apart from inverted focusing.

- *Aiming strategy 4*
  It allows to evaluate how the spillage losses vary changing the focus of the heliostats far from the tower. Peak flux lowers slightly and spillage losses obviously start to increase. For these reasons in the following strategies the second half of the field will not be displaced from the center.

- *Aiming strategy 5*
  The fifth configuration, compared with the previous ones, shows a reduction of the peak flux of minor intensity but it has also the lowest energy losses. The first row is aimed to the bottom of the receiver and the following three to the top.

- *Aiming strategy 6*
  It shows very low energy losses and peak reduction reaches its highest value.

Anyway, in the *Solar Tools 5* help section a briefly description of the aiming strategies is provided, in order to let the user fully understand its meaning and permit a

favourable choice.

In the subsequent table 1.2, the six different aiming strategies are resumed.

	Aim 1	Aim 2	Aim 3	AIm 4	Aim 5	Aim 6
Row 1	2	2	8	8	8	2
Row 2	2	2	8	8	2	8
Row 3	2	8	2	2	2	2
Row 4	2	8	2	2	2	8
Row 5	5	5	5	2	5	5
Row 6	5	5	5	2	5	5
Row 7	5	5	5	5	5	5
Row 8	5	5	5	5	5	5

Table 1.2: Resume of the six aiming strategies for Gemasolar. The row 1 contains the zones from 1 to 8, the row 2 from 9 to16 and so on.

The aiming strategy 6 is adopted by default in the present work and is maintained throughout the whole analysis, being the best aiming strategy both for design and off-design case as demonstrated by De Giorgi and Crespi-Zani. By the way for future studies it will be possible to change it in order to analyse a wider range of possibilities.

1.2.3 Wind characterisation

Gemasolar power plant is property of *Torresol Energy Investments* ([44]) and is located in Fuente de Andalucia, close to Seville (Spain), a floodplain formed by the Guadalquivir River in the Andalusian region. Andalusia is approximately between 36° and 38°44' parallel in the south of Iberian Peninsula and its climatic analysis shows that it is an area in which masses of air from the Atlantic Ocean flow. In particular during spring and summer a humid and warm wind comes from the third quadrant (S-W), while it turns to the first (S-E) during fall and winter. This last, as counterpart, is a dry and temperate wind [29].

In this geographical and climate context, wind statistically crosses Andalusia region most of the time from S-W to N-E, as reported in figure 1.12. This representation is referred to the meteorological station of the Seville airport [57] and is considered a reliable description also for Gemasolar power plant, being only 52 km far from its location. This diagram takes into account both frequency distribution and average wind intensity. Scale in percentage point compared to the maximum wind speed and direction varies with altitude. This means that wind parameters measured close to the earth surface level, where meteorological station are located, are not the same at the clouds level. In order to evaluate this effect, the Hellman equation has been used:

Figure 1.11: Gemasolar power plant location in the Iberian Peninsula.

$$v_{wind}(H) = v_{wind@10m} \cdot \frac{H}{10}^{a} \tag{1.2}$$

Where $v_{wind}(H)$ is the wind speed at the desired height, $v_{wind@10m}$ is the wind speed at an heigth of 10 meters and H is the height. Finally, a is the Hellman exponent that varies regarding the roughness of the terrain. For this particular study, since the two power plants are located in flat terrains surrounded by open land, the parameter has a value of 0.16 ([47]).

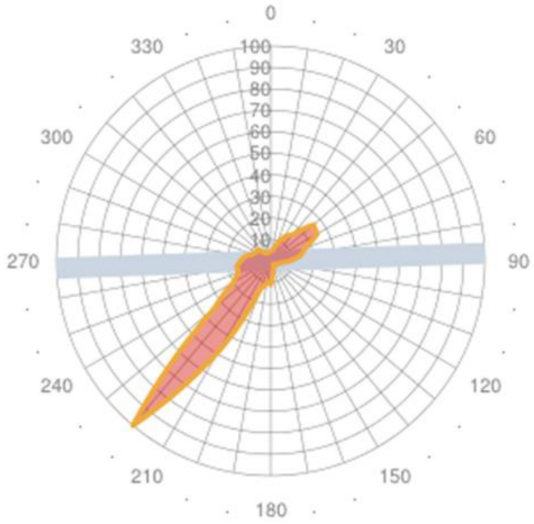

Figure 1.12: Wind chart for Seville Airport and neighbourhood. Source: [57].

1.2.4 Clouds characterisation

This thesis focuses on the off-design working conditions due to unfavourable meteorological conditions. For this reason, additionally to wind considerations a

preliminary study about clouds characterization has to be done: this step is very important because the entire thesis is based on these first assumptions.

Clouds are representative, and thus lead, to complex meteorological phenomena such as rain, snow and hailstorm. From a thermodynamic point of view, clouds are the visual aspect of several events that take part in a gaseous fluid known also as atmosphere: temperature, humidity and pressure.

Clouds are challenging to model because of the very high inhomogeneity in type, shape and velocity, and they are universally classified by altitude range.

According to the geographical and climate condition of the power plant site, the type of clouds taken into account in the present study are the *cumulus humilis*, that are also known as the "clouds of good weather" [23]. They are characterized by a flat light grey basis and small white domed tops. Usually the vertical height from base to top is less than the width of the cloud base. This type of clouds are the worst for this type of plants because leads to fast alternating DNI. Rapid change among blue sky (with a DNI of about 1000 kW/m^2) and shadow (DNI = 0) leads to unstable working operation for the solar tower.

These clouds come in a range of sizes, from small popcorn cumulus to large tropical cloud clusters. The boundaries of the clouds are, usually, highly irregular. It is extremely difficult, if not impossible, to model them as any common geometric figure ([9]).

The velocity of a cloud is obviously related to the wind speed at that height. A lot of study has been done on this topic. Hisashi Kon ([24]) demonstrated that the ratio between clouds and wind speed decreases with the height due to the variation of density of the clouds. Moreover, it has been observed that due to the fact that wind speed increases with the height, these two phenomena offset each other. For these reasons the clouds assume a quite uniform velocity along their axis and the speed is very close to the average wind speed touching the cloud. An assumption done in this work is that the clouds have the same speed and velocity of the wind. Moreover it is assumed that the transmittance of the cloud is zero. It means that all the direct solar incident radiation is stopped by the cloud. Furthermore a hypothesis on the boundary was made: edge sharpness, to avoid further complexities.

1.2.5 Clouds modelling

According to Crespi-Zani's work it has been chosen to characterize six different clouds for the Gemasolar transient simulation. All the clouds come from the same

direction (S-W, 220°). It has been decided not to simulate clouds coming from south-east due to their low probability of appearance, allowing the study of more significant ones. Similar clouds with different sizes have been taken into account, in order to better analyse the effects of the shadowing of high efficiency zones and to see how the field can mitigate the strong DNI reduction.

The chosen clouds are the following:

1. A big cloud covering all the field: ***total shadow***
   The average Gemasolar diameter is about 1500 meters, therefore a cloud with the same size has been chosen.

2. A big cloud covering the left part of the solar field: ***left shadow***
   The field has been subdivided in two main areas with a line parallel to the main wind direction and crossing in the middle. In this case all the left part has been progressively shadowed as shown in figure 1.13.

3. A big cloud covering a great portion of the field : ***total shadow as PS10***
   The peculiarity of this case is that the cloud has the same size of another power plant field: PS10. This choice has been made to understand which are the effects of the same cloud on two different plant sizes, as studied in the original Crespi-Zani work where the two Andalusian plant Gemasolar and PS10 were analysed and compared. Regarding the present work, this cloud represents an intermediate case between *small cloud* and *total shadow* ones.

4. A small cloud crossing in the middle of the field: ***small cloud***
   In this simulation the size of the small cloud with average diameter of about 200 meters is analysed.

5. Two small clouds crossing in the middle of the field: ***two small clouds***
   Two side clouds are modelled, both of them are about 200 meters of diameter. These two clouds are roughly 150 meters far and cross in the middle of the field, where there are the heliostats that most affect the peak flux values on the solar receiver.

6. A cloud big as the PS10 field covering the left part of the field : ***left shadow as PS10***
   As in the *total shadow as PS10* case, this cloud takes geometrical reference from the PS10 field size and crosses the left part of the Gemasolar field.

Due to the fact that the clouds passage is not simulate in a continuous way, the simulation provides a temporal subdivision of the entire process in “time-steps”.

Solar Tools 5 subdivides in 20 time-steps the progressive covering of the Gemasolar field. This choice has been done to have a good compromise between quality and computational cost for the simulation.

As it can be observed from the figure 1.13, an irregular shape of the clouds with sharp edge has been assumed. Some of the 20 time steps are represented below, in order to let the reader understand the main path of each cloud. Only the shadowing process is showed because the unshadowing process is exactly the opposite: the cloud keeps maintaining its direction with the same velocity, unshadowing firstly the heliostats shadowed in the covering process.

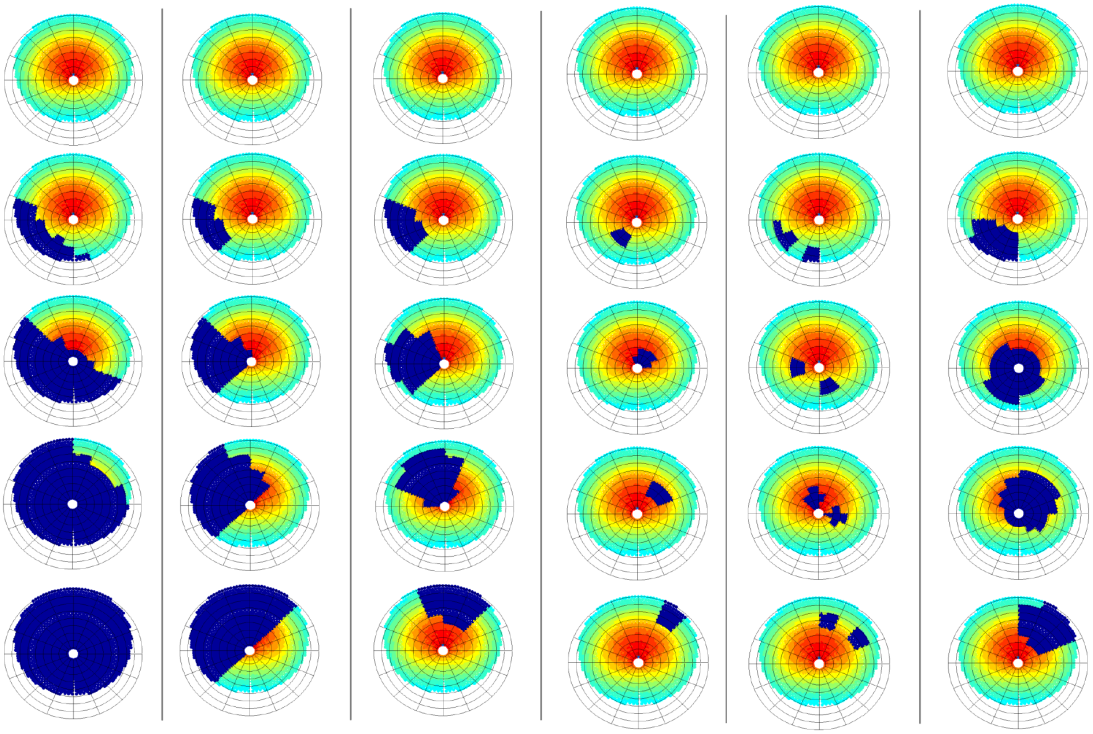

Figure 1.13: Evolution of the shadowing on the Gemasolar solar field for different clouds. From left to right respectively: *total shadow, left shadow, left shadow as PS10, small cloud, two small clouds, total shadow as PS10.*

In order to better understand the two previous figures a further clarification is here reported. The colours through witch the solar field is painted represent the heliostats efficiency, increasing in the scale from blue to red. In this regard and according to the clouds modelling assumptions, the blue regions represent the field portions without solar radiation, i.e. where the heliostats efficiency is equal to zero due to the cloud passage.

1.3 Solar tower transient performances modelling: literature review

In this section a general review of the transient models available in literature is presented and analysed. A particular attention is here dedicated to all the technical components of a solar tower power plant. In fact, with the final aim of the transient performances analysis, it is mandatory to understand which of the power plant processes really affect the system due to the time-varying boundary conditions.

First of all, a list of the main technical equipment objects of the research has to be defined:

- Solar receiver;
- HTF - steam heat exchanger;
- Steam turbine;
- Condenser
- Feed water heater (FWH);
- Pump;

Furthermore, two possible theoretical approaches have to be distinguished:

- quasi-steady state model;
- transient model.

According to the selected one, the model and the results accuracy will be strongly different.

1.3.1 Quasi-steady state model

Quasi-steady state is a particular condition in which, after a perturbation, a new equilibrium state is reached in a considerably low amount of time. This means that the considered process or the object of the analysis has an high adapting capacity with respect to the changed boundary condition and changes its characteristics properties with an high velocity rate.

Most of the time quasi-steady state is a theoretical assumption adopted in order to simplify difficult problems when the above considerations are verified. For example,

in the case of a thermal process such as heat exchange, quasi-steady state is referred to a body characterized by a low heat capacity that necessitates a small amount of incoming energy in order to warm up.

In this regard, the problem is simplified because stationary state equations are used to model the phenomena rather than transient ones, and in this way the use of partial differential equations that describe the time-dependency of the problem can be avoided.

According to these assumptions, a basic model for the analysis of a cavity and external receiver in case of clouds passage ([32]). In particular, the cited tool firstly computes the main system parameters for each of the thermal maps available considering these conditions as if they were the stationary ones. In a later moment, the solution of all parameters for the time-frame in between two thermal images are obtained by interpolation of the stationary results. In this way, the software computational cost is reduced at its minimum value but, on the other hand, the accuracy of the system results to be rough.

Furthermore the thermal storage term of both the pipe and HTF is neglected and, as a consequence, the resulting behaviour of the entire system results to be extremely affected by the radiation: in fact, few seconds of shadows are enough to stop the HTF production rate and cool the receiver pipes in a considerable way.

Whole system quasi-steady state assumption is hereby abandoned preferring a complete transient model. In this way improved thermal results could be achieved, providing a better representation of the real phenomena development.

1.3.2 Transient model

A variety of models can be found in the available literature regarding the transient modelling of power plant equipment. According to the list above, the most suitable tools are hereunder proposed.

Solar receiver

As evidenced in the introduction chapter, the solar receiver is the most critical element in a concentrating solar power plant. Being completely exposed to the solar radiation, high temperatures can be achieved for both the pipes surface and the HTF, resulting in a high modelling complexity.

In this regards, [38] proposed a detailed model for the transient simulation of solar cavity receivers using an interesting one-dimensional approach for the pipes

thermal equilibrium. The code, built and solved using *Modelica*, allows to evaluate different receiver geometries in order to reduce as much as possible thermal losses increasing at the same time the thermal efficiency in the warm up process.

Steam turbine

Steam turbine is for sure the most analysed power plant technical element in literature due to both its importance and its complexities.

In these regards, model from both traditional and CSP applications are available.

Chaibakhsh focuses the attention on the power performances, characterizing the transient dynamics of steam turbine sections through non-linear mathematical models based on energy balance, thermodynamic principles and semi-empirical equations ([12]). The resulting parameters are successively determined by empirical relation or they are adjusted by applying genetic algorithms based on experimental data obtained from a complete set of field experiments. The resulting simulation provides accurate outputs but it is not a suitable reference for the present study due to the lack of information regarding the turbine system mounted in the Gemasolar power block.

On the other hand, Topel focuses the attention on the turbine thermal performances ([43]). Aiming to improve turbine operating flexibility, a thermal model is developed and the resulting temperature profile is made available for further stress analysis. In this regard, particular attention is paid for the start-up cases considering a steam turbine for solar applications and its typical transient operating conditions. Finally, the dissertation proposes the adoption of electrical thermal layer in order to maintain the turbine case temperature in the case of solar radiation lack avoiding in this way expansion and temperature gradient problems. By the way, this specific model does not consider the presence of a heat storage system and, as a consequence, can be used only as reference case being not directly applicable to the present work.

HTF - steam heat exchanger

Regarding the heat exchange modelling, Crespi and Hoopes present a method to evaluate the off-design performance of a heat exchanger with an unspecified geometry ([18]). Instead of assuming one of the heat exchanger terms in a lumped volume approach as constant (such as UA, temperature difference, ε etc.) the method proposes to accurately predict performances as function of a single parameter named *conductance ratio*. This term is defined as the product of heat transfer coefficient and area on both sides of the heat exchanger. In this regard, the model can be useful

in the transient off-design condition for both the steam-HTF heat exchanger and feed water heaters for the Gemasolar case.

Global power plant model

A global power plant modelling is proposed by Queralt ([33]). Applying lumped dynamics model to each power plant component (boiler, turbine, condenser, receiver and pumps) the whole code is built using *Modelica ThermoCycle* library and launched using *Modelica* as compiler. In this regard, the entire system is parametrized respecting the real physical problem in a robust and computationally efficient way. By the way the final purpose is a great range high level simulation and not a single detailed solution. As a consequence, [33] does not provide a precise reference for the present dissertation but only a guideline for the equipments parametrization.

1.4 Solar tower transient performances modelling: time-scale analysis

Once revised models and tools available in literature, in this section a time-scale analysis of the dynamic response of the main elements composing the power plant is developed. A wide literature research confirms that a rigorous analysis of the transient characteristics of each one of these systems has not been performed yet. As a consequence, this analysis provides an additional scheme to the technological state of the art, aiming to underline the importance of each element with respect to the main topic of this work. Furthermore it represents the fundamental theoretical basis through which it would be possible to develop the thermodynamic model according to suitable simplifying assumptions.

1.4.1 Defining model requirements

As already noted, the present study of Gemasolar power plant behaviour involves the analysis of systems with capacitive elements. The elements control the rate at which process parameters change due to net 'forces' imposed by the change in the boundary conditions. As reported by Gemmen ([21]), a general dynamic equation showing capacitance behaviour is:

$$\frac{d[\int (c \cdot P) \cdot d\forall]}{dt} = G_n \tag{1.3}$$

where P is a process parameter associated with a conserved physical quantity Z. That is, $P = Z/c$, where c is the so called capacitance parameter. In general, P, Z and c can vary in space, and so equation 1.3 shows an integration over space, $\forall$, to arrive at the total amount of the conserved quantity Z within the given control space that could be either a volume or an area depending on whether the phenomena has been considered. Finally, the net addition of Z to the control space is described by G_n.

Equation 1.3 is hereby used in a first-order analysis that provides estimates for the various time-scales occurring in a CSP power plant. Such an analysis will be helpful in chapter 2 to determine the requirements of the various sub-models in order to provide an efficient calculation approach to clouds passage transient problem.

To determine the first-order time-scale of a particular transient, equation 1.3 is rearranged as follows.

$$\Delta t = \tau = \frac{\Delta[c \cdot P \cdot \forall]}{G_n} = \frac{\forall}{G_n} \cdot c \cdot \Delta P = \frac{C_{\Delta P}}{P_r} \tag{1.4}$$

τ is the characteristic time for the transient under study, and ΔP is the first-order

estimate for the change in the process variable. The grouping $c \cdot \Delta P$ is referred as the capacity parameter, $C_{\Delta P}$, since it describes the amount of change in the fundamental physical parameter, and $G_n/\forall$ is referred as the Process Rate Parameter, P_r. As a consequence the ratio, $C_{\Delta P}/P_r$ gives the estimate for the time-scale of the transient.

As an example, the case of a thermal diffusion problem can be considered. In this regard, a body of density ρ and heat capacity Cp is in contact with another medium of temperature T_s. The initial body is assumed to have a temperature T_{body_1}. The fundamental equation above can be rewritten in the form:

$$\rho \cdot Cp \cdot L \cdot \frac{dT_{body}}{dt} = k \cdot \frac{T_s - T_{body}}{L} \tag{1.5}$$

where L is the characteristic length of the conductive problem and k is the thermal conductivity. Scaling the entire process over the whole time-frame of the transient phenomena, the time passes from t_1 to t_2 and the body reaches the new T_{body_2} temperature.

For the overall transient the temperature rate of change is $(T_{body_2} - T_{body_1})/(t_2 - t_1)$ and the average driving potential for the thermal conduction will be the temperature difference between the body surface in contact with the medium and the internal portion. According to the first order relationship between the parameters, by integrating the previous equation it results:

$$\rho \cdot Cp \cdot L \cdot \frac{T_{body_2} - T_{body_1}}{t_2 - t_1} = k \cdot \frac{T_{body_2} - T_{body_1}}{L} \tag{1.6}$$

Simplifying in both sides the common temperature difference and solving for the $t_2 - t_1$ term, the time constant is obtained.

$$\tau = \frac{C_{\Delta P}}{P_r} \cong \frac{\rho \cdot C_p \cdot L}{k/L} \tag{1.7}$$

1.4.2 Gemasolar power plant time-scale analysis

The time-scale analysis of the CSP power plant main elements is developed according to the theoretical basis explained in 1.4.1. As already introduced, these results can be helpful to guide the following modelling phase by showing how the transient behaviour of the equipment can be simplified.

More specifically, to provide an efficient use of computational resources, it is customary in dynamic modelling to consider only the details of a given transient process if its characteristic time-scale is within one or two orders of magnitude from the main effect under examination. In this case the characteristic time used as

reference is the interval in which the boundary conditions change.

Hence, while investigating the performances of a concentrated solar power plant affected by clouds passage with a characteristic time-scale on the order of 10^2 seconds, the same value has to be considered as reference. As a consequence, any transient process having a characteristic time greater than 10^4 seconds can be assumed constant; i.e. no detailed model equation is necessary to relate the parameters of that process to the rest of the model. On the other hand, in the case of a transport process having a characteristic time-scale less than 10^0 s, then the related physical parameters can be assumed to behave in a quasi-steady condition and a steady state equation is required to relate the transient process parameters to the rest of the model. All other processes with a characteristics time-scale in within these two values have to be taken into account and require the use of their respective fundamental dynamic equations to relate them to the rest of the process.

The choice for the separation of time-scales (10^2 seconds used here) will affect the temporal accuracy of the solution. A wider time span will result in more phenomena predicted using their respective dynamic equation. This means an improved accuracy but a higher computational cost as well. On the other hand, a lower time span will provoke excessive inaccuracy in the model because important transient processes would not be considered.

Starting from the steam turbine, proceeding through heat exchanger, pumps and receiver, the time-scale analysis of the main elements is hereunder reported according to the principal processes that occur within.

Steam turbine thermal time-scale analysis

Transient phenomena affecting the steam turbine operating conditions are mostly due to the heat exchanged from the working fluid to the turbine mechanical parts and the torques balance at the shaft.

As result of the expansion of the superheated steam coming from the heat exchanger, the turbine receives a huge amount of heat that has to be dissipated. In particular, heat is exchanged from the flowing steam to the turbine blade on which it impacts and successively, the heat flux is directed to both the external casing and the rotor hub.

- **Casing thermal diffusion time** computed for the high pressure stage case.

$$\tau = \frac{Casing\ thermal\ capacity}{Thermal\ diffusion\ rate} = \frac{\rho_{steel} \cdot Cp_{steel} \cdot t_{HP}^2}{k_{steel}} \tag{1.8}$$

where t_{HP} is the casing thickness of the high pressure turbine first stage and is computed through the ASME correlation ([46]). Due to the turbine design, HP stages are characterized by the smallest blade heights. As a consequence, the heat released by the steam proceeds mainly through the casing towards the environment along the radial direction, affecting only in a lower scale the mechanical parts in rotation. For sake of simplicity steel properties are considered for both blades and casing.

- **Blade heating time** computed for the last stage.

$$\tau = \frac{Blade\ heat\ capacity}{Steam\ heat\ transfer\ rate} = \frac{\rho_{steel} \cdot Cp_{steel} \cdot h_b}{h_{steam-blade}} \tag{1.9}$$

On the other hand, blade configuration in the last turbine stage is characterised by the highest height values due to the increment of the steam specific volume proceeding through the turbine expansion. As a consequence, heat flux mainly acts on turbine blades with negligible influence on the turbine casing.

In this regard, last stage blade height is computed proceeding through an indicative stage design by setting the upper limit of the periferical velocity ($\overrightarrow{U}$) and the chord value according to available literature.

- **Blade thermal diffusion time** computed for the last stage.

$$\tau = \frac{Blade\ thermal\ capacity}{Thermal\ diffusion\ rate} = \frac{\rho_{steel} \cdot Cp_{steel} \cdot {h_b}^2}{k_{steel}} \tag{1.10}$$

Due to the bigger size, last stage blades perform as a slab in the thermal perspective. As a consequence, diffusion rate time-scale has to be considered according to the blade thermal capacity.

- **Rotor hub heating**

$$\tau = \frac{Hub\ heat\ capacity}{Steam\ heat\ transfer\ rate} = \frac{\rho_{steel} \cdot Cp_{steel} \cdot dx}{k_{steel}} \tag{1.11}$$

The heat transfer rate from the flowing steam and the rotor hub is hereby analysed. In this case a characteristic length, dx, is assumed according to the data available from the model discretisation made by Kopel ([43]).

Steam turbine mechanical time-scale analysis

Swing equation ([39]) describes the mechanical equilibrium between the motor (T_M) and the resistant torque (T_R) on the turbine shaft and its relation with respect

to the rotational speed (ω).

$$T_M - T_R = J \cdot \frac{d\omega}{dt} \tag{1.12}$$

Equation 1.12 has been used together with an empirical model for the turbine inertia constant computation (J in the above formulation, [26]) in order to describe the transient process to which the proposed steam turbine is subjected in the case of a load reduction with respect to the nominal conditions.

In particular, higher the load variation, higher the rotational speed change. This analysis tries to estimate the time-scale process in which the system changes its rotational speed by 1 *rpm* under the imposed load change. Two possible cases are analysed according to different values of mass flow rate available at the turbine inlet in case of partial radiation.

- **Shaft acceleration for a 10% load reduction**

$$\tau = \frac{Speed\ variation}{Rotational\ acceleration} = \frac{\Delta\omega}{\alpha} \tag{1.13}$$

  In this case, 10% load reduction is considered. According to the system inertia the acceleration of the system is computed and, as a consequence, the characteristic time-scale of the process.

- **Shaft acceleration for a 10% load reduction**

  The same evaluation is repeated for the case of a 50% load reduction in order to analyse a more affecting process.

Pump time-scale analysis

In normal literature analyses, pump influence is usually neglected due to its minimal response time with respect to the other power plant elements. By the way, for completeness purposes, pump is considered in this analysis for both the constant speed plus by-pass valve and variable speed configurations. The latter is further subdivided in the cases of a 10% and 50% mass flow rate reduction.

- **Fluid perturbation response time**

  In this section the hammer effect time-scale is analysed. Also called as *hydraulic shock*, hammer effect is a pressure wave propagation caused when a fluid in motion is forced to stop or change direction suddenly by pumps or valve perturbation effect.

  The characteristic time-step is computed by the ratio of the pipes length and the sound velocity in water medium.

$$\tau = \frac{L_{pipes}}{v_{sound}} \tag{1.14}$$

- **Pneumatic actuator for by-pass valve**

  In the case of a constant speed plus by-pass valve pumping configuration, the time required by a pneumatic piston to actuate corrective actions on the valve is considered. As reported by Yokota ([5]), the new valve position can be reached in a roundabout of 10^{-1} seconds neglecting the possible actuator oscillations,.

- **Pump acceleration for a 10% mass flow rate reduction**

  In the variable speed pump case, the time required by the system to fit the rotational speed according to the new mass flow rate value has to be analysed. In this regard, starting from the mass flow rate variation it is possible to define the new pressure guaranteed by the pump and imposed by the steam turbine through the *pressure sliding* rule ([15]). As a consequence, new pump head can be computed as function of the pressure value. Using the similitude rules, it is then possible to obtain the new pump rotational speed and the speed difference with respect to the nominal conditions. With the shaft acceleration, available from the resolution of the swing equation for the pump shaft, the process time-scale can be finally calculated as follows.

$$\tau = \frac{Speed\ variation}{Rotational\ acceleration} = \frac{\Delta\omega}{\alpha} \tag{1.15}$$

- **Pump acceleration for a 50% mass flow rate reduction**

  The same evaluation is repeated for the case of a 50% mass flow rate reduction.

Solar receiver time-scale analysis

The solar receiver thermal phenomena are analysed from a time-scale perspective considering the whole heat transfer process from the pipe wall surface to the molten salts.

- **Tube wall thermal diffusion time**

  Considering the same pipe thickness (t_{pipe}) and material properties as in 2.2 the heat exchange due to conduction through the pipe tube wall has been analysed as follows.

$$\tau = \frac{Tube\ wall\ thermal\ capacity}{Thermal\ diffusion\ rate} = \frac{\rho_{pipe} \cdot Cp_{pipe} \cdot {t_{pipe}}^2}{k_{pipe}} \tag{1.16}$$

- **Tube wall to HTF thermal heating time**

  The heat transfer process from the pipe wall surface to the molten salts is hereunder analysed. All the properties here introduced are computed as described in 2.2. The following equation is used for the calculation of both the inlet and outlet receiver section due to the considerable changes in HTF properties throughout the entire warm up process.

$$\tau = \frac{HTF\ heat\ capacity}{Thermal\ diffusion\ rate} = \frac{\rho_{fluid} \cdot Cp_{fluid} \cdot dx}{h_{conv,int}} \tag{1.17}$$

Air cooled condenser time-scale analysis

The steam condensation process has been analysed both from the HTF and ambient temperature perspective. In this regard, air properties are computed using EES Software (*Engineer Equation Solver*) as data source. On the other hand, heat transfer coefficients and condenser geometric parameters are obtained as output from *Thermoflex* simulations.

- **Tube wall to ambient air thermal heating time**

$$\tau = \frac{Air\ heat\ capacity}{External\ convection\ heat\ transfer\ rate} = \frac{\rho_{air} \cdot Cp_{air} \cdot dx}{h_{conv,ext}} \tag{1.18}$$

- **Tube wall thermal diffusion time**

$$\tau = \frac{Tube\ wall\ thermal\ capacity}{Thermal\ diffusion\ rate} = \frac{\rho_{pipe,cond} \cdot Cp_{pipe,cond} \cdot {t_{pipe,cond}}^2}{k_{pipe,cond}} \tag{1.19}$$

- **Condensate to tube wall thermal heating time**

$$\tau = \frac{Pipe\ heat\ capacity}{Internal\ convection\ heat\ transfer\ rate} = \frac{\rho_{pipe,cond} \cdot Cp_{pipe,cond} \cdot dx}{h_{conv,int}} \tag{1.20}$$

- **Overall thermal heating time**

  The overall heat transfer coefficient (U) is considered in order to summarise all the heat transfer processes that occur in the condenser.

$$\tau = \frac{Air\ thermal\ capacity}{Overall\ heat\ transfer\ rate} = \frac{\rho_{air} \cdot Cp_{air} \cdot dx}{U_{condensate-air}} \tag{1.21}$$

Feed water heater time-scale analysis

In the FWH bleed steam is used to warm up the boiler feed water. In this regard, heat exchange processes between steam and water are considered for the case of the last FWH, considered the most critical ones from a thermal perspective. In fact, it is subjected to the highest value of temperature in both the steam and water side due to its last position on the water heating line from condenser to boiler. All the thermodynamic values reported below come from the Gemasolar power block simulation proposed in chapter 4. On the other hand, geometric FWH parameters such as pipe thickness ($t_{pipe,FWH}$) are provided by a further simulation using *Thermoflex* software.

- **Tube wall thermal diffusion time**

  Equation 1.4.2 is used to describe thermal conductive process within the FWH tube wall.

$$\tau = \frac{Tube\ wall\ thermal\ capacity}{Thermal\ diffusion\ rate} = \frac{\rho_{pipe,FWH} \cdot Cp_{pipe,FWH} \cdot {t_{pipe,FWH}}^2}{k_{pipe,FWH}} \tag{1.22}$$

- **FWH section heat transfer time**

  The overall heat transfer time-scale is considered for each of the three sections of the FWH, defined according to the steam condition: superheated, condensing and drain cooled section.

$$\tau = \frac{Water\ thermal\ capacity}{Overall\ heat\ transfer\ rate} = \frac{\rho_{water} \cdot Cp_{water} \cdot dx}{U_{steam-water}} \tag{1.23}$$

HTF-steam heat exchanger time-scale analysis

In the Gemasolar power plant, the HTF-steam heat exchanger is the connecting element between the molten salts and the power plant circuits.

As a consequence, the time-scale analysis of this element has a crucial importance inside the entire plant investigation. In this regard, each side of the heat exchanger is properly considered for the case of the evaporation section, being the most critical one due to the water phase change.

- **HTF to tube thermal heating time**

$$\tau = \frac{Tube\ wall\ thermal\ capacity}{Heat\ transfer\ rate - HTF\ side} = \frac{\rho_{pipe,HX} \cdot Cp_{pipe,HX} \cdot \cdot dx}{h_{HTF-pipe}} \tag{1.24}$$

- **Tube wall thermal diffusion time**

$$\tau = \frac{Thermal\ diffusion\ rate}{Thermal\ diffusion\ rate} = \frac{\rho_{pipe,HX} \cdot Cp_{pipe,HX} \cdot {t_{pipe,HX}}^2}{k_{pipe,HX}} \tag{1.25}$$

- **Tube wall to steam thermal heating time**

$$\tau = \frac{Steam; heat\ capacity}{Heat\ transfer\ rate - steam\ side} = \frac{\rho_{steam} \cdot Cp_{steam} \cdot dx}{h_{pipe-steam}} \tag{1.26}$$

1.4.3 Time-scale results

In this subsection the results obtained from the time-scale analyses are reported in a graphical way and analysed from the transient problem perspective.

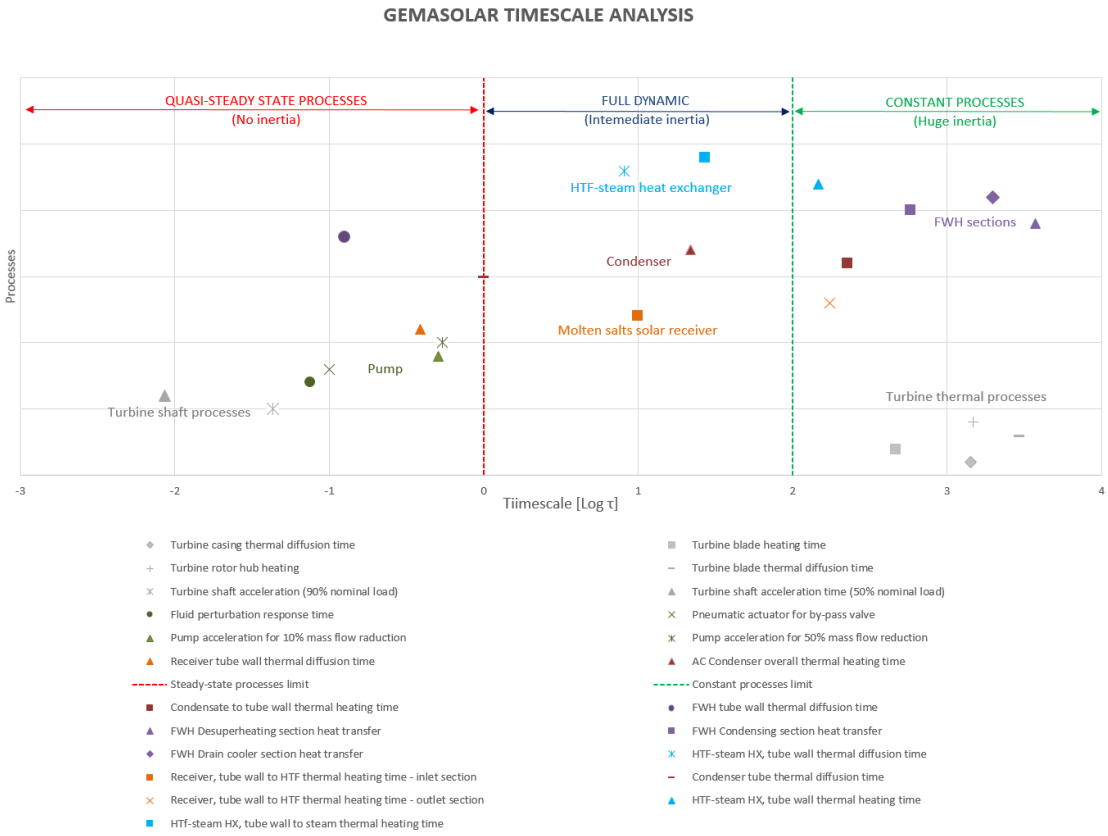

Figure 1.14: Gemasolar time-scale analysis results.

In this regard, figure 1.14 reports the results of the previous analyses in a logarithmic scale in order to appreciate the different orders of magnitude of the main

processes time-scale.

As already introduced, three different processes categories are defined according to the computed characteristic time (τ).

Quasi-steady state processes	$\tau < 10^0$
Transient processes	$10^0 \leq \tau \leq 10^2$
Constant processes	$\tau > 10^2$

Table 1.3: Time-scale categories.

Turbine torque balance and pump phenomena are attributed to the *Steady-state processes* category, and, as a consequence, they can be described using stationary equations in the whole power plant model. On the other hand, thermal phenomena in both turbine and feed water heaters are ascribable to the *constant processes* category. In fact, their characteristic time-scale is higher then the τ upper limit meaning that in the considered cloud passage time-frame these equipments keep constant working condition as if perturbation did not occur.

In between constant and quasi-steady state, *transient processes* category can be evidenced. To the latter HTF-steam heat exchanger, condenser and solar receiver processes are attributable. In this regard, transient processes require a complete dynamic analysis considering their time-varying properties.

By the way, the analysis developed is not enough to properly describe the whole plant response time with respect to the perturbation issue. In fact, the obtained results are referred to each one of the elements considering a "stand alone" configuration, i.e. as if they were working without connection to the other equipments. This assumption was useful to develop in an easier way the time-scale analysis but further considerations concerning how these results are contextualised in the global power plant working framework have to be made. In particular, heat storage system and the two different fluid circuits have to be taken into account.

Gemasolar power plant presents two huge tanks in which hot and cold molten salts are stored. This configuration allows to have two closed circuits: one for HTF and one for the Rankine cycle water connected through an heat exchanger. As a consequence, in case of partial or fulfilled hot tank, the power block plant portion continues to perform in nominal condition even if the solar radiation input is changing over time.

In this way the cloud perturbation affects directly the solar receiver but its effects are stopped at tanks level due to their damping function and only an empty hot tank scenario would lead to off-design power block working conditions. As a consequence

no transient phenomena are verified neither in the HTF-steam heat exchanger nor in the condenser.

Furthermore, air cooled condenser processes are dependent on the environment conditions (ambient temperature especially) that fix the condensing temperature and the other heat transfer parameters. By the way, weather conditions cannot change in such a way to strongly affect the condenser performances in the considered time-frame: no way that ambient temperature can change in the order of 5-10 °C in a period of few minutes.

Thanks to the time-scale analysis enriched with the previous considerations only the solar receiver processes are ascribable to the transient category and have to be modelled according to their dynamic equations in order to obtain the entire system performances in the case of cloud passage. In this regard, in the next chapters both the stationary and transient models of the solar receiver are proposed, while in chapter 4 a complete plant scenario is simulated.

Chapter 2

Methodology

After an appropriate introduction, the receiver thermal model is illustrated in this chapter. The first short section explains the motivation of the software selection. After that, the second section is dedicated to the receiver geometry description, from the pipe design to the complete receiver structure passing through the heat thermal fluid (HTF) flowing inside. In a later stage, the stationary conditions are modelled using a radiation map representative of a complete sunny condition. Finally the transient model has been considered and designed using the stationary conditions as basis.

2.1 Software selection

Software is an essential element in a model development process: both computational power and coding ease has to be taken into account. In this regard, *MathWorks's Matlab* resulted to be the best choice. In fact, it can provide a wide range of tools and functions in a user friendly interface that really helps users during the whole development. Furthermore, both the temporal and geometrical discretisation of the present model can be properly represented in a framework of matrices and vectors for which Matlab results the suitable compiler. Last but not least, Matlab was also the software used in Crespi-Zani's work; therefore proceeding with the same choice was considered the best solution in order to avoid any problems in transferring data through different compiling programs.

2.2 Receiver model

In this section Gemasolar external receiver model is explained. Particular attention is paid both to the pipe diameter choice and HTF flowing path within the receiver.

2.2.1 Pipes general modelling

The pipe is the base unity of the receiver, therefore its modelling is the first thing to do in order to accomplish the overall structure. In fact, pipes structure, tube size, length and thickness are all parameters that affect the correct functioning and the cost of the whole plant. For example the smaller the diameters, the higher the velocities keeping the same mass flow rate. This corresponds to higher Reynolds numbers, higher internal heat transfer coefficients and, on the other hand, higher pressure losses. It is also possible to use a U-tube to increase the total amount of heat exchange area since it allows the fluid to flow twice in the receiver. In this way it is possible to increase the mass flow with the same benefits and disadvantages of the previous case. Nonetheless the final price has to be taken in account. By the way, in order to realize the proper selection, the characteristics of the fluid that flows within the pipes have to be analysed in advance.

2.2.2 Heat thermal fluid properties

Gemasolar receiver uses molten salts as heat thermal fluid. The main purpose of the HTF is transferring the amount of heat coming from the solar radiation to the heat exchanger (HX), where steam is produced and sent to the turbine for the final electrical production. In this regard, molten salts are selected for their suitable heat transfer characteristics.

The molten salts used in the Gemasolar case are composed by a 60% weight fraction of $NaNO_3$ and a remaining 40% of KNO_3; the final conglomeration is also known as "*solar salts*". By definition molten salt is a particular salt which is solid at standard temperature and pressure (STP) but enters the liquid phase due to elevated temperature. In this regard, the minimum temperature for exploiting the mixture is fixed at 290 °C, that is in fact set as cold storage tank temperature. This choice is made in order to avoid solidification problem that could lead to a complete system blockage with the consequent collapse of the entire plant ([50]). On the other hand, also an upper limit has to be fixed in order to avoid degradation problems. Degradation is a critical condition that could occur with temperatures above the 600 °C at which the mixture looses all its properties and, as a consequence, is no more useful for its purposes.

By a numerical point of view, the solar salts properties required by the code are computed by using *Engineering Equation Software* as source (EES, [51]). In particular, *EES* provides the possibility to compute them as a function of temperature and pressure in the available range between 260°C and 620°C.

From a thermodynamic perspective, molten salts have to reach high velocities, and therefore high Reynolds number, in order to guarantee a proper value of the heat transfer coefficient. For this reason the pipe diameter value has to be relatively small. Due to the lack of official information from *Torresol Energy Investments*, the pipe diameter has been set according to the data available from scientific publications and similar power plant studies ([11] and [36]). The selected value is reported in table 2.1.

2.2.3 Pipes thickness

Thickness is an important pipe parameter for heat exchange and mechanical stresses calculation under both stationary and transient conditions. In this regard, pipe minimum thickness is determined in accordance with the *American Society of Mechanical Engineers* (ASME) correlation ([46]).

$$t = \frac{P \cdot D}{2 \cdot (S \cdot E + P)} + C \tag{2.1}$$

Where "P" is the internal designed pressure, "D" the internal diameter, "S" the allowable stress, "E" the quality factor and "C" the term that resumes corrosion and erosion allowances.

2.2.4 Pipe material

According to [36], a suitable material choice for this case is represented by the Fe-Ni-Cr alloy, also known as *"Incoloy 800 H"*. Corrosion and traction resistance, together with the capacity of withstanding high temperatures are the main characteristics of this composite. Furthermore, pipes are usually covered with a special coating that has a selective behaviour with respect to the incident radiation. This means that its optical properties, such as reflectivity, absorptivity and emissivity, change significantly according to the radiation wavelength. In fact, it has to behave as close as possible to an ideal material: unitary absorptivity in the spectral range of the solar radiation, and null emissivity in the thermal infrared region, with a sharp change among the two regions. Composed coatings, such as ceramic-metallic mixture, satisfy these requirements since they have a high absorptivity peak in the solar spectrum and a low emissivity in the thermal infrared region.

The main geometrical values and material properties previously introduced are summarized in the following table:

Variable		Value	Unit
Pipes length	L	16	[m]
Internal diameter	d_{int}	0.0422	[m]
Thickness	t	0.0050	[m]
External diameter	d_{ext}	0.0522	[m]
Coating reflectivity	ρ	0.02	[-]
Density	ρ_{pipe}	7900	[kg/m^3]
Thermal conductivity	k_{pipe}	16	[W/mK]

Table 2.1: Characteristics of the selected pipes

2.2.5 Pipe discretisation and heat transfer assumptions

In order to develop a complete and precise thermal model, pipe length is divided in 28 segments (*j-index*)and each annulus on the axial direction is further subdivided in 8 circumferential pieces (*i-index*)(figure 2.1, *a* and *b*). The axial subdivision is the same of the Crespi-Zani's heat flux map. On the other hand, the number of circumferential flux units is selected as trade off between computational cost and model accuracy.

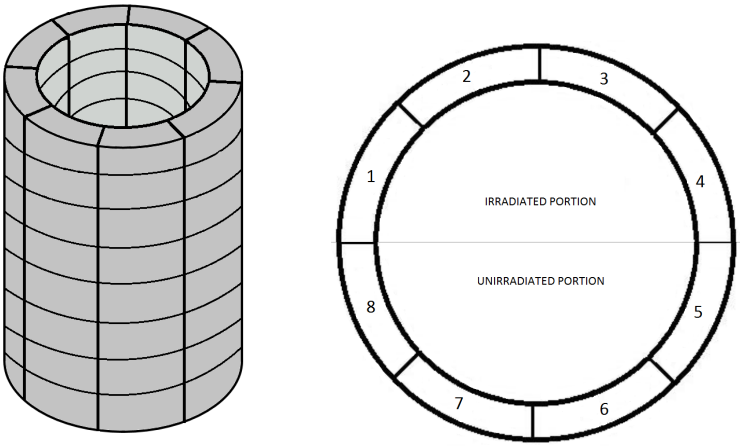

Figure 2.1: Pipe discretisation details: complete (a) and circumferential subdivision (b). Note that in figure (a) the axial pipe direction is modelled only with 8 flux units rather than the real 28 in order to not overload the graph.

This configuration allows to study both tangential and axial equilibrium along the whole tube, as done in the case of a linear Fresnell collector ([31]). Furthermore, once defined the model geometry, it is possible to start simplifying the problem by the use of suitable assumptions; the main ones are the following:

- Due to the geometrical discretisation, four external pieces are irradiated while the internal ones do not have any incident radiation (figure 2.1, *b*). As a

consequence, internal pieces receive heat only by upper and adjacent portions thanks to conduction contribute through axial and tangential directions

- Heat exchange between pipes and tower is neglected. This is correct, for the conductive term, if the tower wall has a temperature close to the pipes one. In this regard, the additional presence of an isolating material on the pipes external surface reduces heat leakages to the tower ([38]). Moreover, considering the tower wall adiabatic also the radiative emission from the pipes to the tower is negligible.

- Fluid temperature inside the pipes is considered constant for each annular section. In fact, thanks to the turbulent flow, the fluid particles are continuously mixed determining an homogeneous situation with a certain level of approximation.

- No heat is assumed to be exchanged through adjacent pipes. In fact, by assumptions each of them is considered to have a very similar temperature with respect to the adjacent ones. In this way, both the conductive and radiative contributions on the overall heat balance are considered negligible. As confirmation of the present assumption, it has to be considered that the solar radiation map available from Crespi-Zani has not the same geometrical discretisation as the receiver pipes subdivision. It results that each group of 24 pipes moving on the circumferential direction has the same radiation value. Therefore, it looks reasonable that they may have the same temperature profile.

2.2.6 External receiver

The external receiver has a cylindrical geometry, with a diameter of 8 meters and an height of 16 meters. The discretisation of the receiver is linked to the Crespi-Zani's heat flux map used as input. In this regard the receiver surface has been originally divided in three sectors of 120°, starting from south and continuing in a clockwise direction. Each panel is composed by 168 flux units, 28 in the height and 6 in width.

The HTF flows within 432 pipes (18 panels, 24 parallel pipes each) laid on the external surface of the receiver, in parallel with respect to the receiver axis. Furthermore, considering the heat flux map 24 pipes are attributable to a single flux unit due to geometrical discretisation.

From preliminary analyses it results that the heat flux map has peak values on the northern part of the receiver surface (as demonstrated in figure 2.2 by the red colour for the heliostat efficiency) due to the geographical location of the plant in the Northern hemisphere. In this regard, the best idea for the pipes design is to set

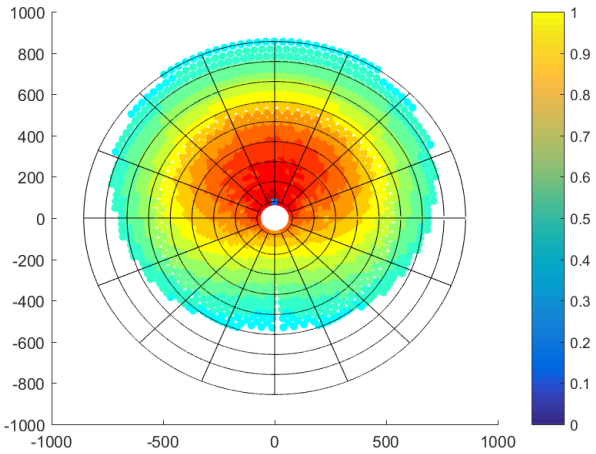

Figure 2.2: Heliostats efficiency for June at 12 am.

the entrance of the HTF circuit in this peaks area. In this way it is possible to cool the pipes wall in a proper way avoiding high temperatures that could provoke creep problems in the material.

Proceeding with the receiver model development, the pipes layout has to be designed. In this regard, the solar salts mass flow rate coming from the cold tank is split in two portions and is sent to different circuits by the use of independent pumps, one for each of them. In this way it is possible to evidence a western and eastern path covered by the HTF. As better explained in the figure 2.3, the former proceeds from North to South in an anticlockwise direction, the latter moves on the same N-S route but in a clockwise direction.

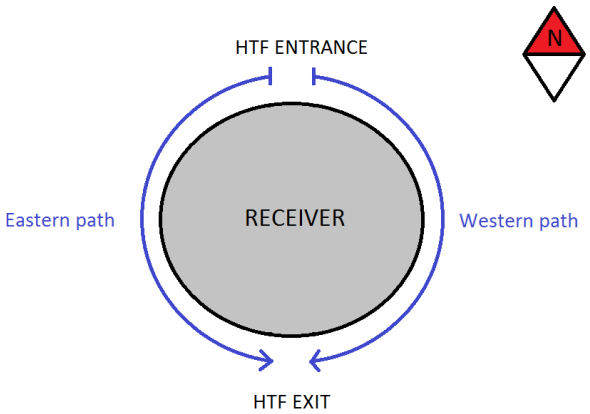

Figure 2.3: HTF different paths through the receiver.

By the way, each of the two HTF paths has the same parallel and series pipes configuration proceeding along the receiver surface. In the developed configuration,

the fluid enters from the bottom of the first 24 parallel pipes panel and warms up proceeding along the vertical direction. As shown in figures 2.4 and 2.5, at the end of each panel a collector reunites the HTF coming from the parallel pipes and sends it to the next ones. The resulting structure allows to properly heat the HTF up to the required conditions, controlling at the same time the pipe wall temperature on the entire receiver.

Figure 2.4: Pipes panel structure.

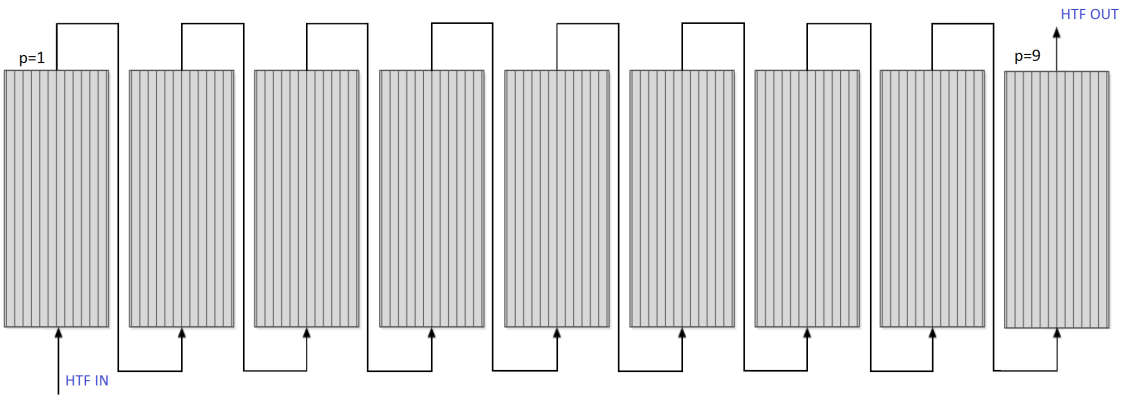

Figure 2.5: Panels configuration for both eastern and western paths.

As further assumption, only one of the 24 pipes of each panel has been considered in the solution of the present model. In fact, as already said, the radiation map has a discretisation that set the same heat flux in the region occupied by a panel, so it is the same for all the 24 pipes. Furthermore the HTF that enters each panel pipes comes from the previous panel collector and, as a consequence, has the same temperature profile. This equality of the boundary conditions allows to ease the complexity of the problem considering only 18 pipes (one for each

of the 18 panels, using *p-index* to represent it) instead of the 432 of the whole receiver.

Figure 2.6 summarizes all the previous considerations. As shown, the modelled receiver is characterized by 2 HTF paths, each of them proceeds through 9 pipes (*p-index*) panels in series. Each panel is analysed by considering the characteristic tube performances. Finally, as already mentioned in 2.2.5, all the tubes are divided in $N = 28$ (*j-index*) annular sections, each of them further subdivided in 8 portions (*i-index*). At the end, the developed model considers 4032 flux units.

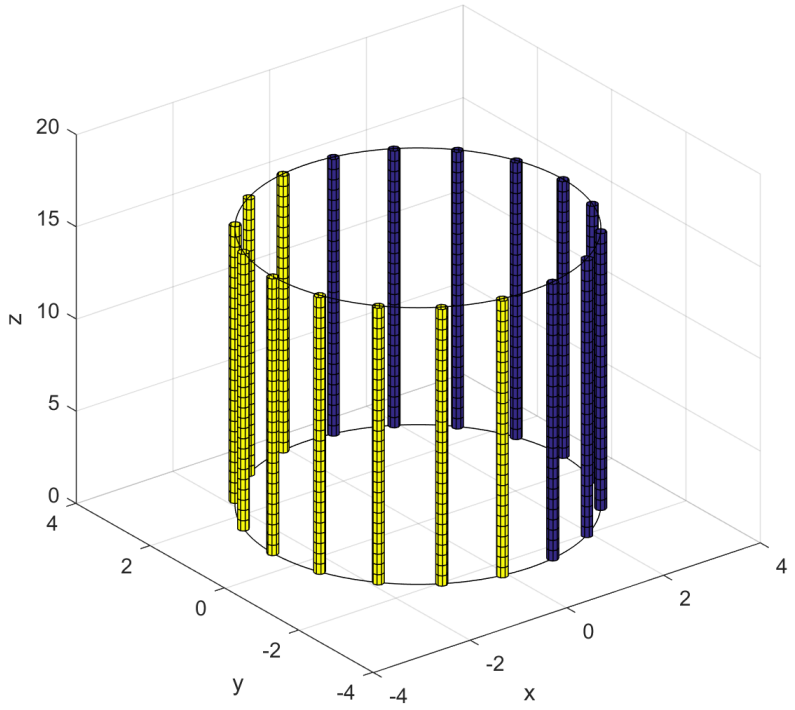

,

Figure 2.6: Receiver discretisation structure: eastern path (yellow) and western path (blue).

2.2.7 Receiver heat flux map correction

The main purpose of the geometrical discretisation is to analyse locally the heat transfer phenomena and solve the thermal problem in a accurate way. For this reason, Crespi-Zani heat flux output has been modified in order to be a suitable input for the present work.

As graphically reported in the next figures, the heat flux map is represented as a matrix in which the different rows stand for the receiver height discretisation (*j-index*)

and each column is referred to a pipes panel, discretising the receiver circumference (*p-index*) (figure 2.7 *a*).

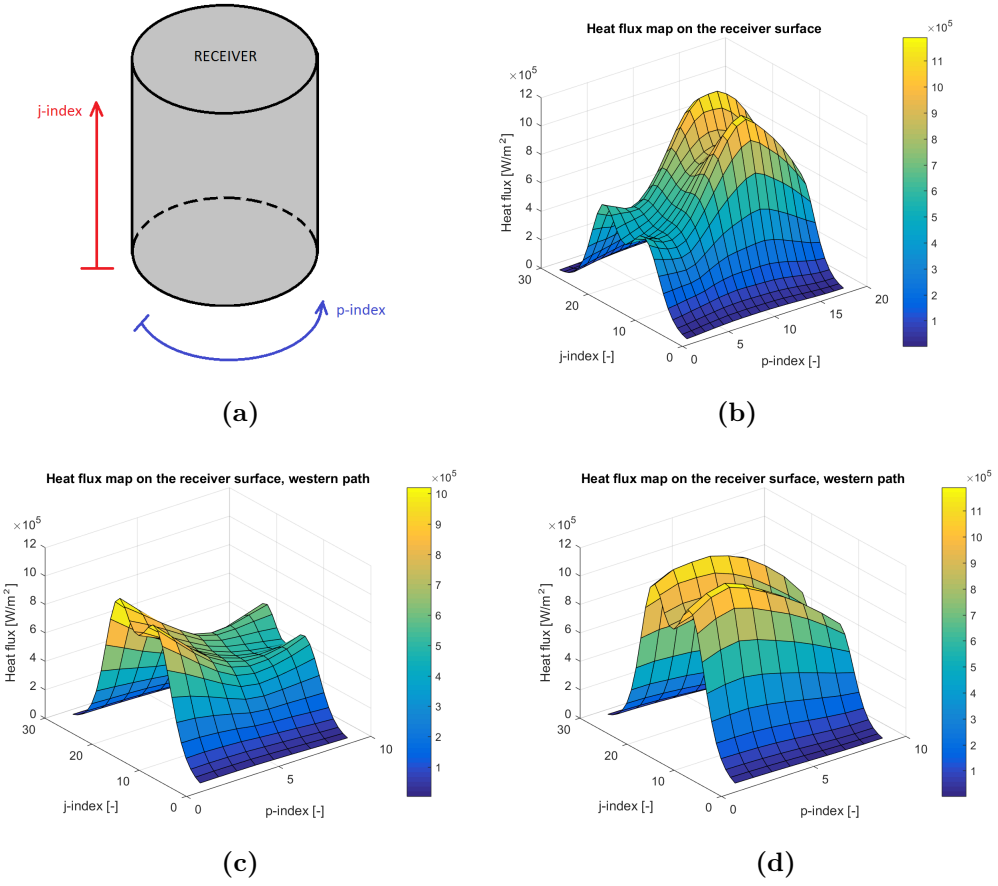

Figure 2.7: Receiver discretisation *a*) and heat flux map according to Crespi-Zani model *b*). On the other hand, *c*) western and *d*) eastern heat flux maps. Case of June at 3 pm.

Crespi-Zani's tool sets the starting point of the receiver circumferential discretisation (*p-index* = 1) on the south, proceeding in a clockwise direction (figure 2.7 *b*). On the other hand, as said before, the present model needs two radiation maps starting from north. For these reasons data have been reorganized in the two maps (figure 2.7 *c* and *d*) required according to the different convention of the present layout.

2.2.8 Other possible receiver configurations

After the description of the selected receiver model, two other possible layouts are hereby described and analysed. In particular these were the first two model attempts but, as it will be explained below, they do not represent a suitable solution for the thermal problem.

Parallel pipes and one pump configuration

The first idea was to adopt the same layout typically used in the case of a receiver with direct steam production. In this case no panel structure is considered since all the 432 pipes are placed in parallel (figure 2.8). As a consequence, the HTF mass flow rate coming from the cold tank is sent by a unique pump to the receiver and is automatically split among the various pipes.

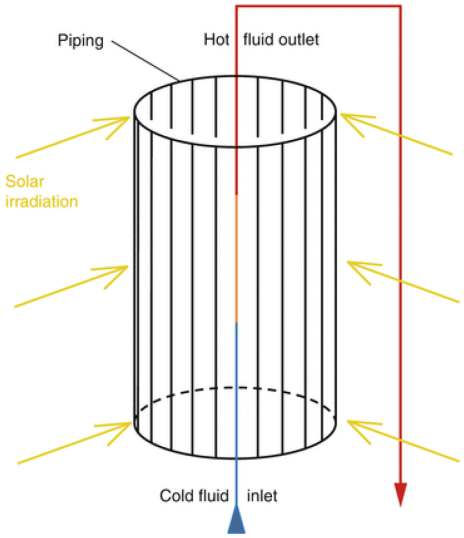

Figure 2.8: 432 parallel pipes layout.

The principal problem of this configuration is represented by the different warming up processes to which the solar salts are subjected depending on the pipes in which they are flowing. In fact, the heat flux map evolution on the receiver surface produces different HTF temperatures at the exit of each tube due to a different incident energy input on the pipes with same mass flow rate within. From a pipe material perspective this means that HTF is not able to properly control the pipe wall temperature: creep and excessive thermal stress conditions could be reached compromising the system security. On the other hand, in the northern portion of the receiver (where, as already seen, the incident radiation reaches its highest values) the molten salts receive an excessive heat flux and they can overcome the upper temperature limit, entering in the degradation region. This local departure from normal operating conditions generates instability in the system and must be avoided (figure 2.9).

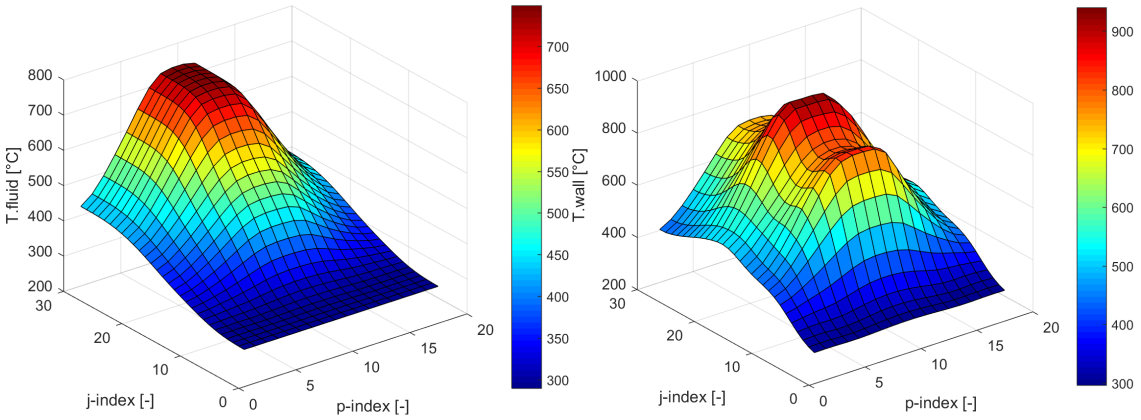

Figure 2.9: Results for the case of the 432 parallel pipes receiver: *a*) HTF and *b*) pipes temperature.

Parallel pipes and various pumps configuration

Starting from the previous idea, a similar layout has been tested starting from Pini's work ([32]). In this case the 432 parallel pipes are divided in a 18 panels framework, each of them served by an independent pump. In this way, a more complex control system could regulate the mass flowing in each tube in order to avoid excessive HTF temperatures.

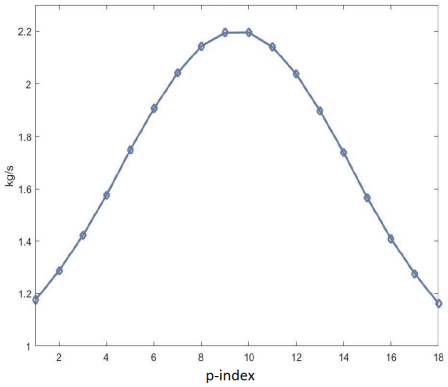

Figure 2.10: HTF mass flow rate produced with respect to pipes panels. Source: [32].

In particular, higher the heat flux incident on the pipes, higher the solar salts mass flow rate produced at the required conditions (2.10) HTF degradation problems are in this way solved but the regulation of the system results to be too complex and expensive due to the elevate pumps number. On the other hand high pipes wall temperature can be still verified.

After these considerations, it resulted mandatory to select a new layout structure and, as a consequence, the framework analysed in subsection 2.2.6 has been developed.

2.3 Stationary performance

In this section the solar receiver stationary model is proposed and the results obtained are analysed. The principal aim is to obtain a temperature map both for the receiver external surface and the HTF flowing within the pipes. These values are fundamental for the following transient analysis and for the receiver model consolidation.

The complex heat transfer problem regarding the whole receiver is hereby divided among the various flux units. In particular, for each of them a thermal balance is established considering radiative terms, thermal losses and HTF forced convection.

2.3.1 Thermal losses

Before facing the details of the iterative process used in the tool, it is necessary to explain in detail all the assumptions and considerations taken into account to design the receiver thermal model.

The solar radiation withstands several optical losses, as explained in section 1.1.5, and only a little part of it reaches the receiver. Moreover, the radiation that is effectively absorbed by the fluid inside the pipes is subjected to further thermal losses. A synthetic explication of the thermal process on the receiver external surface is showed in figure 2.11.

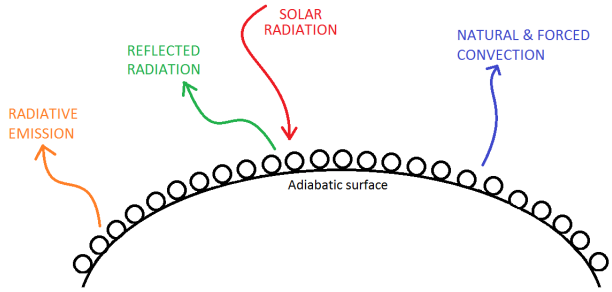

Figure 2.11: External thermal losses for the receiver.

As previously said, in the present model the losses due to the radiative emission and the conduction through the interior of the solar tower are not taken into account because considered smaller compared to the external ones. For those reasons the unirradiated portion of the pipes is considered as an adiabatic surface.

Concerning convection losses, both natural and forced components are taken into account. In particular, the latter can be modified varying the wind speed input data. Without any change the tools uses by default the value of 5 m/s, considered the average wind speed in Andalusia region.

2.3.2 Energy balance in a unit flux

The thermal model is implemented in Matlab and computes the energy flux exchanged with the solar salts and the relative losses for each single flux unit. An iterative process has been set up in order to find the external temperature of the receiver. The theoretical basis of the thermal phenomena is explained below.

Starting from the modified Crespi-Zani's output data (q_{field}) it is possible to calculate the heat flux approaching each of the irradiated circumferential portion of the pipe (q_{normal_i}). In this regard, a specific ϑ angle representing the different orientation of the solar radiation with respect to the normal to the *i-th* surface has to be introduced according to the problem geometry (figure 2.12).

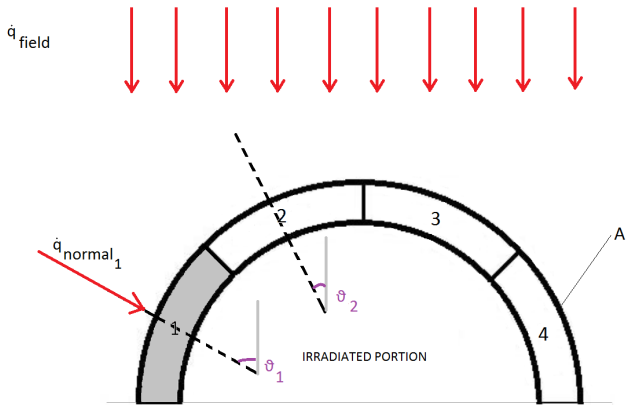

Figure 2.12: External thermal losses for the receiver.

	i=1	i=2	i=3	i=4
ϑ [°]	67.5	22.5	22.5	67.5

Table 2.2: ϑ values for each circumferential flux unit

$$\dot{q}_{normal_i} = \dot{q}_{field} \cdot A \cdot cos\vartheta_i \tag{2.2}$$

The amount of energy that HTF receives through the irradiated flux units is described by the following energy balance equations and moreover it is shown graphically in figures 2.13 and 2.14.

$$\dot{q}_{trans_i} = \dot{q}_{normal_i} - \dot{q}_{loss,rad_i} - \dot{q}_{loss,refl_i} - \dot{q}_{loss,conv_i} \tag{2.3}$$

In the previous formulation q_{trans} represents the effective solar radiation that

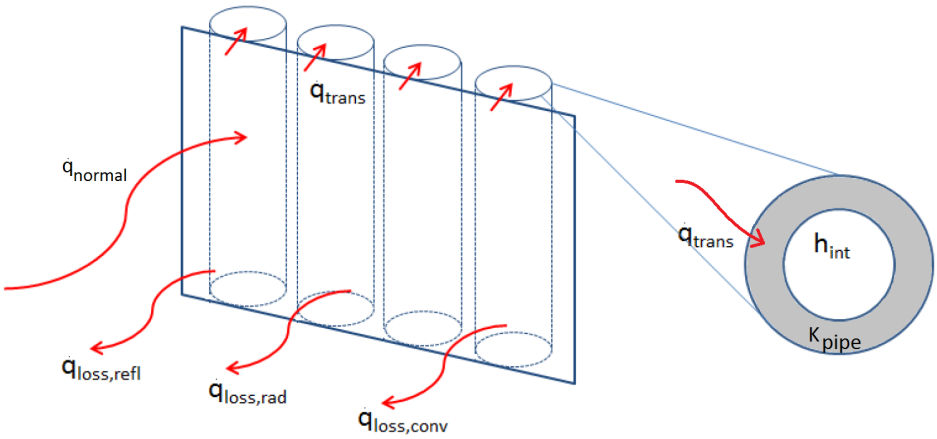

Figure 2.13: Thermal balance on the external surface of a single flux unit. In the present figure only 4 pipes are represented in order to not overload the drawing.

reaches the pipe wall after deducting all the losses terms. The latests are computed as follows:

- $\dot{q}_{loss,rad}$ is the amount of energy lost by radiation towards the ambient and it is described by Stefan-Boltzmann law.

$$\dot{q}_{loss,rad} = \varepsilon \cdot \sigma \cdot A \cdot F \cdot ({T_{wall}}^4 - {T_{sky-ground}}^4) \tag{2.4}$$

  As shown in equation 2.4, the emittance of a body is proportional to the 4-th power of the body temperature T_{wall}.
  ε is the emittance and it is represented by a number different from 1 due to the fact that the surface does not behave like a black body. Its value is found in literature ([25]) as a typical value for a solar receiver selective surface.
  σ is the Stefan-Boltzmann constant equal to $5.6704 \cdot 10^{-8}$ W/m^2K^4. A is the external area of the piece taken into account.
  $T_{sky-ground}$ is the mean value between the sky and the ground temperature because the receiver faces and, as a consequence, irradiates both of them.
  F is the view factor from the flux to the environment, assumed equal to 1. In this regard, the view factor from a unit flux to the one of the adjacent pipe is neglected while F_{ii}, the view factor that considers the emission part absorbed by the same flux unit, is set equal to 0 due to the convex geometry of the pipe.

- $\dot{q}_{loss,conv}$ is the amount of energy dissipated to the ambient due to surrounding air convection. This effect is both determined by the air density difference caused by the temperature gradient between ambient and pipe wall (*natural convection term*) and the air motion determined by wind (*forced convection*

term).

$$\dot{q}_{loss,conv} = h_{conv} \cdot A \cdot (T_{wall} - T_{amb}) \tag{2.5}$$

The heat transfer convective coefficient h_{conv} considers the effect of both the terms:

$$h_{conv} = h_{nat} + h_{forced} \tag{2.6}$$

In order to compute the heat transfer coefficient for the natural convection it has been chosen to use Churchill & Chu correlation [13].

$$Nu_L = 0.68 + \frac{0.67 \cdot Ra^{0.25}}{(1 + (\frac{0.492}{Pr})^{9/16})^{4/9}} \tag{2.7}$$

$$h_{nat} = \frac{Nu_L \cdot k_{air}}{L} \tag{2.8}$$

L is the characteristic length of the problem (the height of the flux unit) and k_{air} is the thermal conductivity of air. Ra is the Rayleigh number and is defined as follows.

$$Ra = Gr \cdot Pr \tag{2.9}$$

$$Gr = \frac{g \cdot L^3 \cdot \beta \cdot (T_{film} - T_\infty)}{{v_{air}}^2} \tag{2.10}$$

$$Pr = \frac{\mu \cdot Cp}{k_{air}} \tag{2.11}$$

In the above equations, Grashof number (Gr), characterizes the heat transmission for natural convection by describing the ratio between floating forces and viscous friction forces in a fluid. Pr, the Prandtl number, identifies the rate between cinematic and thermal diffusivity. g is the gravitational acceleration at ground level (9.81 m/s^2). As further specification, the Churchill & Chu correlation is valid if the flow is laminar, condition valid in the range of $10^{-1} < Ra < 10^9$, verified for the present problem.

All therm-physical air properties are computed at a mean film temperature (average value between the ambient and the external receiver temperature). In this regard, this value is not constant but changes alongside the receiver. For

this reason a table with all the properties is created with *EES* and then the correct value for each area is calculated with a data interpolation inside the code. Anyway, also for this case an approximation is done in order to reduce the computational time of the tool: instead of calculating all the properties of every *i-th* flux unit, they are calculated for the average temperature of the irradiated part of each annulus in which the units are included.

Regarding the forced convection produced by wind, an empirical formula by Sandia has been chosen:

$$h_{forced} = 0.197 \cdot v_{wind}{}^{1.849} \tag{2.12}$$

- $\dot{q}_{loss,refl}$ stands for reflection losses and depends on the material reflectivity ρ that characterizes the external surface of the receiver.

$$\dot{q}_{loss,refl} = \rho \cdot F \cdot \dot{q}_{normal} \tag{2.13}$$

Once analysed the reduction of incident radiation due to losses, the amount of heat that the HFT receives from the pipe *i-th* surface has to be computed. The latter is represented as $\dot{q}_{eff_i}$.

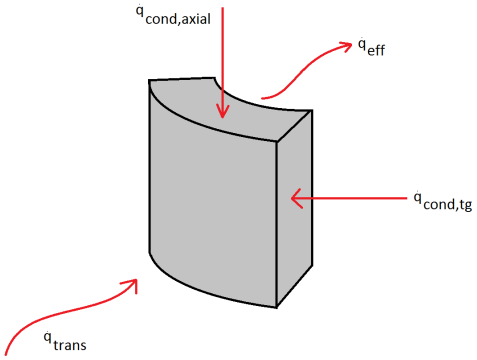

Figure 2.14: Thermal balance in the internal portion of the *i-th* flux unit underlining the axial and tangential conductive terms.

$$\dot{q}_{eff_i} = \dot{q}_{trans_i} + \sum \dot{q}_{cond,axial_i} + \sum \dot{q}_{cond,tg_i} \tag{2.14}$$

As evidenced in equation 2.14 and figure 2.14, the tangential conductive component ($\dot{q}_{cond,tg}$) and the axial one ($\dot{q}_{cond,axial}$) coming from all the adjacent flux units are taken into account. In this regard, if they are entering the considered flux unit they have positive sign in the above equation according to the convention (figure

2.14). In particular, $\dot{q}_{cond,tg}$ represents the heat transfer exchanged due to conduction through the tangential direction inside the pipe wall from the *i-th* flux unit to the adjacent $i+1$ one:

$$\dot{q}_{cond,tg_i} = \frac{T_{wall_{j,i}} - T_{wall_{j,i+1}}}{R_{tg}} \tag{2.15}$$

Note that if $i = 8$ is considered the model computes the heat exchanged between the 1^{st} and the 8^{th} flux units.

In the equation above, R_{tg} is the thermal resistance in the tangent direction, defined as function of external and internal radius, thickness t, material thermal conductivity k_{pipe} and flux unit length dx. The latter is obtained dividing the whole pipe length by the number of axial discretisation ($dx = L/28$).

$$R_{tg} = \frac{\pi \cdot (r_{ext} - r_{int})}{8 \cdot dx \cdot k_{pipe} \cdot t} \tag{2.16}$$

On the other hand, $q_{cond,axial}$ represents the axial heat conduction inside the pipe wall and is computed as follows.

$$\dot{q}_{cond,axial_i} = \frac{T_{wall_{j,i}} - T_{wall_{j+1,i}}}{R_{axial}} \tag{2.17}$$

Where $T_{wall_{j+1,i}}$ represents the pipe wall temperature of the same *i-th* unit flux on the successive annular division along the pipe length $(j+1)$.

The HTF temperature of the *j-th* annulus is then computed by the use of the Newton formulation:

$$T_{wall_{i,j}} = T_{fluid_j} + \frac{\dot{q}_{eff_i}}{A \cdot U} \tag{2.18}$$

$$U \cdot A = \frac{1}{R_{tot}} \tag{2.19}$$

where U is the overall heat transfer coefficient (also known as *global heat conductance*) of the flux unit and A is the reference area. According to the previous hypothesis HTF temperature is uniform on the whole annular section of the pipe due to turbulent flow.

For the solution purpose the electric analogy is then set. In this regard, the thermal resistances behave like the electric ones and the the heat flux is considered as a current. This methodology is valid for this case since there is no energy production inside the system. In particular, the relation between T_{fluid} and $T_{wall,ext}$ results to

be determined by the R_{tot} term, which is the sum of the thermal resistances both due to conduction and internal convection of the studied process.

$$R_{tot} = R_{cond} + R_{conv} \tag{2.20}$$

The fouling resistance is hereby neglected, in fact the pipes are considered clean as further simplifying assumption. As results, the overall system is described by figure 2.15.

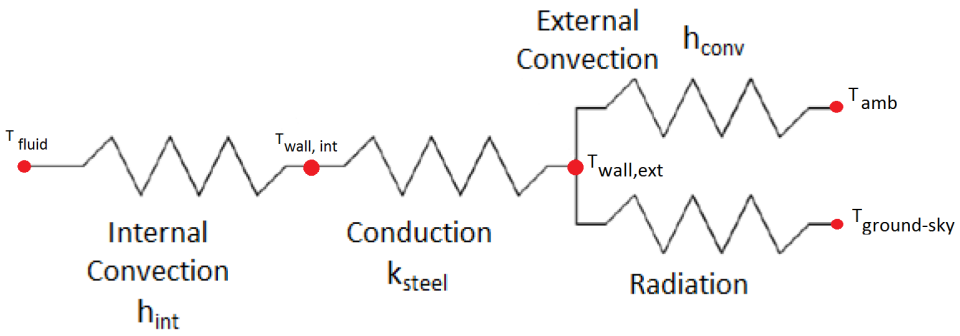

Figure 2.15: Electric analogy of the heat transfer process.

After the first modelling attempts, at a later stage the conductive resistance R_{cond}, considered for the case of the cylindrical geometry, has been neglected due to the low influence on the overall process. This assumption is verified from the theoretical point of view considering the Biot number. The latter measures the magnitude of the temperature differences in the pipe wall determined by the conductive term with respect to the magnitude of the temperature differences between pipe wall and surrounding fluid.

$$Bi = \frac{h_{conv} \cdot L_c}{k_{pipe}} \tag{2.21}$$

Substituting the characteristic values of the present problem the result is $Bi << 1$ which allows the application of the lumped parameter approach. This means that conduction heat transfer within the body can be neglected with respect to convection. Therefore equation 2.20 can be simplified in the form:

$$R_{tot} = R_{conv} \tag{2.22}$$

R_{conv} is the convective heat transfer resistance. Its computation is more complicated because one of the various empirical correlations that describe the behaviour of the forced flow in pipes has to be taken into account. In this regard, a specific subsection is dedicated to the purpose.

2.3.3 Molten salts internal heat transfer coefficient

The heat transfer coefficient of the single phase HTF flowing within the pipes is defined using the Gnielinski correlation (equation 2.23) and the other traditional heat transfer correlations:

$$Nu_D = \frac{\frac{f}{8} \cdot (Re_D - 1000) \cdot Pr}{1 + 12.7 \cdot \frac{f}{8}^{0.5} \cdot (Pr^{\frac{2}{3}} - 1)} \tag{2.23}$$

$$f = (0.79 \cdot ln(Re_D) - 1.64)^{-2} \tag{2.24}$$

$$h_{conv} = \frac{Nu_D \cdot k_{fluid}}{D_{int}} \tag{2.25}$$

$$Pr = \frac{\mu_{fluid} \cdot Cp_{fluid}}{k_{fluid}} \tag{2.26}$$

$$Re_D = \frac{\dot{m_{fluid}} \cdot D_{int}}{S_{pipe} \cdot \mu_{fluid}} \tag{2.27}$$

In the equations above Nu is the Nusselt number and describes the ratio between the heat exchanged by convection and the one by conduction. f is the friction coefficient between the fluid and the pipe wall and is obtained using the Petukhov formulation reported in equation 2.24. Re_D and Pr refer respectively to the state of motion of the fluid and to the ratio between cinematic and thermal diffusivity. D_{int} is the internal pipe diameter and S_{pipe} is the pipe cross sectional area through which the solar salts flow.

Variable		Value	Unit
Temperature	T_{fluid}	290	[°C]
Dinamic viscosity	μ_{fluid}	0.0043	$[m^2/s]$
Specific heat capacity	Cp_{fluid}	1498	[J/kgK]
Thermal conductivity	k_{fluid}	0.4922	[W/mK]
Density	ρ_{fluid}	1905	$[kg/m^3]$

Table 2.3: HTF properties at the receiver inlet section.

On the other hand, μ_{fluid}, Cp_{fluid} and k_{fluid} are the dynamic viscosity, specific heat capacity and the thermal conductivity of the HTF and they are computed autonomously by the present tool starting from the data provided by *EES*. An idea of the order of magnitude of HTF properties is given describing the molten salts conditions at the receiver inlet section, as reported in table 2.3.

2.3.4 Pressure drops

In parallel with respect to the thermal problem the tool evaluates also pressure drops in the system. The latter are fundamentals in order to accurately describe the entire receiver behaviour and avoid dynamic problems. In fact, proper pressure values in the pipes have to be guaranteed otherwise the flow will stop its proceeding generating the collapse of the whole system due to excessive temperatures. For this reason, in every power plant pressure losses are controlled by computerized valves.

Starting from the same friction factor f obtained by Petukhov equation, pressure losses are then evaluated for each annular pipe section as follows.

$$\Delta P_j = 4 \cdot f \cdot \frac{L + L_{eq}}{D_h} \cdot \left(\frac{1}{2} \cdot \rho_{fluid_j} \cdot {v_{fluid_j}}^2 \right) \tag{2.28}$$

D_h is the hydraulic diameter, ρ is the density, v_{fluid} is the molten salts velocity inside the pipe and f,as already mentioned, is the friction coefficient between the fluid and the pipe wall obtained from equation 2.24. Furthermore, L is the pipe length and L_{eq} represents the losses due to curves, section changes and valves that specify the circuit characteristics.

Finally the code calculates pressure losses at each iteration along with the solution of the thermal problem.

$$P_{j+1} = P_j - \Delta P_j \tag{2.29}$$

2.3.5 Operating principle of the algorithm

In this section the *Matlab* code control logic based on the previous thermodynamic principles is defined.

From a numerical point of view, the main issue is represented by the two temperatures unknown in each flux unit thermal balance equation. In fact, both the wall pipe and the HTF temperature results to be defined. Furthermore the solar salts mass flow rate that the receiver can guarantee at the designed conditions has to be computed. As a consequence of the high number of unknowns more than one iterative cycle has to be set.

The solution proposed is based on the assumption of considering the fluid in a *j-th* annular section at the same temperature with respect to the section inlet. In this

way, for both eastern and western HTF paths, it is possible to start the computation from the first annulus ($j = 1$) of the characteristic tube of the first panel ($p = 1$) setting the molten salts temperature $T_{fluid_{j=1,p=1}}$ equal to the cold tank temperature. The wall pipe temperatures of each *i-th* section of the annulus can be then founded by iteration process.

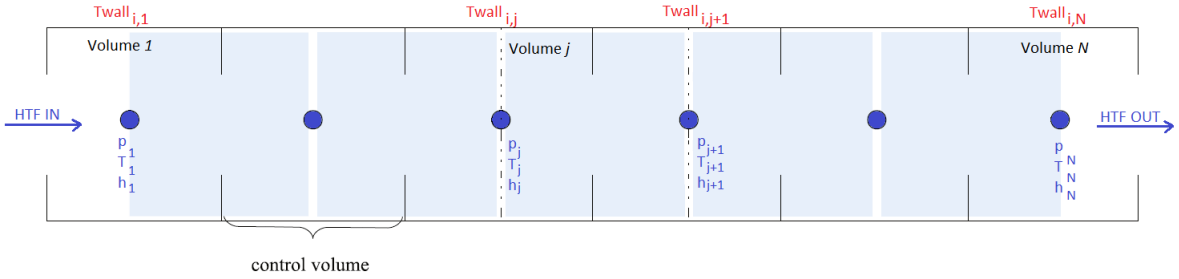

Figure 2.16: *p-th* pipe discretisation scheme according to convention.

Once known $T_{wall_{i,j=1,p=1}}$, all the losses and the net heat flux $\dot{q_{eff_i}}$ absorbed by the HTF can be evaluated using the previous equation.

$$\dot{q}_{tot_{j,p}} = \sum_{i=1}^{8} \dot{q}_{eff_{i,j,p}} \tag{2.30}$$

$\dot{q}_{tot_{j,p}}$ represents the amount of heat that the fluid receives from the whole annular section, composed by the heat portions coming from the eight flux units of the annulus.
The further step is to compute the fluid temperature for the next annulus (*j+1*):

$$T_{fluid_{j+1,p}} = \frac{\dot{q}_{tot_{j,p}}}{\dot{m}_{fluid} \cdot Cp_{fluid_{j,p}}} + T_{fluid_{j,p}} \tag{2.31}$$

Applying the same methodology along the entire pipe length for each of the panels that compose the fluid path it is possible to solve the whole thermal problem. By the way, the HTF mass flow rate has still to be computed and, as a consequence, a further external iteration cycle has to be set. For sake of simplicity the whole code logic is explained in a graphical way in the following flow-chart.

1. First of all the required inputs have to be loaded. From *EES* database both air and molten salts properties are obtained for a wide range of temperature and pressure. From these values the tool autonomously computes fluid properties by interpolation. After that Crespi-Zani's *Solar Tool 5* is launched and the user is free to select the proper aiming strategy, day and hour of the analysis and cloud type. Finally the receiver geometry data are loaded by the compiler

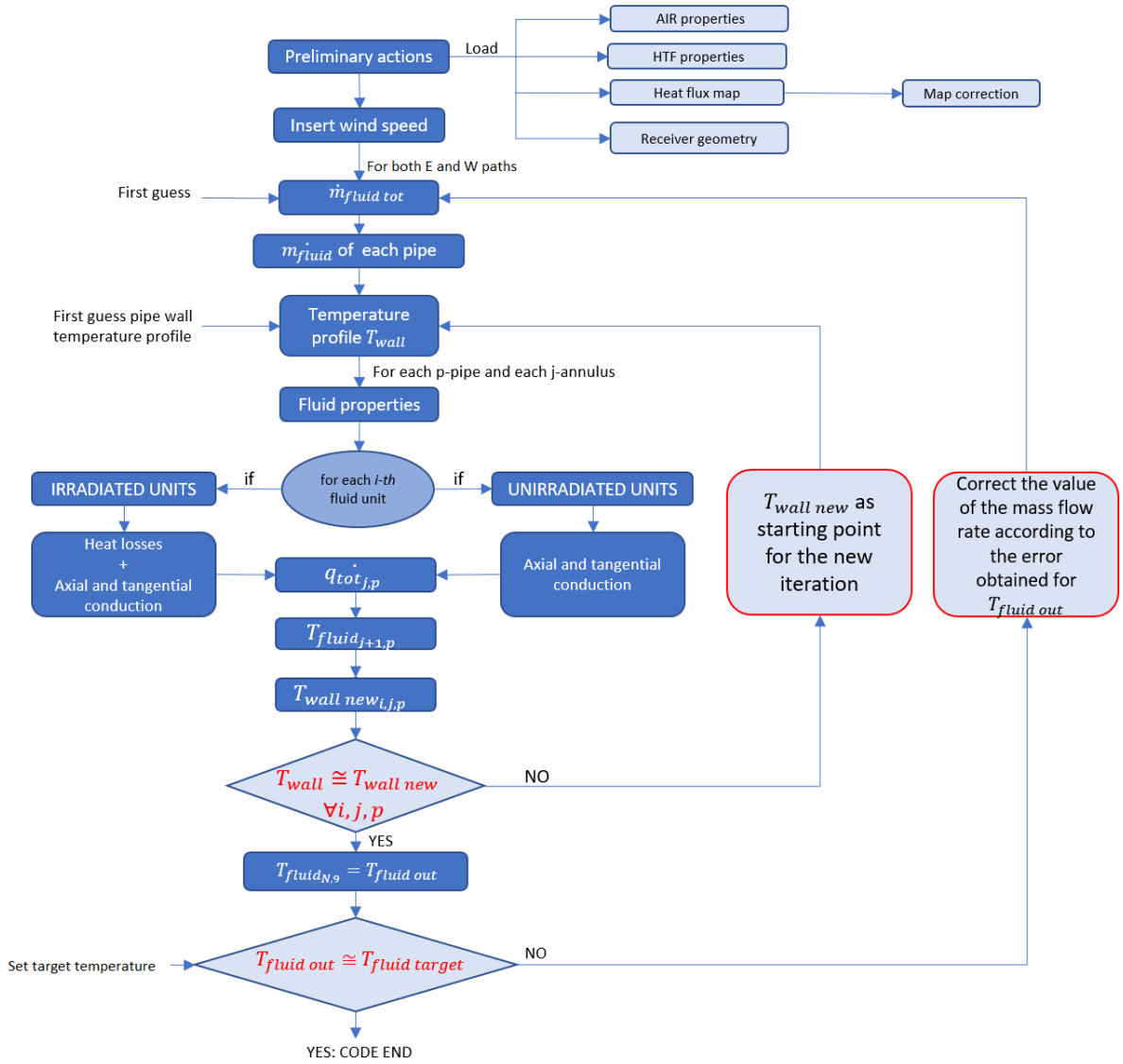

Figure 2.17: Matlab logic operating principle of the stationary problem.

and it is asked to introduce the wind velocity completing the desired ambient conditions.

2. The code proceeds setting default values as first guess for both HTF total mass flow rate and pipe wall temperature profiles in order to reduce the number of unknowns. After that, it enters in the iterative process firstly for the western path case and then for the eastern one.

3. Starting from the first annular section of the first pipe (j=1,p=1), thermal balance equations are set in order to calculate the amount of heat transferred through the pipe to the molten salts. In this regard, the case of an irradiated flux unit with respect to an unirradiated one is distinguished.

4. HTF temperature profile in the pipe is computed using equation 2.31 for each annular section. From the obtained value it is possible to calculate the new pipe wall temperature that guarantees the thermal equilibrium in the flux unit.

5. Error between T_{wall} and $T_{wall,new}$ is evaluated for each flux unit: if the inaccuracy is greater than the tolerance accepted the code comes back to point 3 through a *while* function and uses $T_{wall,new}$ as new starting value.

6. Once solved the thermal problem, it is checked if the mass flow previously set guarantees the HTF outlet designed temperature or not. In this regard, at constant incoming radiation, higher the mass flow rate imposed, lower the outlet molten salts temperature obtained. Through a second *while* function the compiler iterates in this loop modifying $\dot{m}_{fluid,tot}$ up to the moment in which the required conditions at the outlet section are satisfied.

7. This sequence is repeated for both eastern and western paths case. Default graphical results are displayed for both HTF and pipe wall temperatures.

2.3.6 Results for the stationary conditions

In this section the results of the analysis previously described are provided and examined. In particular, the tool provides a series of 2D and 3D graphs that simplify the comprehension of the receiver thermal performances particularly useful useful for data analysis purposes. All the results are referred to the 21^{th} March 12 am conditions.

HTF temperature graphs

In the following graph, HTF temperatures are reported for both eastern and western paths. A 3D chart framework is selected in order to provide the global imagine of the temperature evolution both in the axial and circumferential directions of the receiver.

In his original idea, figure 2.18 tries to represent the HTF system if an infrared picture of the entire receiver was taken from a northern perspective. In fact, being the area in which the HTF coming from the cold tank enters in the receiver, it is possible to denote the colder temperatures of the molten salts (depicted in blue). Proceeding along the receiver circumferential direction in a clockwise and anticlockwise direction the HTF warms up to the desired conditions and exits in the back part of the receiver (pipes depicted in red).

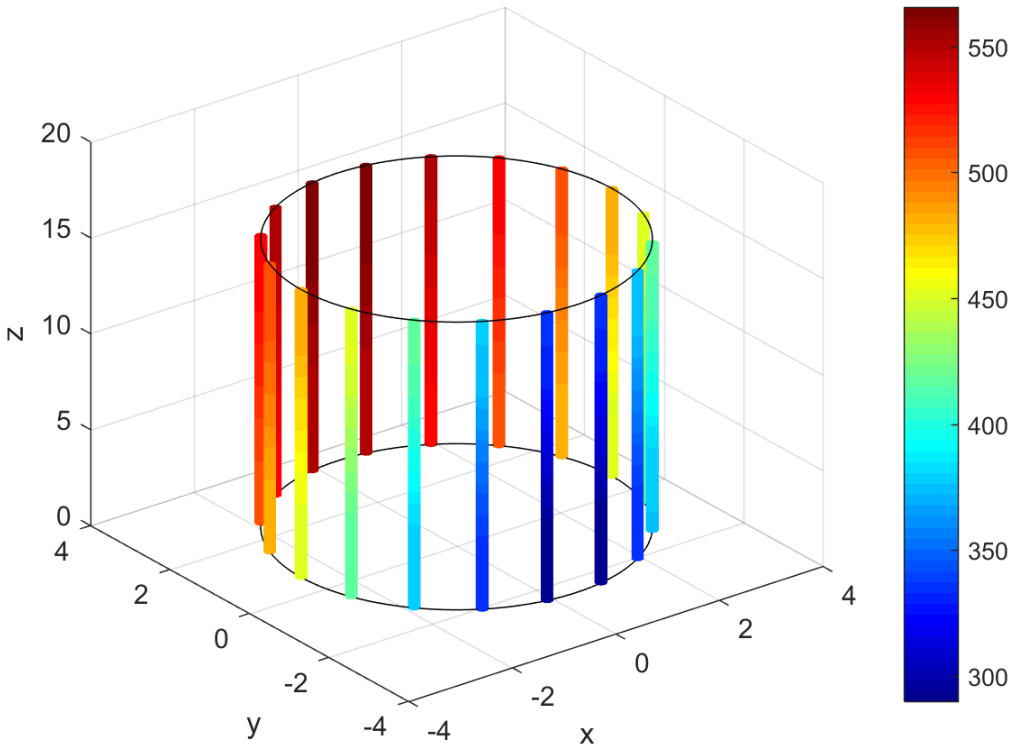

Figure 2.18: HTF temperature as from an infrared picture (March 12 am, aiming strategy 6). Northern side in the foreground.

Upper and lower HTF temperature limits are verified by a more traditional 3D representation (figure 2.19). In this regard, solidification and degradation problems are surely avoided and, as a consequence, the effective quality of the designed model is confirmed.

Apparently the molten salts warm up process seems to be symmetric between eastern and western path and equally distributed among the pipes. The former hypothesis is correct being the heat flux map representative of the 12 am solar position and, as a consequence, the resulting radiation values are symmetric on the heliostats field with respect to the tower position. On the other hand, as evidenced in the 2D graph below (figure 2.20 *a*) the latter hypothesis was only the result of an optical illusion.

In fact, ΔT_{fluid} between inlet and outlet pipe sections depends on the heat flux variation along the receiver. In particular higher the heat flux on the receiver surface, higher the HTF temperature variation inside the tube. For this reason, the highest temperature increase is located in the northern region entrance tube (p=*1*). On the other hand, proceeding to the southern area of the receiver ΔT_{fluid} decreases as the heat flux decreases. A further confirmation of the heat flux decreasing trend

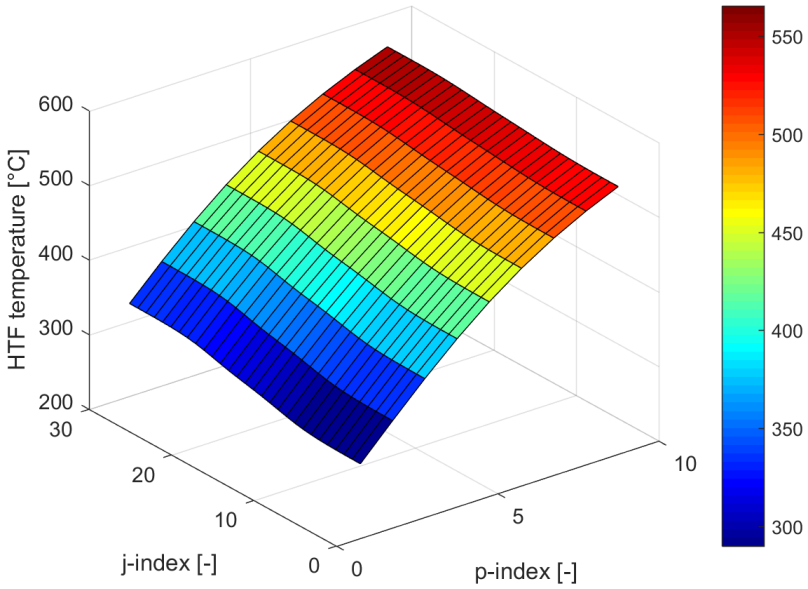

Figure 2.19: HTF temperature surf map (March 12 am, aiming strategy 6, western path).

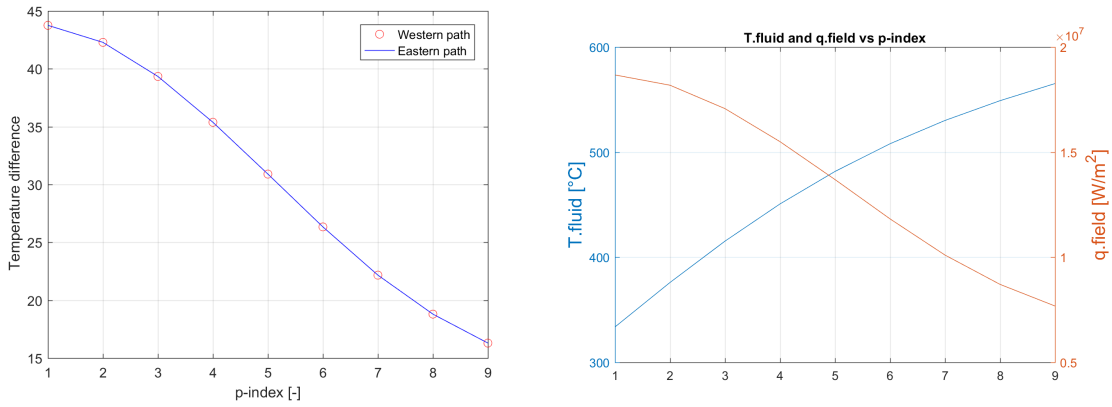

(a) **(b)**

Figure 2.20: HTF temperature increase in each pipe, comparison between western and eastern path *a*). Western path HTF warm up process with respect to total heat flux on the tube *b*).

proceeding in the p-index direction is evidenced in figure 2.20 *b*.

The latter also evidences how the areas subjected to the maximum incident flux are the ones in which the colder HTF flows. This result is the confirmation of the main design assumption. In that way it is in fact possible to properly control pipe wall temperatures that otherwise would reach excessive values.

Pipe wall temperature graphs

In this subsection attention is focused on the pipe wall temperature of the receiver. The following pictures aim to represent how would be the system if an infrared picture was taken for both receiver sides.

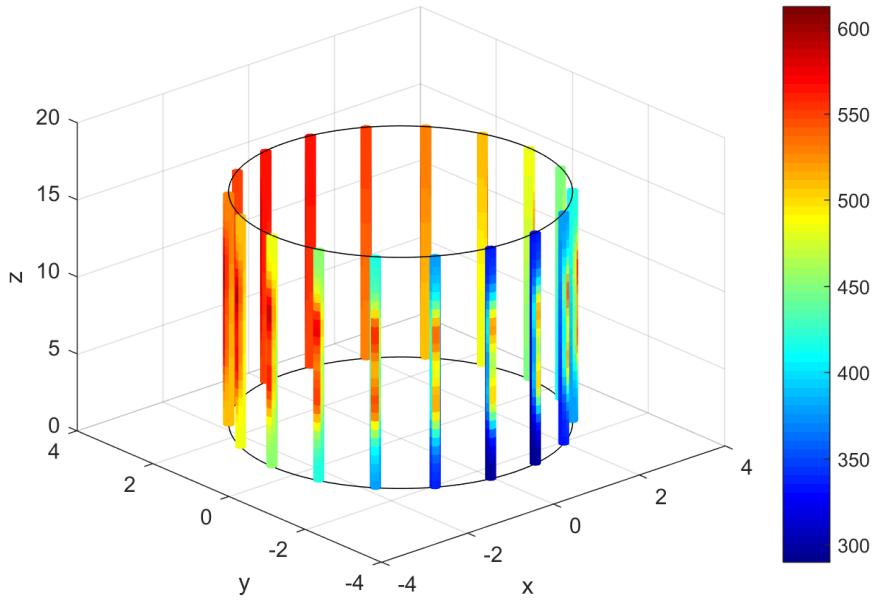

(a)

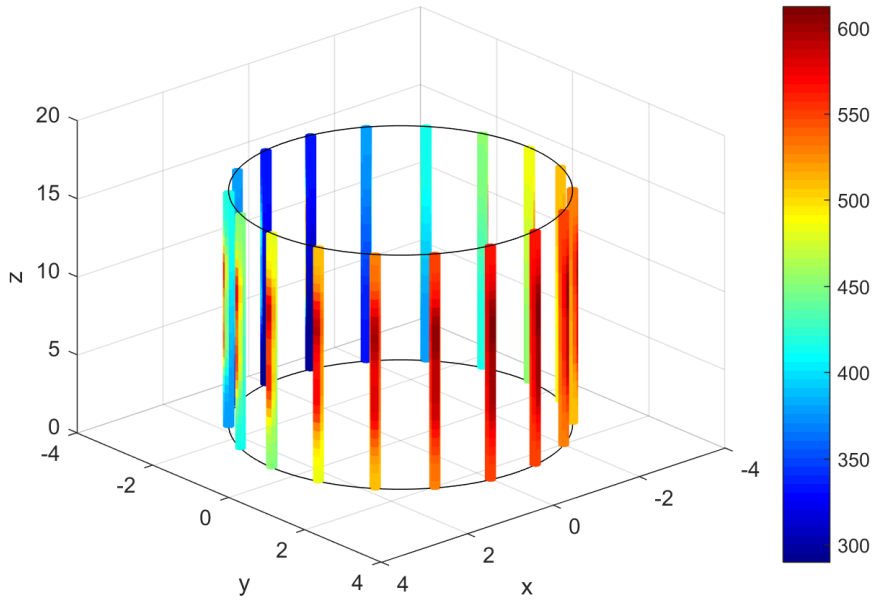

(b)

Figure 2.21: Pipe wall temperature [°C] as from an infrared picture: *a*) Northern side vs. *b*) southern side perspective.

As evidenced in the colorbars, none of the 4032 flux unit suffers from critical pipe wall temperature conditions. In fact, the pipe material can withstand temperatures up to 800°C, while the maximum value reached by the pipe system is 612.4°C in correspondence of the southern side. Here the highest temperature are verified for the HTF providing less heat absorbing capacity. As a consequence, even if the solar incident radiation is characterised by the lowest values the pipe wall temperatures are the highest one.

Furthermore, observing figure 2.21 *a*) and *b*), it possible to appreciate both tangential and axial thermal equilibrium on the external receiver surface. In this regards, two peak areas are outlined more or less at the middle of the pipe length. This behaviour is caused by the nature of the heat flux map coming from Crespi-Zani tool. In fact, looking back to figure 2.7, two peak areas on the radiation maps due to the aiming strategy are observed too. As a consequence, a straight correlation between heat flux map and pipe wall temperature is underlined: higher the peak of the heat flux incoming to the receiver surface, higher the temperature peak verified on the pipes wall surface. The same phenomena is verified also in figure 2.22, even if a main temperature among the 8 flux units is considered for each pipe annulus. By the way, the chart purpose is to evidence the main temperature at which heat is exchanged from pipes wall to molten salts.

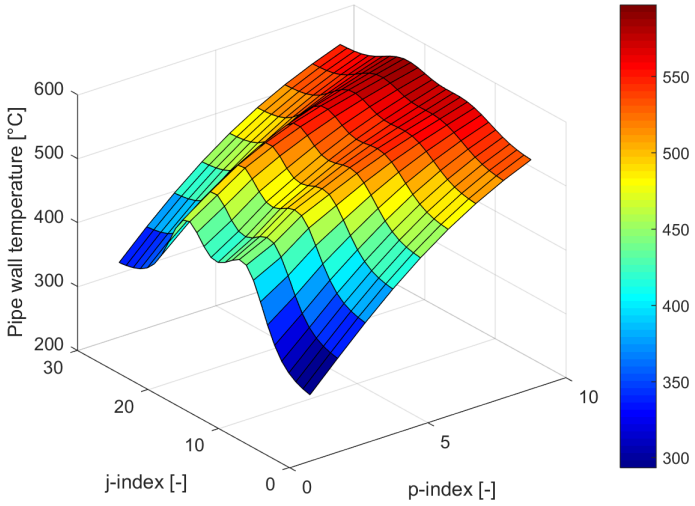

Figure 2.22: Pipes wall temperature surf map: for each *j-th* annulus the average temperature among the flux unit is considered.

Last but not least, the connection between HTF and pipes wall temperature is shown in figure 2.23. For this purpose an additional *jj* index is introduced. The latter represents the proceeding of a single HTF particle along the whole path (western

or eastern), following its motion through the various pipes, one after the other. In this way, *jj=1* represents the inlet section (first section of the first pipe: *p=1, j=1*) on the other hand *jj=252* represents the outlet section (last section of the last pipe: *p=9, j=28*).

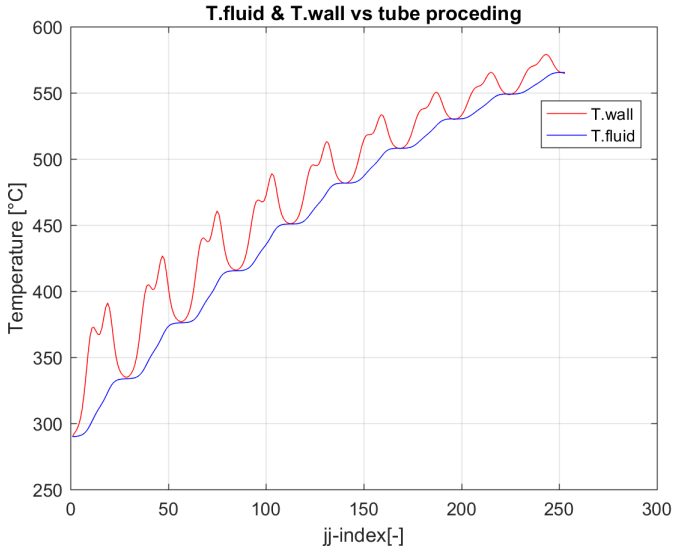

Figure 2.23: Comparison between HTF and pipe wall temperature profile.

The higher temperature difference between HTF and pipe wall is verified for the case of the first pipe ($1 < jj < 28$), where, as already said, the radiation map has the highest values and molten salts enters at the temperature conditions imposed by the cold tank. Proceeding along the receiver path the temperature difference is reducing as the HTF are warming up and the heat flux is reducing. In the same j-index increasing direction is possible to observe a peaks reduction due to the decrease in the heat flux values.

HTF mass flow rate

The main purpose of the receiver is to produce a certain amount of molten salts at the desired thermodynamic condition for the further steam generation. As a consequence, beside the thermal problem the mass flow production rate has to be analysed.

The following table (2.4) reports the HTF mass flow rate that the modelled receiver is able to guarantee according to month and hour during the year. On the other hand, in table (2.5) is reproduced the average heat flux available from *Solar Tool 5* from both the western and eastern sides of the receiver.

For this analysis three representative case of study are hereby considered:

- *21st March 12 am* is the design condition of the receiver power plant;
- *21st June 12 am* represents the condition of maximum solar radiation;
- *21st December 9 am* is considered the condition of minimum solar radiation.

		$\dot{m}_{fluid,west}$ [kg/s]	$\dot{m}_{fluid,east}$ [kg/s]	$\dot{m}_{fluid,tot}$ [kg/s]
21st March	12.00 am	212.4	211.3	423.7
21st June	12.00 am	214.5	212.9	427
21st December	9.00 am	180.1	174.5	354.6

Table 2.4: HTF mass flow rate with respect to month and hour.

As reported, the average radiation conditions coming from the solar field ($q_{field,tot}$) for March do not differ too much with respect to June and, as a consequence, the same behaviour is respected by the similar values of the HTF mass flow rate produced in those conditions. On the other hand, on December a reduction of 14% of the average heat flux with respect to the designed condition provokes a 16.5% decrease in the HTF produced in the receiver.

		$\dot{q}_{field,west}$ [kW/m^2]	$\dot{q}_{field,east}$ [kW/m^2]	$\dot{q}_{field,tot}$ [kW/m^2]
21st March	12.00 am	481.97	479.87	480.92
21st June	12.00 am	489.20	486.68	487.94
21st December	9.00 am	417.07	410.8	413.71

Table 2.5: Avarage incident radiation with respect to month and hour.

Receiver thermal efficiency

Once computed the HTF mass flow rate is possible to conclude the stationary analysis evaluating the thermal efficiency of the receiver for the considered conditions.

$$\eta_{th} = \frac{\dot{m}_{fluid,tot} \cdot Cp_{fluid,mean} \cdot (T_{fluid,out} - T_{fluid,in})}{\sum_i \dot{q}_{field_i} \cdot A_i} \tag{2.32}$$

where $\sum_i \dot{q}_{field} \cdot A_i$ is the overall energy that the solar field can provide to the receiver. This value is computed as sum of the heat flux incident to each *i-index* unit ($\dot{q}_{field_i}$) multiplied by the unit area (A_i).

		η_{th} [-]
21^{st} March	12.00 am	0.85
21^{st} June	12.00 am	0.86
21^{st} December	9.00 am	0.84

Table 2.6: Receiver thermal efficiency with respect to month and hour.

2.3.7 Model comparison

In this subsection a model tool comparison is proposed. In this regard, it was not possible to properly validate the developed model output with respect neither to real values of the power plant nor to other models that used the same initial conditions.

In fact, no data provided by *Torresol Energy Investment* are available in literature regarding the specific working condition of Gemasolar power plant and, as a consequence, the tool effectiveness could be only demonstrated through the main results comparison with respect to external receiver models developed for scientific publications purposes.

The main elements to be checked for the comparison are the incident heat flux considered as input and the size of the considered receiver. In this regard, the main problem is evidenced by both the different geometries and radiation adopted. As shown in table 2.7, these parameters differ significantly with respect to the ones used as input in the present model. As a consequence, they do not allow a precise validation but they only provide a general check of the performances of the model.

		Model	Ref. [11]	Ref. [36]	Ref.[34]
nr° panels	[-]	18	18	18	18
$D_{receiver}$	[m]	8	6	6	6
$H_{receiver}$	[m]	16	7.4	7.4	7.4
$d_{ext,pipe}$	[m]	0.0422	0.0422	0.0422	0.0422
$\dot{q}_{field,max}$	[kW/m^2]	1330	1250	1200	1600
$\dot{q}_{field,mean}$	[kW/m^2]	480	794	800	-
η_{th}	[-]	0.86	0.87	0.78	0.83
$\dot{m}_{fluid,tot}$	[kg/s]	423	600	560	395
$T_{wall,max}$	[°C]	612	640	715	588

Table 2.7: Model comparison, design case 21^{st} March 12 am.

As results, some considerations can be made about the different values reported above:

- The differences in the receiver size, especially in height, is considerable. For

all the references, the receiver area is smaller and the heat flux resulted more concentrated causing higher pipe wall temperatures.

- Even if for both Ref.[11] and Ref.[36] cases Andalusia region was the same location choice, a different radiation map characterised by higher average value with respect to Crespi-Zani's output has been adopted. This heat flux difference is at the basis of the variation in the main results. On the other hand, Ref.[34] does not provide the average radiation value used in the computation.

- The receiver thermal efficiency is very similar for the case of Ref.[11] and Ref.[34]. On the other hand, the higher temperatures reached by Ref.[36] cause additional thermal losses due to both convection and emission heat exchange from the receiver surface to the environment leading to a significant thermal efficiency reduction.

- All the cited authors do not consider the tangential conduction component in their heat transfer model. In this regard, the present dissertation improves the temperatures profiles accuracy providing more reliable results through which describe the real thermal phenomena.

- In the present work Cp values are interpolated with respect to temperature as done in Ref.[11] case. On the other hand, Ref.[36] considers a constant value of 1500 J/kg K for sake of simplicity.

- Considering the same target condition for the HTF but different average values for the heat flux map, the resulting molten salts mass flow rates differ of a 30% between the present and the other works. This difference can be explained considering the different amount of energy that heliostats field provide to the receiver and the comparable value of the thermal efficiency among all the cases.

- In the Ref.[34] the mass flow rate was set as target object rather than the required outlet HTF temperature and, as a consequence, it does not represent a suitable validation reference with respect to the present model.

As further comparison, Ref.[11] results for both HTF and pipe wall main annular temperature are reported and compared to the same ones obtained through the present model (figure 2.25 *a* and *b*).

The two charts present the same general behaviour, by the way the HTF heating process appears to be more linear in Ref.[11]. In this regard, higher pipe wall temperature peaks are appreciable in the central part of the receiver, meaning a less homogeneous radiation map along the pipe length. On the other hand, in the present work the nature of the heat flux map sets two lower peaks in the central part

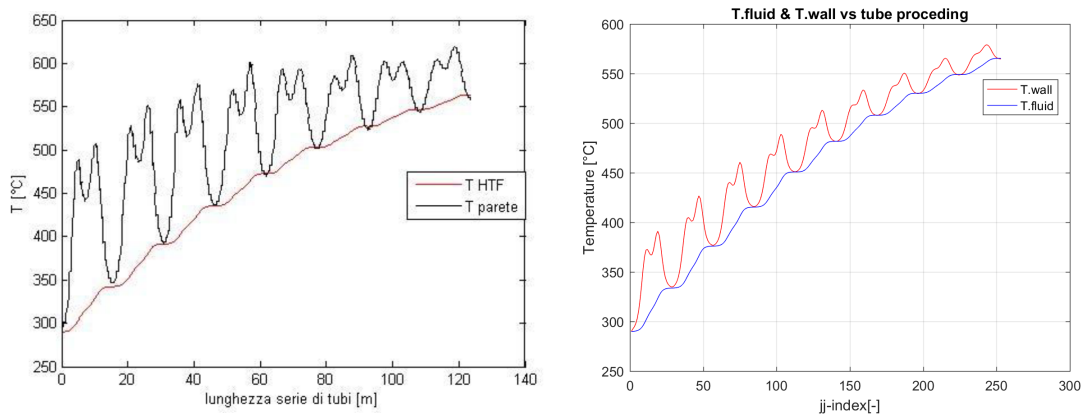

Figure 2.24: Comparison between HTF and pipe wall temperature profile. *a*) Ref.[11] case vs *b*) present model.

of the receiver causing the same trend in the pipe wall temperatures.

In a later stage, Ref.[36] authors, Sanchez and Rodriguez, revised their work providing a further publication ([37]) taking into account tube wall temperature variations according to the incident solar-flux distribution. From a graphical perspective, Ref.[37] results appear in line with the ones obtained through the present work and reported in figures 2.23 and 2.21.

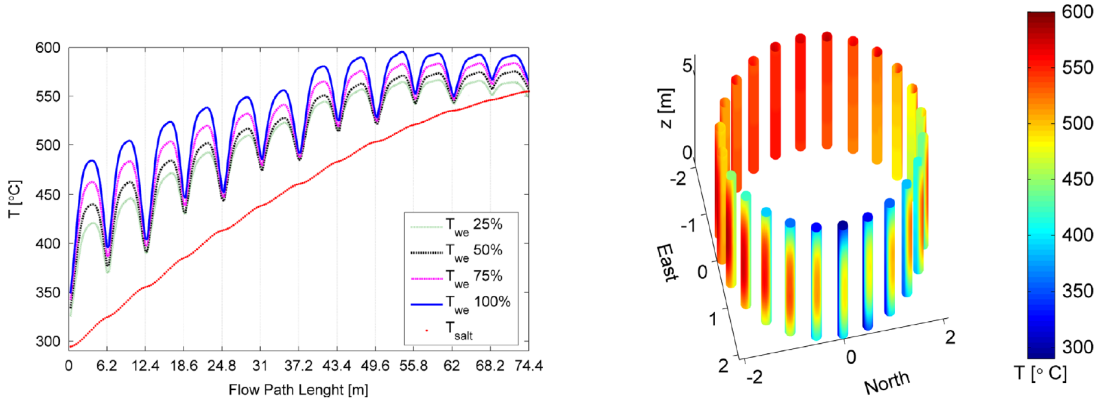

Figure 2.25: Ref.[37] results - *a*) Pipe wall and HTF temperature 2D chart and*b*) Pipe wall temperatures 3D chart.

Furthermore, the same authors proposed a new receiver design ([35]) in which receiver panels are formed by bayonet tubes instead of circular pipes. Each bayonet pipe is constituted by two concentric tubes joined by a bayonet end-cap in one of its ends. Regarding operation mode bayonet receivers have two possible flow directions. The cold fluid can be pumped into the inner tube and then the hot fluid flows out through the annular gap (inner bayonet); or else the cold fluid can enter

by the annular gap and exits hotter by the inner tube (outer bayonet). With this new structure they demonstrated soften wall and film temperatures, lower thermal stresses due to a more homogeneous wall temperature, and lower corrosion rate. By the way, a comparison with this reference has not been considered suitable due to the huge differences in the receiver modelling structure.

2.3.8 Aiming strategies analysis

In this subsection the validated stationary model is used to analyse which of the available aiming strategies represents the best option from both a maximum wall temperature and receiver thermal efficiency perspective.

Crespi-Zani's work assures that aiming strategy 6 is the one that obtains the lowest heat flux peak values in the radiation map. The following step is to demonstrate if this strategy, compared to the other, also assures the lowest peak values on the temperature profile for the pipes wall. In this regards, the code is launched using as input the radiation maps obtained with aiming strategy 1, 2 and 4 for the case of 21^{th} March at 12 am. These strategy are considered the second best option after the number 6, according to Crespi-Zani's analysis. Aiming strategies 3 and 5 introduce excessive spillage losses and, as a consequence, are kept out from the present investigation. The results obtained as output are successively modified in order to evidence the maximum pipe wall temperature for each of the tube annular section. As shown in figure 2.26, apart from the aiming strategy 1 which produces a extremely high temperatures peak the other strategies show a very similar behaviour. By the way, few differences can be evidenced:

- Aiming strategy 4 chart presents two very similar peaks situated at the middle of pipe length. If the higher one is identical with respect to the one produced by aiming strategy 6 in the same position, the first peak from the bottom presents higher temperature with respect to the same reference strategy 6;
- Aiming strategy 2 is characterized by an extended plateau in the central part of the chart, meaning an ample receiver surface at maximum temperature.
- Aiming strategy 6 chart shows two peaks with different height: if the upper one has the same shape of the ones of the other aiming strategies the bottom one presents lower values. Furthermore, the curve slope moving on the j-index axis suggests how the temperature gradient is slightly lower with respect to the other case.

By the way, these considerations do not allow to fully promote aiming strategy 6 as the best one from the pipe wall temperature perspective even if a slight advantage

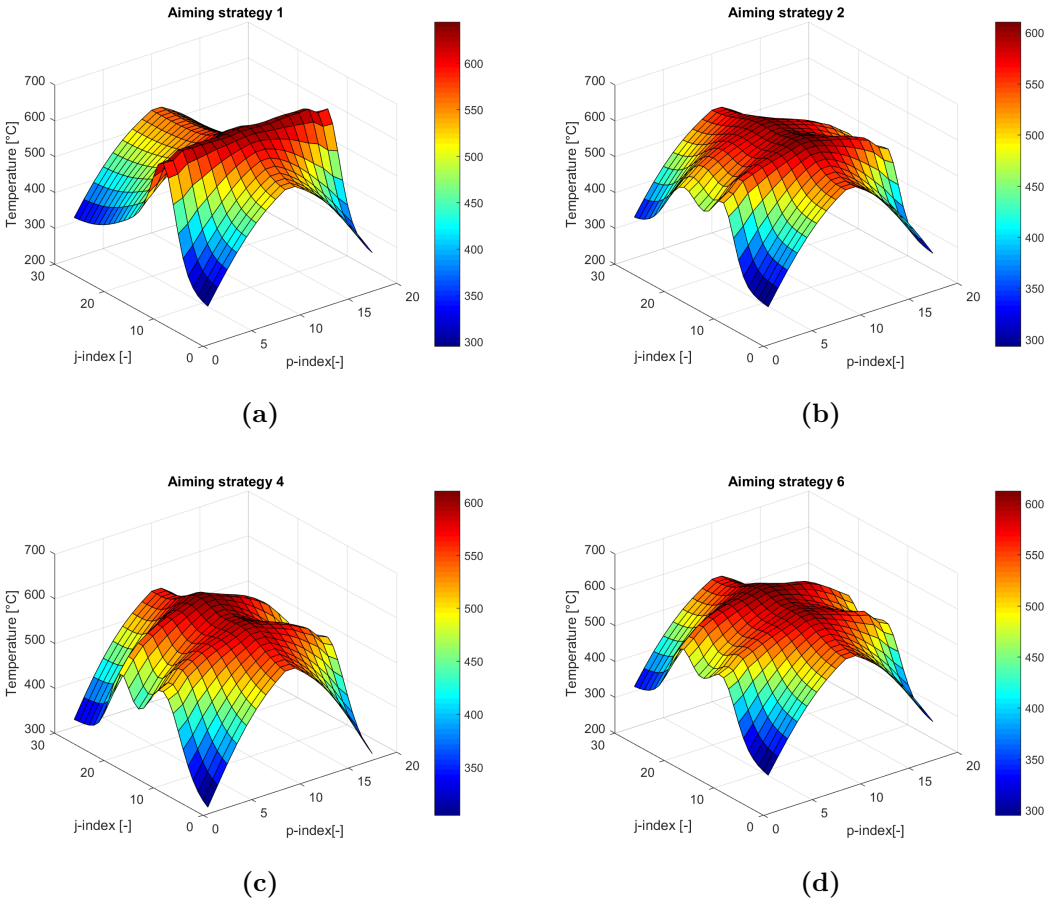

Figure 2.26: Maximum pipe wall temperature comparison: *a*) aiming strategy 1, *b*) aiming strategy 2, *c*) aiming strategy 4, *d*) aiming strategy 6.

can be evidenced anyway. New parameters have to be taken into account to enlarge the basic elements of the analysis: HTF mass flow rate and receiver thermal efficiency.

In this regard, as shown in table 2.8 aiming strategy 6 guarantees the highest value for the HTF mass flow rate at the desired outlet condition and, as a consequence, is the strategy that provide the highest receiver thermal efficiency.

	$\dot{m}_{fluid,tot}$ [kg/s]	η_{th} [-]
Aiming 1	419.8	0.84
Aiming 2	420.8	0.85
Aiming 4	417.9	0.84
Aiming 6	423.7	0.86

Table 2.8: Receiver thermal efficiency with respect to month and hour.

With the last results, it is now possible to confirm Crespi-Zani work demonstrating aiming 6 as the best strategy also from the point of view of the stationary regime.

2.4 Transient performance

In this section a model of the transient performances of the solar receiver is proposed. The results obtained in section 2.3 and the theoretical assumptions made in 1.4 are now used as input of the present model. In the designed scenario in fact, starting from the stationary operating condition, the receiver is subjected to a time-changing heat flux map due to different clouds passage over the heliostats field that modifies the solar incident radiation.

Under these particular conditions both the receiver pipe wall temperatures and the molten salts conditions are changing in time. In this regard, the aim ot the model is to evaluate all the important parameters in order to forecast the conditions in which the system can evolve providing a suitable and accurate tool for the further control system analysis.

2.4.1 Time modelling

Crespi-Zani's *Solar Tool 5* is used also in this case as input data provider. In fact, once selected the cloud model object of the analysis, it produces a time-varying map constituted by 20 heat flux images describing the different radiative condition at which the receiver is subjected due to the cloud passage process over the solar field. In particular each of the 20 images represents a different position of the cloud. The cloud passes directly from a position to the other and, as a consequence, on the receiver is verified the instantaneous change from a heat flux image to the next one.

The elapsed time between two subsequent thermal image, i.e. the elapsed time between two cloud positions considered in the discretisation is the first thing to define. In this regard, it is considered that the radiation input will be the same for a certain amount of time (according to the wind speed) and then will suddenly change to the next values. The elapsed time depends on both the cloud velocity and the field portion that it has to cross in order to pass from a position to the following one. By assumption the former is considered to be equal to the wind velocity, value introduced manually by the user or kept as default to 5 m/s as average wind speed in Andalusia.

The latter represents the solar field discretisation unit and is computed dividing the field radius by the number of cloud positions available:

$$dx_{field} = \frac{R_{field}}{nr^{\circ}_{images}} \tag{2.33}$$

As a consequence, the elapsed time (from now on defined as *changing-time*) is computed as follows.

$$\Delta t_{change} = \frac{dx_{field}}{v_{wind}} \tag{2.34}$$

At the end, the *time-frame*, i.e. the overall period of time in which both the radiation map and the receiver surface are affected by the cloud passage, is defined as the sum of the elapsed time for each thermal image.

At this point some clarifications need to be done. Firstly, the elapsed time is always rounded to the closest whole number allowing the program to work at 1 second *time step*. Two are the reasons of this selection: a smaller time division would lead to computational time too high for Matlab; on the other hand, a greater time division would not let the user appreciate the receiver dynamic performance. Secondly the wind speed, and therefore the cloud velocity, is supposed to be constant during all the transitory event, i.e. clouds do not accelerate or decelerate in the time-frame.

In order to give an idea, with the default wind velocity the cloud changes its position every 14 seconds and the overall passage time-frame is of 281 seconds (roughly 5 minutes).

2.4.2 Preliminary thermal analysis

In a transient analysis both capacitive and time changing terms have to be taken into account in the thermal equations describing the phenomena. In this regard, as already evidenced in section 2.3 the system has to be solved according to the thermal equilibrium in between heat thermal fluid and pipe wall for the imposed radiation conditions.

By the way, a preliminary analysis focused on the heat capacity of the two thermal element has to be developed to underline possible differences in their order of magnitude and, if permitted, to simplify the problem considered.

For these purposes a single pipe control volume has been considered and heat capacity has been computed as follows.

Pipe heat capacity

The mass of an empty pipe is calculated according to the geometric parameters and material properties introduced in 2.2.

$$M_{pipe} = \rho_{pipe} \cdot V_{pipe} = \rho_{pipe} \cdot \frac{\pi}{4} \cdot ({d_{ext}}^2 - {d_{int}}^2) \cdot L_{pipe} \tag{2.35}$$

Considering the material specific heat capacity is then possible to obtain the overall pipe heat capacity:

$$C_{pipe} = Cp_{pipe} \cdot M_{pipe} = 5.15 \cdot 10^4 \ \frac{J}{K} \tag{2.36}$$

HTF heat capacity

HTF heat capacity is considered for the same pipe control volume. As a consequence, the considered HTF volume is the space available for the fluid inside the pipe.

$$M_{fluid} = \rho_{fluid} \cdot V_{fluid} = \rho_{fluid} \cdot \frac{\pi}{4} \cdot {d_{int}}^2 \cdot L_{pipe} \tag{2.37}$$

Considering the material specific heat capacity is then possible to obtain the overall pipe heat capacity:

$$C_{fluid} = Cp_{fluid} \cdot M_{fluid} = 6.31 \cdot 10^4 \ \frac{J}{K} \tag{2.38}$$

Heat capacity comparison

Once obtained the two heat capacities for the same control volume, data have been compared.

$$\frac{C_{fluid}}{C_{pipe}} = 1.2 \tag{2.39}$$

As resulted in 2.39, heat capacities are in the same order of magnitude but the value for HTF results 20% higher with respect to the pipe one. In a practical sense, this means that HTF is characterised by a more important capacitive term and requires a greater amount of energy in order to increase its temperature of 1°C.

From the opposite perspective, HTF is able to provide an higher amount of energy due to its thermal storage capacity at same temperature decrease.

In this regard, a further assumption is hereby introduced. In fact, from a theoretical perspective, the heat capacity analysis allows to focus the transient model on the HTF rather than the pipe wall.

As a consequence, the transient model is used to describe the HTF thermal behaviour while, on the other hand, pipe wall characteristics respect quasi-steady state rules and therefore are obtained by stationary equations. This is an important and strong assumption that for sure will affect the results accuracy but, on the other hand, it allows both to ease the problem complexity and reduce the computational time required by *Matlab* to provide the solution.

2.4.3 HTF transient modelling

As demonstrated in the preliminary analysis, HTF modelling is crucial to determine the power plant performances in the considered perturbation time-frame.

Several simulation models can be found in literature, but according to the previous assumption it has been selected to proceed through the resolution of the energy conservation equation for the fluid (f-subscript in the following equations) imposing the thermal equilibrium with respect to the pipe wall. As a consequence, the problem for each of the annular discretisation units of the pipe is formulated as follows:

$$\frac{\partial(\rho_f \cdot Cp_f \cdot T_f)}{\partial t} + \frac{\partial}{\partial x}(\rho_f \cdot Cp_f \cdot \overrightarrow{v} \cdot T_f) = \frac{\partial}{\partial x}\left(k_f \cdot \frac{\partial T_f}{\partial x}\right) + h_{conv} \cdot (\overline{T_{wall}} - T_f) \quad (2.40)$$

$$T_{wall_i} = T_f + \frac{q_{eff_i}}{R_{tot}} \quad (2.41)$$

Different mathematical approaches have been adopted in literature to integrate these equations: finite differences method and complex models using CFD tools or *TRNSYS* environment.

On the other hand, the thermodynamic model developed in this work is written in *Matlab*, maintaining the same choice as for the stationary model and exploiting the capabilities of this software to solve partial differential equations in both time and space.

In this regard, further assumptions have to be made to properly develop the model:

- One-dimensional model. HTF temperature is assumed to vary along the pipe axis only. For each height (coordinate along the axis), there are no radial nor tangential temperature gradients.

- Viscous dissipation is not taken into account in the energy balance for it is several orders of magnitude smaller than the other terms ([45]).

- One pipe for each panel is analysed. The same assumption of the stationary model is maintained in order to simplify the problem and reduce the number of equations. Furthermore the HTF proceeding path is modelled as if it was through a single longer tube rather than the real nine ones. In this regard, the HTF path is described according to the *jj*-index as introduced in 2.3.6. (*jj*-index direction is reported as the x one in equation 2.40)

- Heat transfer by convection is considered to be exchanged to the HTF from the average pipe wall temperature of the annulus, i.e. the mean value of the eight flux unit of the annulus:

$$\overline{T_{wall}} = \sum_{i=1}^{8} \frac{T_{wall_i}}{8} \tag{2.42}$$

  In this way either the number of the equation and the computational time of the code are further reduced and *Matlab* solution results more stable.

Matlab PDEPE function is the selected tool for the mathematical solution of the introduced problem. In fact, it is optimized to the solution of initial boundary value problems for parabolic-elliptic partial differential equations (PDEs) in one spatial dimension x and time t. It is to note that parabolic PDEs are used to describe a wide range of physical phenomena, including heat transfer.

In as far as Matlab is concerned, these equations must be expressed as follows for a cylindrical problem ([53]):

$$c\left(x,t,u,\frac{\partial u}{\partial x}\right)\frac{\partial u}{\partial t} = x^{-1}\cdot\frac{\partial}{\partial x}\left(x\cdot f\left(x,t,u,\frac{\partial u}{\partial x}\right)\right) + s\left(x,t,u,\frac{\partial u}{\partial x}\right) \tag{2.43}$$

Equation 2.40 must be rearranged to adopt this parabolic form above so that it can be managed by the *PDEPE* solver. Considering the same assumption about one dimensional problem, the resulting expression is as follows:

$$\frac{\rho_f\cdot Cp_f}{k_f}\cdot\frac{\partial T_f}{\partial t} = \frac{1}{x}\cdot\frac{\partial}{\partial x}\left(x\cdot\frac{\partial T}{\partial x}\right) - \frac{1}{x}\cdot\frac{\partial T_f}{\partial x} - \frac{\rho_f\cdot Cp_f\cdot\overrightarrow{v}}{k_f}\cdot\frac{\partial T}{\partial x} + \frac{4\cdot h_{conv}}{k_f\cdot d_{int}}\cdot(\overline{T_{wall}} - T_f) \tag{2.44}$$

All the fluid properties, such as density, specific heat or thermal conductivity, are evaluated for HTF at each point of the mesh as function of the temperature for each time step.

As already introduced, HTF proceeding through the receiver is subdivided in 252 annulus along the lengthwise direction for both western and eastern path. For each of the mentioned discretisation units *Matlab* imposed the above equation and autonomously solves the equations system by establish the boundary conditions of a section according to the previous and following one.

Initial temperature values are taken from the previous time step, whilst boundary conditions are specified for the inlet and outlet receiver section. The boundary

conditions for the charging process are as follows:

$$\underline{x = 0 \;\; (jj = 1)} \quad T_f = T_{inlet} = 290°C; \quad \frac{\partial T_f}{\partial x} = 0 \tag{2.45}$$

$$\underline{x = L \;\; (jj = 252)} \quad \frac{\partial T_f}{\partial x} = 0 \tag{2.46}$$

2.4.4 Operating principle of the algorithm

Once the HTF thermal modelling has been proposed, the overall framework of the transient model is hereby explained underlining the methodology through witch *Matlab* solves the system for every time step.

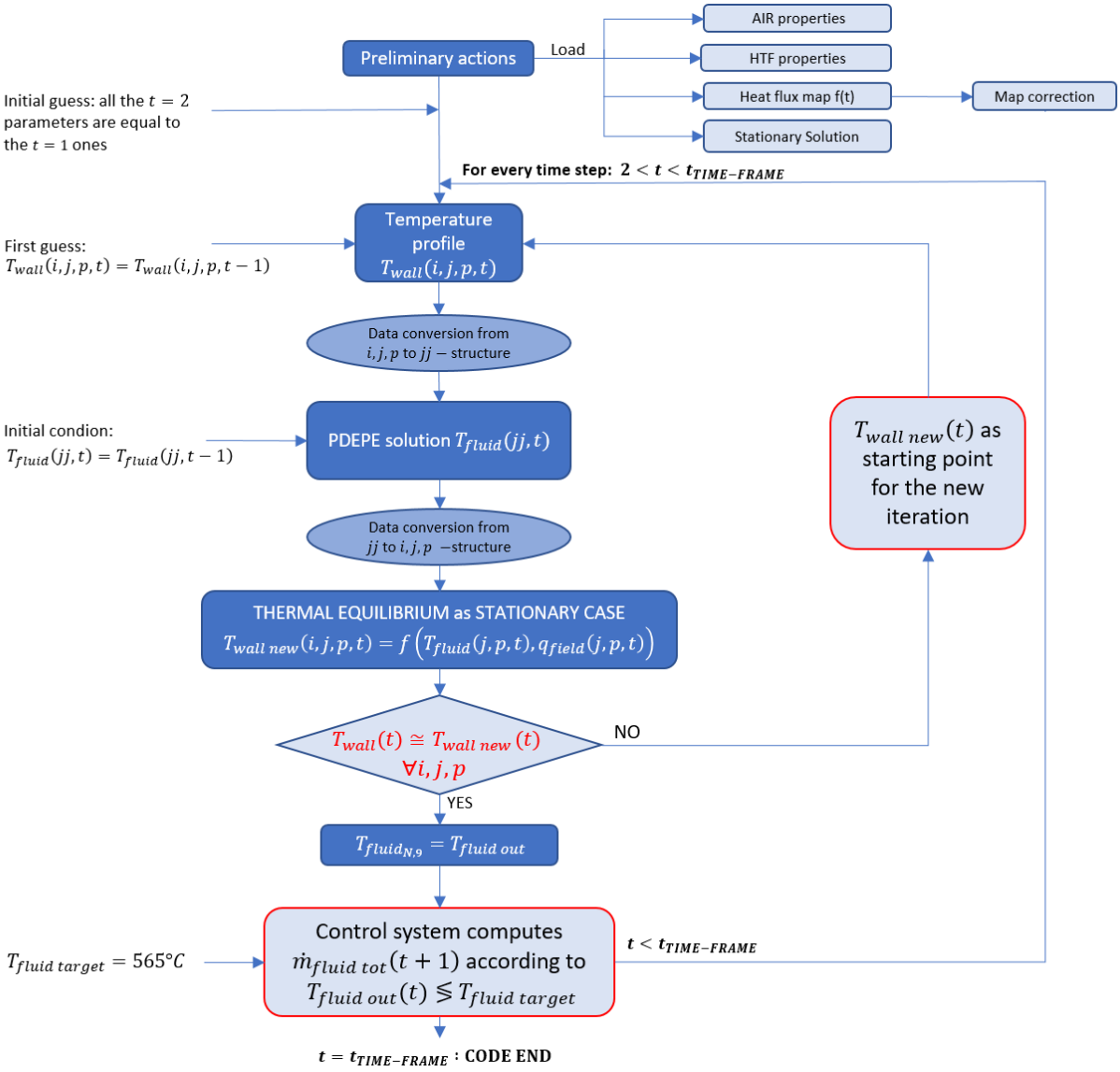

Figure 2.27: Matlab logic operating principle of the transient problem.

1. First of all, the required input data have to be loaded. As in the case of the stationary model, the database for both air and molten salts properties is obtained for a wide range of temperature and pressure using *EES* as source. From these values the tool autonomously computes fluid properties by interpolation. After that Crespi-Zani's *Solar Tool 5* is launched and the user is free to select the proper aiming strategy, day and hour of the analysis and cloud type for the transient analysis. Finally the stationary problem of the first thermal image is solved as done in section 2.3 and the results are loaded for the further transient computation.

2. Considering the stationary problem as the first time-step of the analysis ($t = 1$) the code enters in a *for*-cycle computing the solution for each time-step included in the time-frame considered for the transient problem ($2 < t < t_{TIME\ FRAME}$).

3. The code proceeds setting as first guess for all the parameters their value at the previous time-step ($t - 1$) in order to reduce the number of unknown. After that, it enters in the iterative process firstly for the western path case and then for the eastern one. The flow-chart reported in figure 2.27 is valid for both of them.

4. Starting from the first guess of pipe wall temperature profile and the HTF temperatures of the previous time-step, *Matlab PDEPE* function provides the molten fluid temperature evolution during the time-step ($T_{fluid}(t)$). A particularity has to be underlined: as already said *PDEPE* function works using the lengthwise direction described by *jj-index* but the normal system and the thermal equilibrium continues to be based on the traditional discretisation according to *i,j,p-indexes*. As a consequence, either before and after the use of *PDEPE* function all the values have to be traduced from a framework to the other in order to respect the different correlations.

5. Using the obtained HTF temperature profile, the same model introduced for the stationary case is applied in order to solve the thermal equilibrium among molten salts and pipe wall surfaces computing the latter as function of the HTF temperatures profile, the radiation map ($q_{field}(j, p, t)$) and all the thermal losses. This step is based on the theoretical assumptions made in 2.4.2. In fact, considering a lower heat capacity for the pipe wall it is assumed that its temperature profile will change in a faster way with respect to the HTF one. From a numerical perspective, this temperature change happens in a negligible time and then pipe wall temperatures remain constant for the whole time-step affecting the HTF thermal response. In this way, it is possible to use *PDEPE* computing the molten salts evolution from the imposed pipe wall boundary

conditions. By the way, thermal equilibrium conditions have to be satisfied for each time step. As a consequence, the iteration on the pipe wall temperatures is set in order to find the profile that assures thermal equilibrium conditions with the molten salts at the end of the considered time-step.

6. The new pipe wall temperature profile ($T_{wall\ new}(i,j,p,t)$) is compared with the first guess ($T_{wall}(i,j,p,t)$) and the error between them is evaluated for each flux unit: if the inaccuracy is greater than the tolerance accepted the code comes back to point 4 through a *while* function and uses $T_{wall\ new}$ as new starting value. This iterations assures the temperature equilibrium linking the HTF transient evolution and the quasi-steady state behaviour of the pipe wall.

7. Once the thermal model is solved for the considered time step t, the HTF outlet temperature is compared with respect to the target one. In order to correct the mass flow rate deliverable with respect to the radiation conditions a control system has to be introduced. The main idea is that according to the available solar radiation the receiver has to guarantee the HTF target temperature at the outlet section modifying the molten salts mass flow rate. As a consequence, the control system corrects the the HTF mass flow rate for the next time-step $(t+1)$ according to the obtained HTF outlet temperature of the present one (t).

8. Points from 3 to 6 are repeated for each time-step solving the entire time-frame considered and providing the system performances for the selected cloud passage.

2.4.5 Solver stability

With the modelled tool transient problems can be solved. By the way, the system results to be extremely unstable and, as a consequence, the condition on the outlet target temperature is not satisfied for various attempts.

After investigations the problem is identified in the control system. In the original configuration, a simple proportional control system was in fact set as modelling first attempt according to the hereunder correlation:

$$\dot{m}_{fluid\ tot}(t+1) = \dot{m}_{fluid\ tot}(t) \cdot \left(\frac{T_{fluid\ out}}{T_{fluid\ target}} - 1 \right) \cdot F \tag{2.47}$$

where F represents a weight factor which value can be imposed by default according to the importance of computed temperature error in the system controlling: higher the F factor, higher the correcting action on the mass flow rate at same temperatures error.

In this regard, the proposed model was not able to properly control the system evolution and, as a consequence, the results were unacceptable leading to HTF temperatures above the upper degradation limit. For this reason, a more complex PID (Proportional-Integral-Derivative) control system has been developed to improve the tool accuracy and, as a consequence, the overall solver stability.

Being the control system a fundamental element in the transient model, an entire chapter has been dedicated to its analysis reporting the obtained transient results in a later stage.

Chapter 3

Control system and analysis

In this chapter the control system of the solar receiver is developed and analysed. In particular, feed forward and feed back control theories are firstly modelled and then compared in order to select the most suitable strategy for the transient problem solution.

At a later stage, the chosen model is used to analyse in details various clouds passages underlining system performances and possible critical problems.

3.1 Control system theoretical basis

As mentioned in the chapter introduction, two methodology are selected: feed forward and feed back control. In this regard, the aim of this section is to provide the theoretical basis to the control system modelling phase.

A control system is a fundamental element for the receiver: it is able to properly guarantee the HTF target conditions at the outlet section and it ensures limits compliance avoiding dangerous and problematic situations.

In this regard, HTF mass flow rate is the main parameter through which the control system can act. In fact, at constant incident radiation higher the mass flow rate sent to the receiver pipes, lower the HTF temperature obtained at the outlet section; on the other hand, reduce the mass flow rate provokes a general temperatures increase. The relation between the target outlet temperature and the mass flow regulation factor has to be defined according to the error verified for each time step. The latter is computed as follows.

$$error(t) = \frac{T_{fluid\ out}(t)}{T_{fluid\ target}} - 1 \tag{3.1}$$

$$\Delta \dot{m}_{fluid\ tot} = f\left(error(t)\right) \tag{3.2}$$

where f is the characteristic function that define the "weigth"of the error with respect to the imposed target condition. According to the selected control model f-function assumes different structure.

3.1.1 Feed back control theory

From a general perspective, a feed back control is a particular regulating method in which outputs of a system are routed back as inputs as part of a chain of cause-and-effect that forms a circuit or loop. The system can then be said to feed back into itself.

Various type of feed back regulations are available in literature, PID controller has been selected among all for the present model ([6]).

The PID controller was first placed on the market in 1939 and has remained the most widely used controller in process control until today. PID is the acronym for "proportional, integral and derivative" and identifies a controller that includes element able to provide these three function in the system control task:

- *P-element*: proportional to the error at the instant t, which is the "present" error;
- *I-element*: proportional to the integral of the error up to the instant t, which can be interpreted as the accumulation of the "past" error;
- *D-element*: proportional to the derivatice of th error at the instant t, which can be interpreted as the prediction of the "future"error.

A PID controller continuously calculates an error value $e(t)$ as the difference between a desired set point and a measured process variable and applies a correction based on proportional, integral, and derivative terms.

The controller attempts to minimize the error over time by adjustment of a control variable u(t) to a new value determined by a weighted sum of the PID terms:

$$u(t) = K_P \cdot e(t) + K_I \cdot \int_0^t e(\tau)d\tau + K_D \cdot \frac{d\, e(t)}{dt} \tag{3.3}$$

where K_P, K_I, and K_D, all non-negative, denote the coefficients for the proportional, integral, and derivative terms and each of them behaves like a "weight" in the sum providing more importance to the representative term in the overall value.

Particular attention has to be focused in the PID coefficients because either excessive and too low parameter can badly affect the system response. For instance, high proportional gain K_P results in a large change in the output for a given change in the error. If the proportional gain is too high, the system can become unstable. In

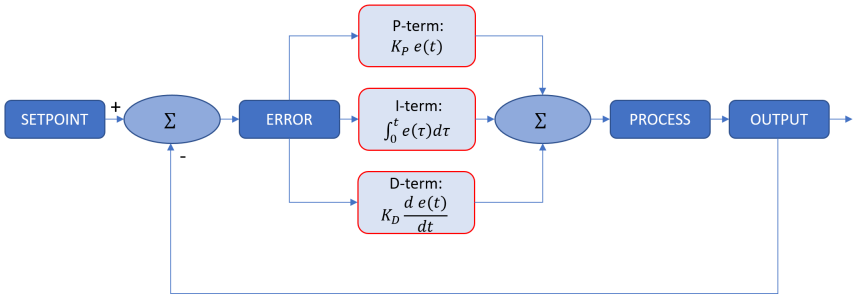

Figure 3.1: PID control system logic principle.

contrast, a small gain produces a small output response even in case of a large input error, characterising a less responsive and less sensitive controller. If the proportional gain is too low, the control action may be too small when responding to system disturbances.

As a consequence, the main issue is to find by attempts the specific values of K_P, K_I, K_D through which properly regulate the model response for any cloud passage case.

3.1.2 Feed forward control theory

Opposite with respect to feed back theory, the feed forward control system is a controller method that regulates the system in a predefined way according to a measured parameter and a corrective map (*lookup table*) provided in advance.

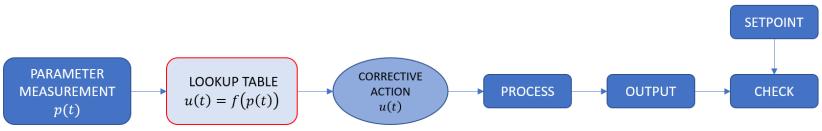

Figure 3.2: Feed forward control system logic principle.

In particular, as shown in figure 3.2, starting from a measured parameter the method is able to provide a corrective action $u(t)$ according to a set of predefined values available in a lookup table. Once imposed the corrective action to the system it is possible to check the obtained result with respect to the target one (set point). The resulting method is very simple and requires a lower computational load with respect to the feed back one. By the way it cannot regulate the system in the case of a scenario not described in the predefined lookup table library.

3.2 Feed forward control model

In this section the control system based on the feed forward method is firstly modelled and then linked to the developed transient model (section 2.4) in order to compute the receiver performances in case of transient phenomena.

3.2.1 Operating principle

From the present problem perspective, the control system is constituted by a pyranometer and a electronic circuit board linked to the HTF pump.

The pyranometer measures the solar radiation that reaches the receiver surface for every time-step and provides this information to the electronic circuit board. The latter takes as input the pyranometer informations and computes the amount of HTF mass flow that the pump has to send to the receiver circuits by interpolation of the data available in the lookup table. In this way the molten salts mass flow rate is proportional to the radiation value for each cloud passage time-step.

The first step for the control system development is the creation of the lookup table. In this regard, a multitude of radiation maps have been imposed on the receiver and for each of them the HTF mass flow guaranteed by the receiver at stationary conditions has been computed and saved in the table. As example, an extract of the lookup table for the western path is shown in table 3.1 for the 21^{st} March 12 am condition.

Mean radiation $[kW/m^2]$	HTF mass flow rate $[kg/s]$
240.2	95.8
245.8	97.6
275.2	113.6
302.6	125.8
331.1	138.9
399.4	168.9
441.6	187.4
478.7	207.0

Table 3.1: Lookup table extract for the western path, 21^{st} March 12 am.

As a consequence, once measured the average incident radiation the code can autonomously compute the molten salts flow rate and proceed to the transient solution for every time step.

Furthermore, in the developed model the traditional feed forward calculation is enriched with a component proportional to the error at the previous time step. In

this way it is possible to create a more sensitive controller able to respond to the thermal oscillations of the system. In this regard, K is the *under-relaxation factor* with respect to the error $e(t-1)$.

The control logic of the whole model is explained in figure 3.3. Note that "transient thermal model" is referred to the model introduced in 2.4.4.

$$\dot{m}_{fluid\ tot}(t) = \dot{m}_{lookup\ table} + K \cdot e(t-1) \tag{3.4}$$

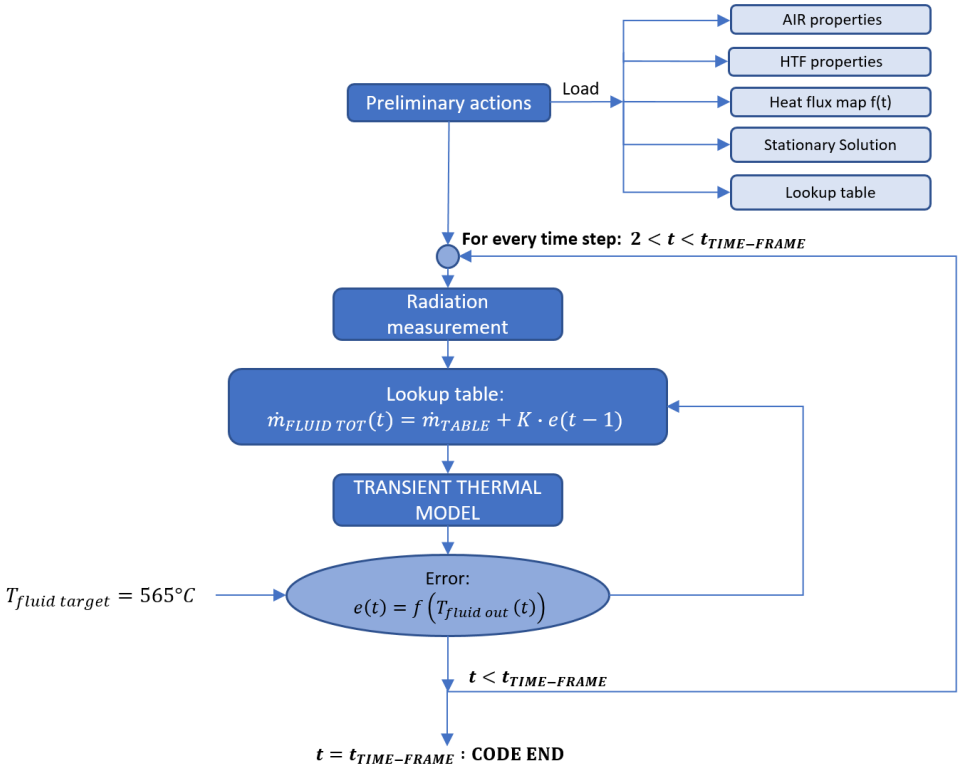

Figure 3.3: Transient model with feed forward operating principle.

As shown, for each time step t the code measures the average incoming radiation and computes the correspondent value of the HTF mass flow rate through the lookup table. With the value set by the control system the transient thermal model is launched, obtaining as solutions both the molten salts and the pipe wall temperatures profiles. Error between the target and the real HTF outlet temperature is computed by the controller and the result is saved for the next time-step correction.

3.2.2 Results

The developed model is finally applied to the transient problem solution. As further system optimisation, a multitude of K values have been tested in order to find the most suitable ones. The results hereunder reported are obtained using the best K coefficients found for the cases of high and low error influence:

- *High* K means that a greater importance is given to the error computed at the previous time-step and, as a consequence, the $\dot{m}_{fluid\,tot}$ value provided by the lookup table changes in a significant way according to equation 3.4. It is a more pessimistic perspective in which lookup table values are considered less reliable and the system has an higher degree of freedom regulating by itself the HTF mass flow rate according to the computed error.

- *Low* K means that a lower importance is given to the error computed at the previous time-step and, as a consequence, the $\dot{m}_{fluid\,tot}$ value results to be almost equal to the one provided by the lookup table. It is a more optimist perspective in which lookup table values are considered with a higher level of confidence.

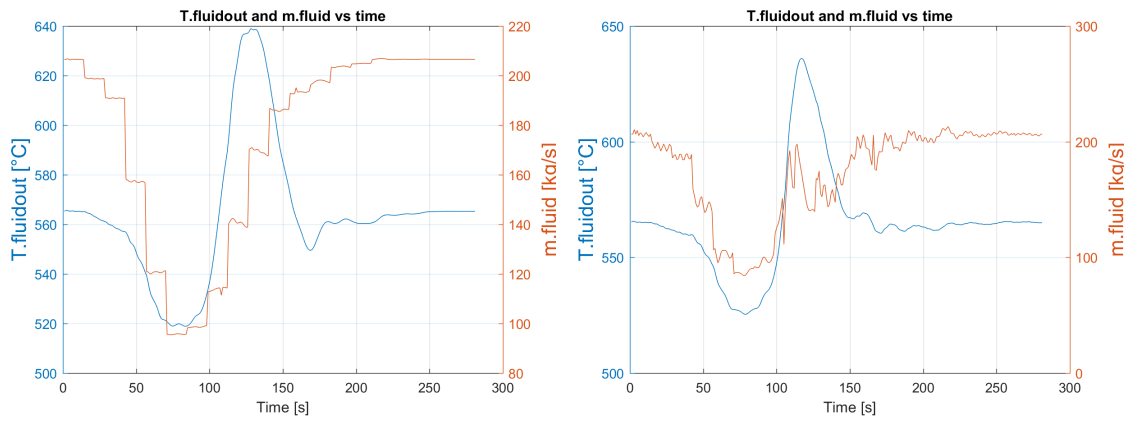

Figure 3.4: "Total shadow as PS10" cloud transient solution. Feed forward: *a*) low K control system. and *b*) high K control system.

The two proposed solutions for the "total shadow as PS10" cloud passage result very similar even if different K values have been used. The main difference is represented by the produced HTF mass flow curve (depicted in orange in both figures): for the high K case a more oscillating trend is detected, on the other hand the curve follows a steps behaviour in the case of low K. Both curves show a minimum point either in the mass flow rate and in the outlet temperature due to the minimum values of the radiation map determined by the maximum shadow condition imposed by the

considered cloud.

From a fluid outlet temperature perspective, high K case succeeds in a better control of the maximum value but neither of the two proposed solution appears completely in compliance with respect to the upper degradation limit. In fact, once the cloud starts exiting the solar field and the radiation raises, the control systems are not able to properly control the maximum fluid temperatures by increasing with the same rate the HTF mass flow sent to the receiver. As a consequence, possible degradations problem can occur due to excessive fluid temperatures. In this regard, solar field unshadowing results the most critical thermal condition.

In order to provide a more suitable solution the feed back method has been analysed.

3.3 Feed back control model

In this section the control system based on the feed back method is firstly modelled and then linked to the developed transient model (section 2.4) in order to solve the receiver performances problem.

3.3.1 Operating principle

From the present problem perspective, the control system is constituted by a thermometer device (a thermocouple for instance) and an electronic circuit board linked to the HTF pump.

The thermocouple measures the HTF temperature at the outlet section for every time-step and provides this information to the electronic circuit board. The latter takes as input the thermometer informations and computes the amount of HTF mass flow that the pump has to send to the receiver circuits according to error between the measured value and the target ones. In the evaluation of the the new mass flow rate value each of the PD components is taken into account together with the previous time-step error $[e(t-1)]$:

$$\dot{m}_{fluid\,tot}(t) = \dot{m}_{fluid\,tot}(t-1) \cdot \left[K_P \cdot e(t-1) + K_D \cdot \frac{d\, e(t-1)}{dt} \right] \tag{3.5}$$

Firstly the developed control system was constituted by all the three PID terms but in a later stage it has been selected to adopt only PD components due to the instabilities introduced in the system by the integral element.

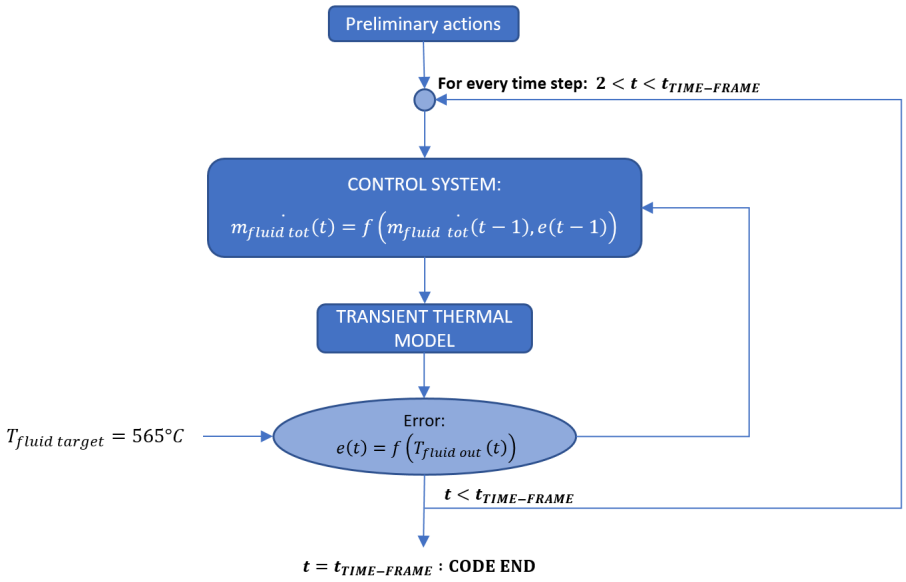

Figure 3.5: Transient model with feed back operating principle.

Using equation 3.5 as regulating function, the overall framework of the transient model is hereby explained underlining the methodology through witch *Matlab* solves the system for every time step.

For every time-step $2 < t < t_{time-frame}$, the control system computes the HTF mass flow rate according to the temperature error computed at the previous time-step and corrected by the use of the PD coefficients. With the molten salts mass flow the transient problem is solved as introduced in section 2.4. Error between target and obtained HTF outlet temperatures is evaluated and saved for the regulation of the next time-step.

3.3.2 Results

The developed model is finally applied to the transient problem solution. As further system optimisation, a multitude of PD coefficients have been tested in order to find the most suitable ones. The results hereunder reported are obtained using the best K coefficients found for the cases of high, low and variable error influence:

- *High under-relaxation factors case.* With a high value selection for K_P and K_D terms the aim is to keep the HTF outlet temperature as close as possible to the target. It represents the safest case from a degradation perspective because excessive temperatures conditions are avoided. On the other hand,

high coefficients stress most the pump working conditions by imposing brusque changes in the molten salts mass flow rate.

- *Low under-relaxation factors case.* From a more optimistic perspective, it is assumed that low K_P and K_D values are enough to properly regulate the system.

- *Variable under-relaxation factors case.* It is the most sophisticated control system proposed: variable coefficients are imposed in the governing rule according to the measured HTF temperature values at the outlet section. Up to the moment in which the latter is kept inside a safety temperature limit, low coefficient are used to regulate the system in a soft way avoiding stress conditions. On the other hand, when this limit is exceeded the control system reacts using higher values for the PD coefficients in order to re-establish safety conditions from a fluid degradation perspective.

$$T_{upper\ limit} = 580°C \tag{3.6}$$

$$\underline{T_{fluid\ out} < T_{upper\ limit}} \quad Low\ K_P\ and\ K_D\ values \tag{3.7}$$

$$\underline{T_{fluid\ out} > T_{upper\ limit}} \quad High\ K_P\ and\ K_D\ values \tag{3.8}$$

Two further conditions are then set. A lower temperature limit is introduced in order to avoid fluid solidification problems in case of long radiation lack. In this regard, if the HTF temperature is lower than the cold tank one (290°C) in any section, the receiver is emptied and an error message is displayed by the compiler.

On the other hand, a minimum condition is set at the outlet section of the receiver: if the HTF temperature is higher then 500°C the fluid is allowed to enter the hot tank otherwise it is sent back to the cold tank. This condition is applied in order to safeguard the thermal conditions of the heat storage system; lower temperature will cool the tank causing off-design conditions of the HTF-steam heat exchanger.

The simulation results for the three cases are hereunder reported and analysed.

From a graphical analysis it is distinguished between overdamped and underdumped behaviours. HTF outlet temperature for the *variable K case* presents sensible fluctuations that the control system did not successively dump and, for that reason, it is defined underdumped. Similar but slightly lower trend is shown by the *high K case*. On the other hand, the *low K case* is defined an overdamped system due to

the absence of fluctuations.

From a HTF temperature perspective, only *variable K case* is compliant with respect to the degradation limit (600 °C) while the other ones exceed this value and provoke an irreversible properties decline in the molten salts. Furthermore, *variable K case* guarantees the higher temperature value in case of radiation absence, meaning that it is the system through which the hot tank conditions can be better maintained avoiding cooling processes of the stored fluid.

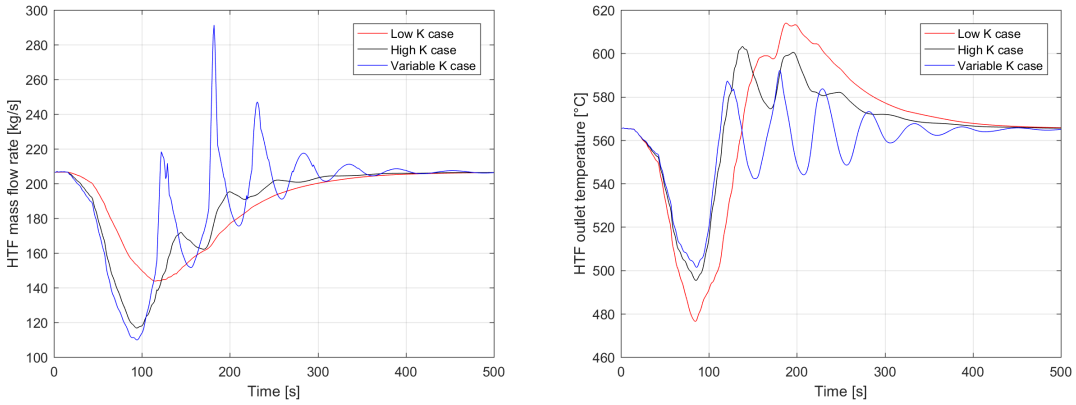

Figure 3.6: "Total shadow as PS10" cloud transient solution. Feed back cases comparison: *a*) HTF mass flow and *b*) HTF outlet temperature.

On the other hand, from a pump perspective, the mass flow rate conditions imposed by the *variable K case* result to be the worst ones due to the high peaks in correspondence to the moments in which an higher mass flow rate was required by the system to reduce the maximum fluid temperature. In this regard, the solar field unshadowing process, i.e when the cloud leaves the power plant, is the most problematic condition: due to the previous low radiation, a lower mass flow is sent to the receiver, by the way when the clouds passes radiation raises to normal values in few seconds and, as a consequence, the fluid is warmed up to excessive temperatures. In this regard, a mass flow peak represents a stressful condition for the pump system but it is the only way to keep temperatures inside a safety conditions band.

Figures 3.6 *a*) and *b*) demonstrate that K values have to be a trade off between the required fluid outlet temperature and the system equilibrium. Higher the K, lower the temperature error but higher the system instability. On the other hand, low K means reduced system oscillation but at the same a rough accuracy of the obtained temperatures profiles. In this regard, *variable K case* is the best solution due to the possibility of use variable "weight" parameters coupling the best point of the two behaviours.

3.4 Controller comparison: back vs forward

In this section the proposed feed back and forward control methods are analysed.

In this regard three are the main parameters object of the investigation: HTF mass flow rate produced, molten salts outlet temperature and pipe wall temperature gradient.

From the pipe wall perspective, it is computed the temperatures gradient at which the pipe surfaces are subjected in order to understand the thermal stress conditions and analyse where the worst situations occur. In a first step, the problem is analysed computing for each time-step the maximum temperature gradient in the overall receiver surface according to the following equation applied to each flux unit.

$$\frac{\partial T_{wall_{i,j,p}}}{\partial t} = \frac{T_{wall_{i,j,p}}(\tau) - T_{wall_{i,j,p}}(\tau - 1)}{t(\tau) - t(\tau - 1)} \tag{3.9}$$

Note that by definition the computed value is a "temporal gradient", meaning that for a given flux unit the temperature difference is analysed between two consecutive time-steps. Furthermore, it has to be underlined that these results are strongly influenced by the quasi-steady state assumption for the pipe walls. In fact, not considering the thermal storage term and its damping function in the pipe wall energy equation the temperature gradient will be higher with respect to a complete developed thermal model.

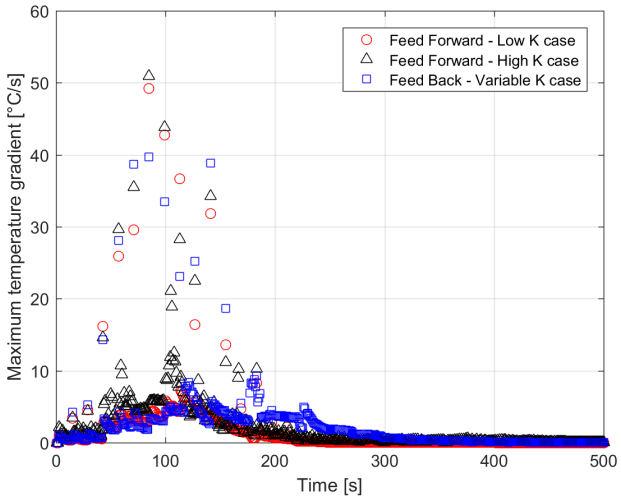

Figure 3.7: "Total shadow as PS10" cloud transient solution. Feed back vs. forward - Max pipe wall temperature gradient.

As shown in 3.7 the models shows a similar trend but the feed back control system guarantees a lower maximum temperature gradient assuring a reduction of

more then 10 °C with respect to the two feed forward cases.

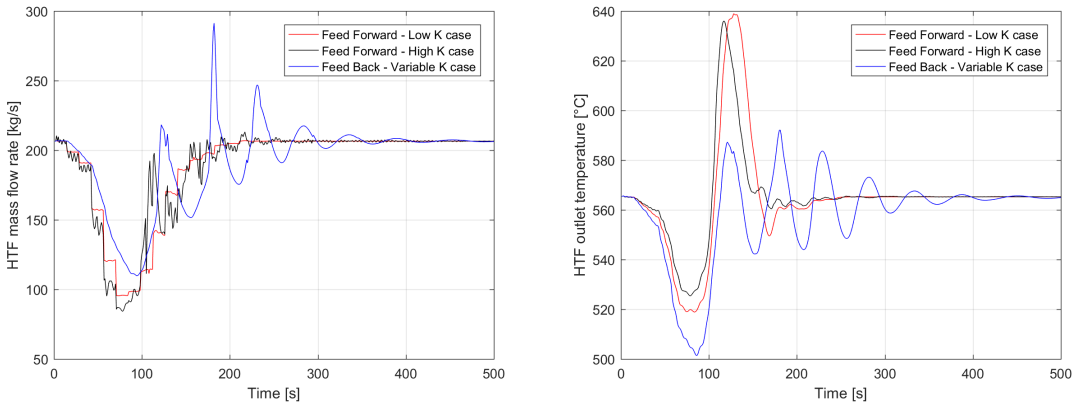

(a) **(b)**

Figure 3.8: "Total shadow as PS10" cloud transient solution. Feed back vs. forward - *a*) HTF mass flow rate, *b*) HTF outlet temperature.

Furthermore, feed back control method is the only one that completely assure temperatures limits compliance. In fact, during the whole transient process it controls HTF temperatures that never exceed the degradation limit of 600°C, preserving molten salts thermal properties. On the other hand, the feed forward cases lead the system to dangerous condition with HTF temperatures close to 640°C.

From a HTF mass flow rate perspective, feed forward cases present similar trend due to both the lookup table imposition and the reduced error importance. On the other hand, feed back case shows a more oscillating trend with peak values in correspondence of the time-steps in which the system needed to control strongly the temperatures raising during the unshadowing phase.

As result of the explained characteristics, feed back with variable K coefficients is demonstrated to be the best control system choice in order to guarantee safety operating conditions. As a consequence, all the following transient results are obtained using this methodology as controller strategy of the system.

3.5 Transient model results

In this section the best developed control methodology is used as regulating system for the solution of transient problems. Firstly the control system has been tested according to radiation step changes, then the code potentialities have been shown for the "total shadow as PS10" cloud case. In a later stage, all the clouds model have been analysed and compared in order to investigate the most critical situation to which a tower receiver can be subjected.

3.5.1 Steps response

In this subsection the developed tool is tested according to step changes in the heat flux map. These tests are useful for the evaluation of both the control system stability and the dynamic response time, validating the controller from the worst cases perspective.

100% - 0% step

Firstly a complete radiation lack has been modelled with the final aim of the evaluation of the receiver thermal inertia. Starting from 21^{st} March 12 am nominal radiation conditions (100%) the overall heat flux map suddenly becomes null in each point (0%) as if a big cloud was completely shadowing the solar field (figure 3.9 *a*)).

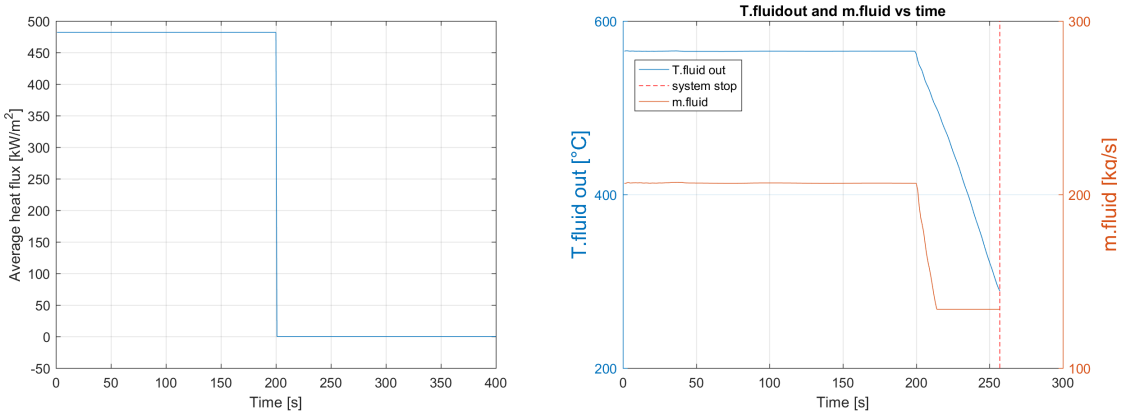

(a) **(b)**

Figure 3.9: Step response 100% - 0%. *a*) Average heat flux, *b*) HTF mass flow rate and temperature at the outlet section.

Since $time = 200\ s$ no more radiation has been provided by the solar field to the receiver external surface. Meanwhile HTF production rate continues but only due to the thermal inertia of the system. By the way, without direct incoming radiation the molten salts outlet temperature rapidly declines and, as a consequence, the control

system operates reducing the mass flow rate sent by the pump to the receiver. In this regard, the production rate decrease proceeds until the fluid outlet temperature is higher than 500°C. With lower outlet temperatures, the HTF has to be sent back to the cold tank avoiding heat storage cooling issues. In this condition, the pump by default keeps constant flow rate. After some attempts, the latter control scheme has been considered by assumption rather than allowing further mass flow rate decrease. From a conservative perspective, keeping a relatively high constant mass flow rate in case of radiation lack means to prepare the system for the following unshadowing phase. In fact, the higher the HTF flowing in the pipes, the higher the heat capacity of the system and, as a consequence, lower the instability introduced in case of increase radiation steps. Back to the analysis, in case of even lower HTF outlet temperatures, the pump complete blockage has been set at the value of 290°C in order to avoid molten salts solidification issues (red dotted line in figure 3.9 *b*)).

As result of the present simulation, a 20 seconds of additional HTF production time at the required conditions has been evidenced since the complete shadowing of the solar field. On the other hand, a further time-lapse of 37 seconds has been computed before the pump complete switch off.

The developed simulation provides proper outputs according to the problem object of the analysis. In particular, it underlines the essential importance of the solar source for the HTF production and, in a preliminary way, it shows the importance of heat storage system from the general power plant perspective: in case of no tanks only one minutes will be enough to completely stop the power block operating conditions.

Results here above appear in line with respect to the output obtained in the receiver time-scale analysis (section 1.14). In fact, the latter reported a system response in the order of 90 s, while present simulation has shown slightly lower value (57 s). In this regard, it has to be considered that the present results are strongly affected by the basic assumption of neglecting the transient phenomena within pipe wall surfaces. In case these terms were be taken into account a higher time would be computed for both the case of production rate and pump blockage and the values would be most probably the same with respect to the time-scale analysis.

According to this simulation, Gemasolar O&M operator has to pay particular attention to the radiation conditions because pump blockage has to be assured after one minute of complete radiation lack in order to avoid dangerous conditions for the power plant.

These results will be used to define the following simulation. In fact, with the final aim of developing a system response to a 100%-0%-100% radiation steps profile,

it will be useless to simulate a complete radiation lack with a more than 50 seconds time-frame because this will cause a complete stop of the system.

100% - 0% - 70% - 100% steps

The original aim of this simulation was to verify the system response to a 100%-0%-100% heat flux steps trend, meaning that starting from the nominal condition a temporary radiation lack occurred and, in a later stage, heat flux map nominal values were re-established.

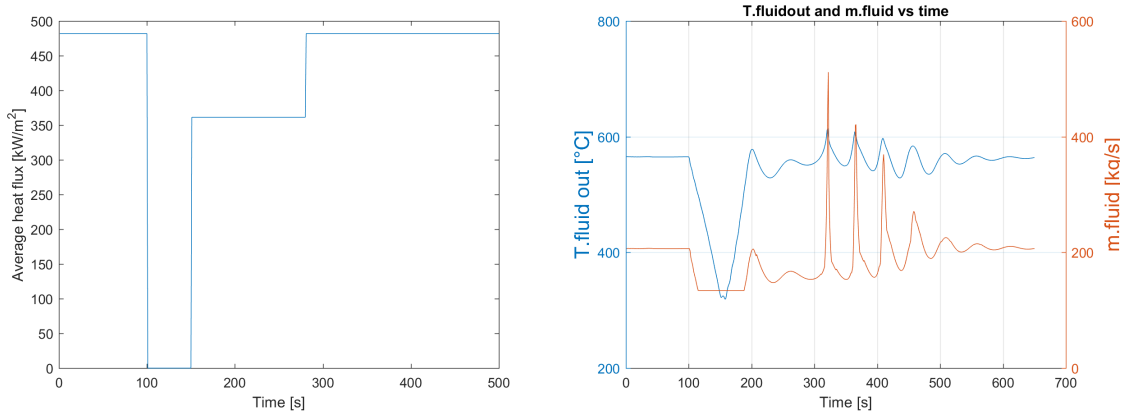

(a) **(b)**

Figure 3.10: Steps response 100% - 0% - 70% - 100%. *a*) Average heat flux, *b*) HTF mass flow rate and temperature at the outlet section.

By the way, after some attempts, these radiation steps resulted too aggressive with respect to the system causing instability and degradation problems especially in the 0% to 100% climb. In fact, once decreased the mass flow rate due to the radiation lack, the sudden 0%-100% radiation step causes an uncontrolled system heating with HTF temperatures that can lead to degradation. In this regard, the control system, optimised for the case of real clouds passages, was not able to completely manage these abrupt and severe conditions changes. As a consequence, in a later stage the 0% to 100% radiation step has been softened using the 0% to 70% scheme. Furthermore, the latter is considered as a more suitable case in order to simulate real ambient conditions verified in the plant daily operations.

In figure 3.10 it is shown how the 50 seconds of radiation lack provoke a sudden decline in the HTF production. This scheme progressively leads to unsatisfactory outlet temperature conditions that cause the HTF come back to the cold tank. Since $time = 150\ s$ the system is brought back to operating conditions through 150 s of 70% heat flux map and further 350 s of nominal radiation. In this regard, 70% to

100% step provokes a greater system instability with HTF temperatures close to the degradation limit. Only high mass flow rate values resulted able to control the temperature increase and damp the the radiation step effects. In any case, the system needs roughly 300 s to complete settle according to the new heat flux conditions.

In conclusion of this preliminary simulation, the control system did not pass the critical 0%-100% step test but it has been confirmed as a good controller for more real radiation conditions as the 100% - 0% - 70% - 100% steps.

100% - 0% - 100% steps

As already explained in the previous simulation, the controller was not able to proper manage the system evolution in case of radiation increase step higher than 70% of the nominal value. With the final aim of optimise the system also in these aggressive conditions, an additional function and a pyranometer have been integrated in the control system structure.

As in the feed forward strategy case (section 3.2.1), the pyranometer measures the receiver incident radiation and provides the measurement to the control system that saves the value in its memory. If the radiation step detected is lower or equal than 70% of the heat flux nominal value the controller regulates the system in default mode using *variable K-values*; on the other hand, for radiation steps higher than 70% the controller sets the nominal HTF mass flow rate, regulating the system according to an overdamped strategy. With this adjustment it has been possible to simulate 100%-0%-100% radiation steps.

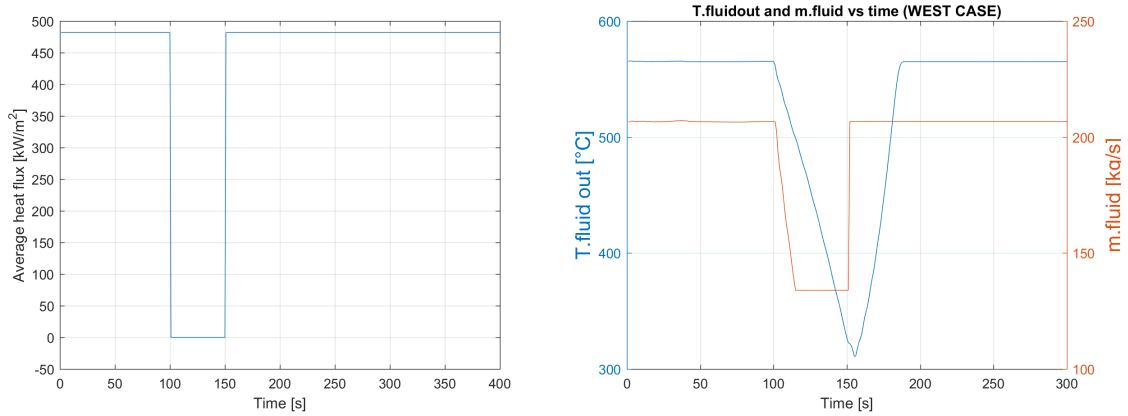

(a) **(b)**

Figure 3.11: Steps response 100% - 0% - 100%. *a*) Average heat flux, *b*) HTF mass flow rate and temperature at the outlet section.

Proceeding with an overdamping control scheme, oscillations and system instability have been avoided in the critical radiation climb step, although the receiver

performances have been sacrificed. In fact, suddenly imposing nominal mass flow in the receiver the outlet HTF temperature conditions cannot be further guaranteed and for approximately 40 s the molten salts have to be sent back to the cold tank because their conditions do not satisfy the minimum temperatures limit. As a consequence, in this elapsed time no production rate is guaranteed by the receiver and the resulting thermal efficiency is null.

By the way, from a conservative perspective these aggressive radiation steps are not often verified and, as a consequence, it is preferable to introduce losses in the system for a while rather than lead the receiver to unsafe operating conditions.

As shown in figure 3.11 degradation limit compliance is assured throughout the whole simulation, with HTF temperature far lower than 600°C. Furthermore in case of only 50 s of complete radiation lack a resulting 75 s of HTF outlet temperature non-compliance has been verified. This trend, as already mentioned, is due to the overdamped control strategy rather than to the unsufficient thermal inertia of the system.

In conclusion, the control system has been optimised with a further regulating function useful in the regulation of more aggressive conditions. In this regard, the controller has been successfully tested and could be used for the specific clouds passage solutions.

3.5.2 Total shadow as PS10 analysis

In addition to the outlet conditions regarding both HTF temperature and mass flow rate with the present model it is possible to analyse the thermal evolution of the whole receiver in the entire time-frame.

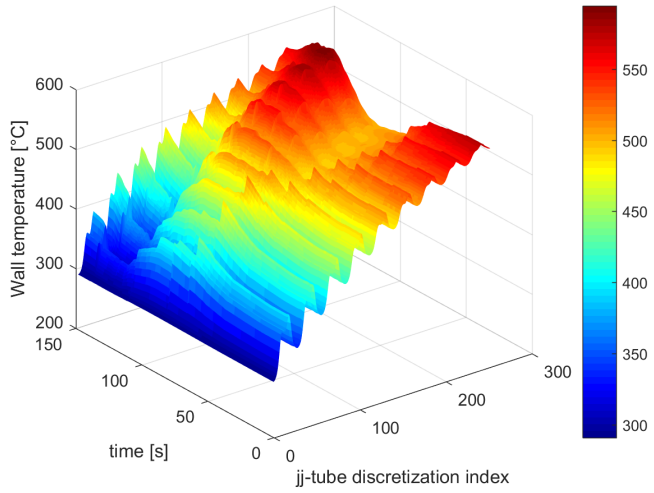

Figure 3.12: "Total shadow as PS10" cloud transient solution. Pipe wall temperatures.

The pipe wall thermal evolution with respect to both time and space is reported in figure 3.12. In this regard, due to the discretisation complexity it has been selected to visualize the results according to the *jj-index* following the fluid path through the various panels. As a consequence, the temperature values are the average ones with respect to each annular section.

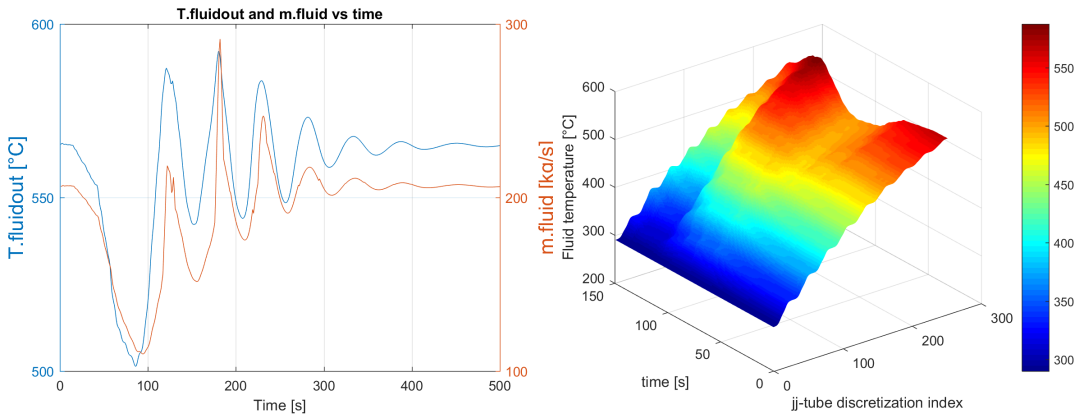

(a) **(b)**

Figure 3.13: "Total shadow as PS10" cloud transient solution. *a*) HTF mass flow rate and temperature at the outlet section, *b*) HTF temperatures vs space and time. Note that 3D charts are reproduced only up to 150 seconds in order to not overload the drawings.

A visible hollow can be evidenced for the around of 100 seconds. In correspondence to the lack of radiation the system is in fact strongly affected by thermal losses, causing a general temperatures decrease. In the following unshadowing phase the pipe wall temperatures present maximum values due to the combined effect of low mass flow rate in the pipes and high values of the incident radiation.

A similar representation is provided for the HTF temperatures profile in figure 3.13. Due to a proper controller action, degradation limit is respected and the system is able to overcome the cloud passage maintaining the HTF production rate with a suitable temperatures profile.

From a temperature gradient perspective, the evolution of the system is analysed in figure 3.14. In this regard, the *jj* and *time-axis* are represented switching their directions in order to better visualize the results in the 3D graph.

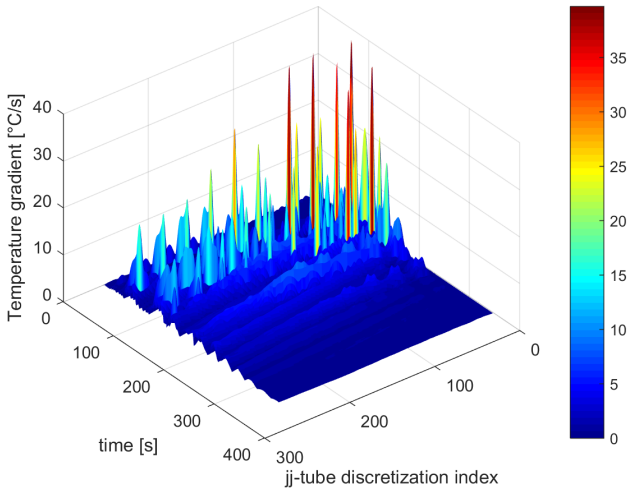

Figure 3.14: "Total shadow as PS10" cloud transient solution. HTF temperatures.

Worst temperature gradient conditions are verified in between the shadowing and unshadowing process ($t \cong 100$ s) for low *jj*-values. This behaviour is explained by the receiver configuration. For low *jj*-values (the firsts receiver panels, as explained in 2.3.6) and nominal conditions the highest heat flux values are verified; on the other hand, the highest radiation rate of change is observed for the same region during transient conditions. As a consequence, this trend produces the highest temperature gradient in the pipe wall surfaces.

3.5.3 Clouds comparison

The already tested tool is used to analyse the available cloud models investigating the system response. In this regard, the *Matlab* code is launched using as input the radiation map for each of the available cloud models. The main results are hereunder graphically shown.

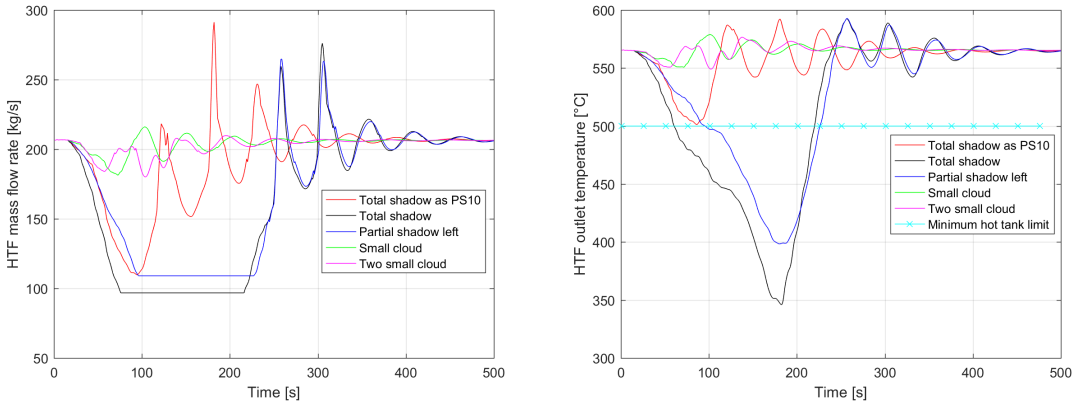

(a) **(b)**

Figure 3.15: Cloud analysis - *a*) HTF mass flow rate, *b*) HTF outlet temperature.

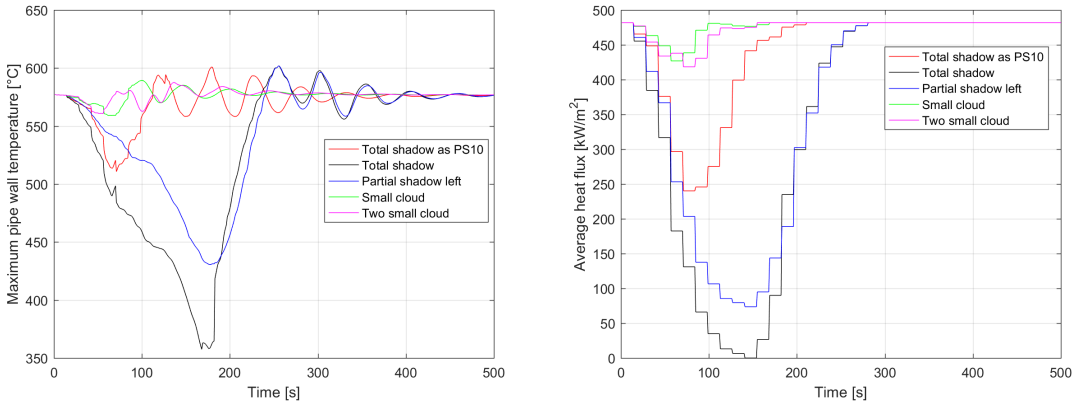

(a) **(b)**

Figure 3.16: Cloud analysis - *a*) pipe wall maximum temperature, *b*) average heat flux on the receiver.

From a thermal perspective, "Total shadow" cloud represents the most critical case. In fact, this cloud passage provokes the highest temperature gradient in the receiver pipe walls and stops the molten salts production. In this regard, the lack of radiation in some time-steps evolves in a complete sun absence. This condition considerably cools the system imposing the HTF to be sent back to the cold tank. As a consequence, the controller stops regulating the system and the mass flow rate

is kept constant (horizontal line in figure 3.15 *a*)). In the unshadowing phase, the system boundary conditions change with a considerable speed and the control system has to properly regulate the mass flow rate in order to avoid degradation issues even if high oscillations are still verified.

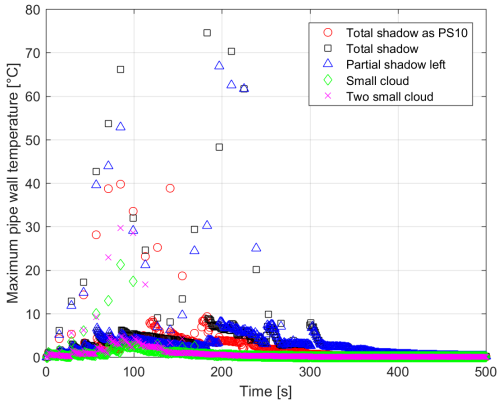

Figure 3.17: Cloud analysis - pipe wall maximum gradient.

On the other hands, "Small cloud" and "Two small clouds" are the cases that less affect the system. Introducing only a partial radiation decrease, their impact is in fact limited by the molten salts heat capacity and, as a consequence, the total amount of HTF produced at the target temperature conditions does not change consistently with respect to the nominal value.

Furthermore it is verified the proportional relation between radiation and temperature gradient: higher the radiation difference between two consecutive time-step higher the temperature gradient imposed on the receiver pipe walls. As confirmation, the higher temperature gradient is observed for both "Total shadow" and "Partial shadow left", two clouds models that introduce a complete shadowing of the solar field with radiation values that from the nominal conditions become zero and then come back to the nominal conditions producing, as a consequence, the highest radiation gradient.

Chapter 4

Analysis of complex scenarios

In this chapter the developed model potential is exploited for the solution of the transient problem regarding more than one consecutive clouds from a complex scenario perspective. In this regard, the attention is focused on the overall plant performance, analysing how the whole system is affected by the transient phenomena.

At this level, the equilibrium in between the amount of molten salts produced by the receiver and required by the power block working in nominal condition is fundamental. In this regard, the storage system acts as a damper with respect to the production rate oscillations caused by the solar source variability. By the way, it has to be proved that hot tank was correctly designed to store and provide the amount of HTF requested by the Gemasolar power block even in case of radiation lack. With this final aim, the HTF mass flow rate required for the steam generator has to be computed starting from the amount of steam that has to be produced for the turbine expansion. As a consequence, in order to calculate the latter parameter the nominal working conditions of the whole power block has to be simulated through an appropriate model before considering the overall Gemasolar system linking Rankine and salts circuit.

More in details, firstly the power block simulation is developed for the 19.9 MWel nominal production. In a second stage, the complex scenario is defined and modelled through the receiver transient tool. Finally the obtained results are linked together in order to couple the two system underlining how the storage system smooths the perturbation effects.

4.1 Power block model

In this section the power block simulation is developed through a in-house *Matlab* code according to the nominal conditions.

The main model assumptions are hereunder explained.

- The power plant is based on a SH-RH Rankine cycle (Superheated and Re-heated) characterized by a turbine inlet temperature of 542°C (T_1) and a maximum pressure of 105 bar (p_1) with an overall 19.9 MW_{el} power production in nominal conditions. All these general characteristics are taken from the available literature ([44]). On the other hand, water-steam properties have been obtained using *XSteam* as data source ([58]).

- Steam expansion process is divided in a high and low pressure turbine. The division is applied according to the relation hereunder proposed.

$$P_{HP,out} = \frac{1}{5} \cdot P_{HP,in} \tag{4.1}$$

- Steam is produced at the desired conditions through a three-sections heat exchanger (Economizer, Evaporator and Super-heater) in which the molten salts coming from the hot tank are used as heat source to the water-to-steam production. In this regard, a thermal efficiency of 0.85 is considered (η_{th}).

- A feed water structure of five FWH plus a deaerator is considered. As already mentioned a further heater (Economizer) is set as first section of the HTF-steam heat exchanger. The water temperature increase for each feed water heater is set imposing the follow empirical equation ([16]):

$$\Delta T_{FWH} = \frac{T_{sat}(Evap) - T_{sat}(Cond)}{Nr^{\circ}_{FWH} + 1} \tag{4.2}$$

  Steam bleeding pressure for the last FWH is set by default at 45 bar according to available literature ([28]). On the other hand, steam bleeding pressures for the LP turbine are set according to the saturated temperature required by the thermal equilibrium in each FWH.

- Deaerator pressure is set by default at 10 bar ([16] and [28]). The amount of steam that escapes with the vented gasses from the deaerator is neglected for sake of simplicity.

- Pressure losses and efficiency for each process are set according to values available in literature:

$\Delta p_{FWH} = 1\%$, $\Delta p_{RH} = 5\%$, $\Delta p_{HTF-steam\ HX} = 12\%$, $\Delta p_{bleeding} = 3\%$;

$\eta_{IS,HP} = 0.9$, $\eta_{IS,LP} = 0.82$, $\eta_{mec} = 0.96$, $\eta_{el} = 0.98$.

- A 30°C temperature is considered as the ambient condition according to the Andalusian climate. A final condensate-to-ambient air temperature difference of 10°C is set in the Condenser.

Using these values as starting point all the characteristic equations regarding mass flow rate, temperature and enthalpy are set for the whole plant power block. Among them, the main are hereunder reported.

- Mass equilibrium equations:

$$\dot{m}_2 = \dot{m}_1 - \dot{m}_{15} \tag{4.3}$$

$$\dot{m}_3 = \dot{m}_2 - \dot{m}_{16} \tag{4.4}$$

$$\dot{m}_4 = \dot{m}_3 - \dot{m}_{17} - \dot{m}_{18} - \dot{m}_{19} - \dot{m}_{20} \tag{4.5}$$

$$\dot{m}_5 = \dot{m}_4 + \dot{m}_{25} \tag{4.6}$$

$$\dot{m}_{11} = \dot{m}_{10} + \dot{m}_{22} + \dot{m}_{17} \tag{4.7}$$

- Energy equations in HP and LP turbines according to isoentropic efficiencies:

$$h_{15} = h_1 - \eta_{IS,HP} \cdot (h_1 - h_{15,IS}) \tag{4.8}$$

$$h_2 = h_{15} - \eta_{IS,HP} \cdot (h_{15} - h_{2,IS}) \tag{4.9}$$

$$h_4 = h_{20} - \eta_{IS,LP} \cdot (h_{20} - h_{4,IS}) \tag{4.10}$$

- Net specific work and power produced in each turbine sections. HP first section example:

$$W_{net\ first\ section} = (h_1 - h_{15}) \cdot \eta_{el} \cdot \eta_{mec} \tag{4.11}$$

$$P_{first\ section} = \dot{m}_1 \cdot W_{net\ first\ section} \tag{4.12}$$

- Feed water heater energy equations. First and last FWH examples:

$$\dot{m}_{15} = \frac{\dot{m}_{14} \cdot (h_{14} - h_{13})}{h_{15} - h_{21}} \tag{4.13}$$

$$\dot{m}_{20} = \frac{\dot{m}_7 \cdot (h_8 - h_7) - \dot{m}_{24} \cdot (h_{24} - h_{25})}{h_{20} - h_{25}} \tag{4.14}$$

An iteration process is then used to solve the system and compute the steam mass flow required by the cycle in order to guarantee the nominal power performances.

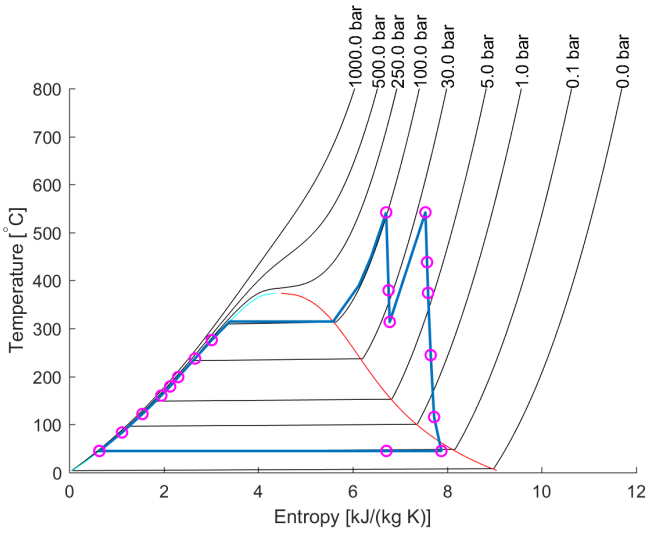

Figure 4.1: Temperature-Entropy diagram for the SH+RH steam Rankine cycle.

According to the plant layout scheme shown in figure 4.2, the main results are hereunder reported.

The principal aim of the power block model is the estimation of the steam mass flow rate at the HP and LP turbine inlet sections ($\dot{m}_{steam_1}$, $\dot{m}_{steam_3}$) . In fact, using these values in the energy balances of the HTF-steam heat exchanger and the re-heater, it is possible to compute the amount of molten salts required by the system to the steam generation in nominal conditions.

$$\dot{m}_{HTF_{HX}} \cdot (h_{hot\ tank} - h_{cold\ tank}) \cdot \eta_{th} = \dot{m}_{steam_1} \cdot (h_1 - h_{14}) \tag{4.15}$$

$$\dot{m}_{HTF_{RH}} \cdot (h_{hot\ tank} - h_{cold\ tank}) \cdot \eta_{th} = \dot{m}_{steam_3} \cdot (h_3 - h_2) \tag{4.16}$$

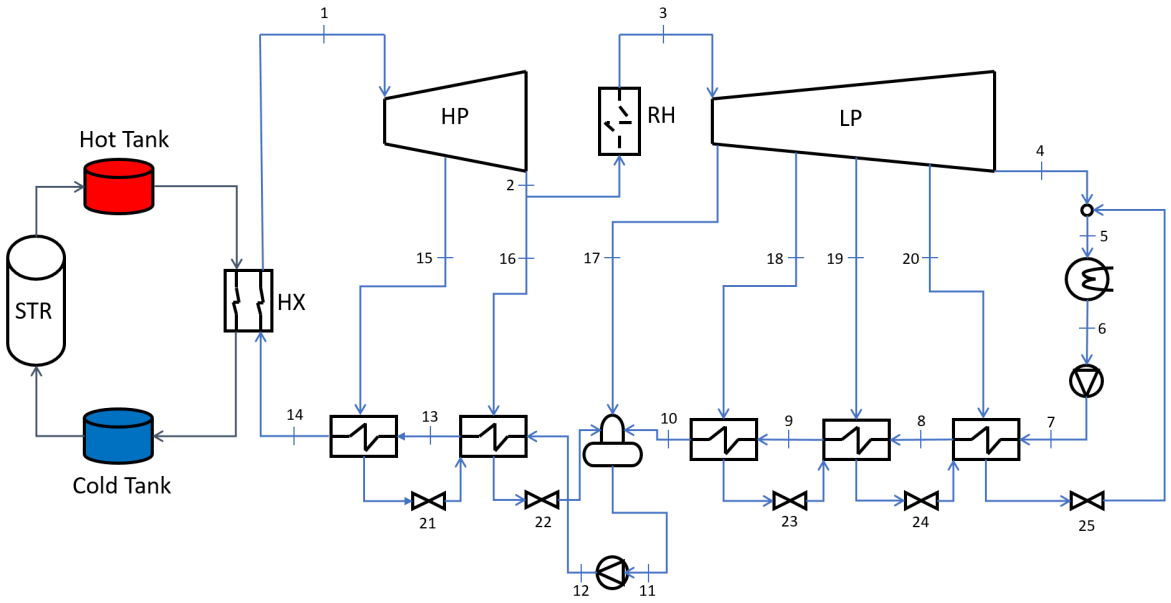

Figure 4.2: Gemasolar plant layout scheme.

	$\dot{m}_{steam}$ $[kg/s]$	p $[bar]$	T $[°C]$	h $[kJ/kg]$	s $[kJ/kgK]$
Point 1	17.0	105	542	3476.7	6.70
Point 2	15.7	21.6	313.8	3051.9	6.78
Point 3	14.6	20.5	542.0	3560.6	7.53
Point 4	11.6	0.09	45.0	2490.6	7.87
Point 5	13.2	0.09	45.0	2120.8	6.71
Point 6	13.2	0.09	45.0	2582.5	0.64
Point 9	13.2	10.09	122.0	512.9	1.55
Point 11	17.0	9.90	179.4	760.7	2.13
Point 14	17.0	117.32	276.1	1268.0	3.01
Point 16	1.2	21.00	313.8	3051.9	6.78
Point 18	1.0	6.45	374.3	3216.4	7.64
Point 20	0.9	0.56	115.7	2712.8	7.72

Table 4.1: Gemasolar power block main results.

	$\dot{m}_{HTF}$ $[kg/s]$
HTF-steam HX	89.95
Steam RH	39.21
Total	129.16

Table 4.2: HTF mass flow rate required.

4.2 Morning start-up process

4.2.1 Start-up modelling

In this section the morning start-up process has been simulated. In particular, the Gemasolar heating phenomena have been investigated starting from the March 21^{st} 6.30 am radiation conditions. In this regard, 7 heat flux maps have been directly obtained from *Delsol* software in between 6.30 am and 12 am (figure 4.3). In this way, the progressive increase in the HTF production rate and the transitory process that leads the plant up to nominal design conditions have been analysed in details. By assumption, no cloud perturbation has been added in this simulation and, as a consequence, the solar field resulted completely unshadowed during the whole process.

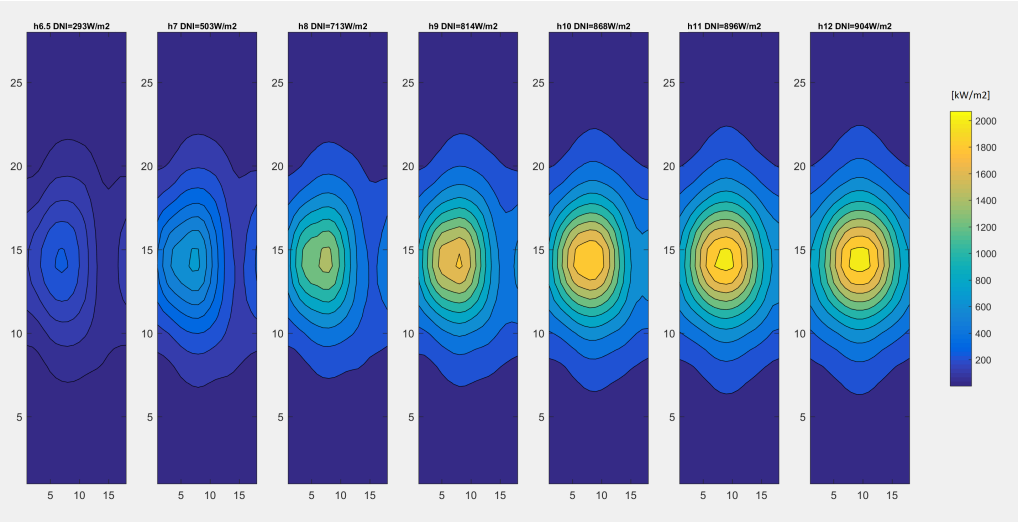

Figure 4.3: 21^{st} March heat flux maps. From left to right: 6.30 am, 7 am, 8 am, 9 am, 10 am, 11 am and 12 am.

In real operating conditions, the overall sum of the elapsed time for the considered heating process would be 5.5 hours (19800 s). In order to reduce the computational time needed by *Matlab* to provide the solution, the process has been virtually speeded up. In this regard, a time frame of 300 s has been considered as duration for each radiation map: this changing time resulted in fact the optimal trade off between *Matlab* processing time and the correct appreciation of the dynamic response of the system with respect to the heat flux steps. As a consequence, an overall 2100 s (35 minutes) process has been simulated (figure 4.4).

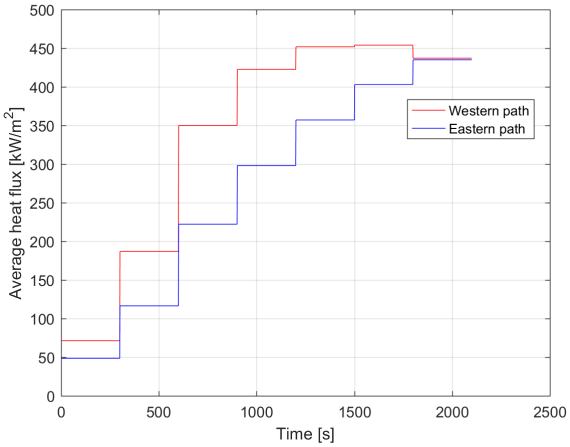

Figure 4.4: Average heat flux changing on time. Western and eastern path.

4.2.2 Start-up performances

According to the operating principle described in 4.3.1, the tool has been launched for both western and eastern paths. Results are hereunder shown graphically.

A complete switch off condition has been considered as the starting point of the present simulation. In fact, it has been verified that during the first radiation map (conditions at 6.30 am) the low heat flux values were not sufficient to guarantee any HTF production rate. Furthermore, even if a minimum mass flow rate was sent to the receiver the HTF outlet temperature would be lower than the inlet one causing possible solidification problems. In order to avoid these issues, the pump does not turn on until higher radiation values are verified (at least radiation map at 7 am). By the way, it has been assumed that radiation conditions in the early morning are able to pre-heat at least the pipes surfaces. In this regard, both HTF and pipe wall temperatures have been set for $time = 1\ s$ at 290 °C (cold tank temperature) for sake of simplicity.

After first 300 s, the higher radiations values of the second map guarantee the minimum plant start-up conditions. In this regard, a mass flow rate of 80 kg/s has been computed as the maximum HTF production rate through which 1°C HTF temperature increase is verified between the inlet and the outlet receiver section. Setting the latter as initial flow rate, the system can start working. In a first stage, the mass flow rate is kept constant by the control system because the outlet temperatures, still lower than 500°C, do not allow the fluid to be sent to the hot tank. This warm up process is more evident from an eastern path perspective due to lower heat flux values. Proceeding with the following radiation maps the control system starts regulate the flow rate in order to guarantee the target temperature conditions at the outlet section as described in section 3.3.1.

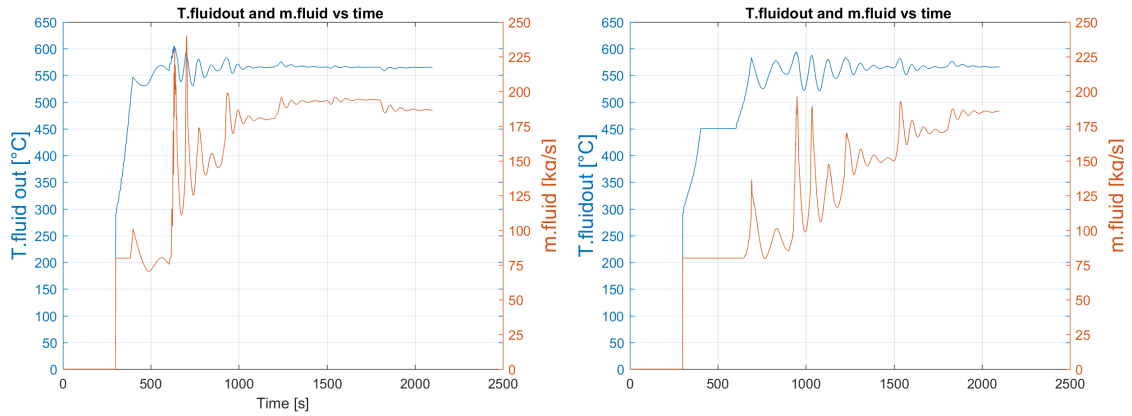

Figure 4.5: HTF mass flow rate and temperature at the outlet section. *a*) Western path, *b*) eastern path.

Comparing figure 4.5 *a*) and *b*) the different operative conditions of the eastern and western path have been underlined. Due to the different radiation profiles, the HTF production rates differ sensibly. Considering in fact a morning period, the HTF western path receives a higher heat flux from the correspondent portion of the solar field due to the sun position in the sky. This behaviour can be verified by the heliostats efficiencies in figure 4.6: higher efficiency values characterise the western portion of the solar field during the morning; vice-versa, during the afternoon the eastern portion is the one that can rely on higher radiation values.

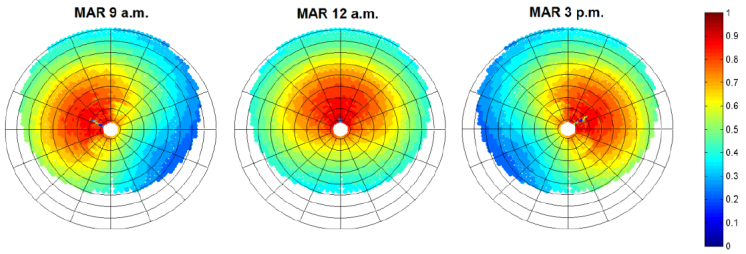

Figure 4.6: 21^{st} March heliostats efficiency. From left to right: 9 am, 12 am and 15 pm.

Proceeding from 6.30 am to 12 am this trend is progressively reduced up to mid-day, when the radiation map is completely symmetric and the same average heat flux value is verified for both western and eastern paths ($1800 \div 2100$ *s* in figure 4.4). For these reasons an higher mass flow rate is produced in the western path in most of the time-frame considered, until mid-day when a 196 kg/s production rate is verified for both eastern and western path.

As final observation, receiver system response resulted quicker in case of mass flow rates higher then 150 kg/s, while in case of lower values higher oscillations and a slower response of the system have been verified. In this regard, the trend can be explained considering the molten salts heat capacity: at same temperature profiles (meaning same thermal properties), higher the mass flow rate, higher the heat capacity. As a consequence, with a greater amount of HTF flowing in the pipes, the system can easily overcome radiation steps obtaining a new equilibrium conditions in lower than 300 s; on the other hand, with a low mass flow rate, a small step in the heat flux map is sufficient to consistently heat the HTF, destabilizing the system before the controller could operate accordingly.

Once solved the receiver performances, attention can be focused on the overall Gemasolar system. In this regard, using for the power block subsystem the same results obtained in section 4.1, tanks levels have been monitored.

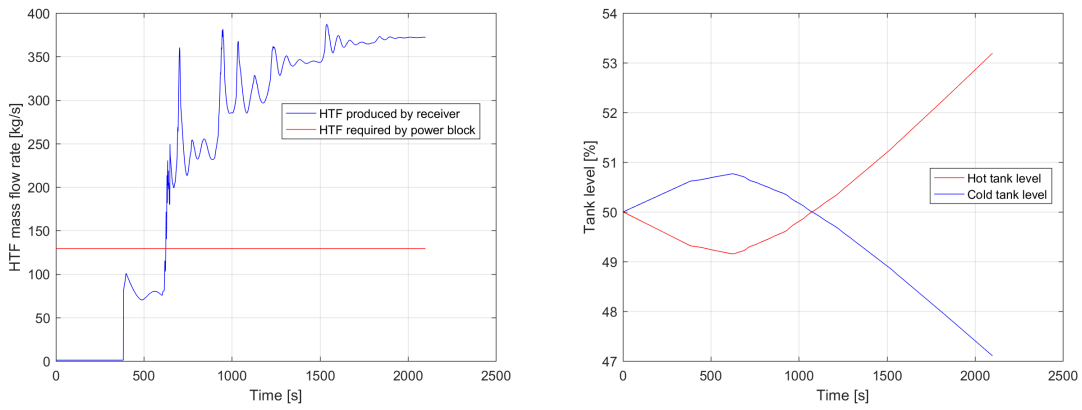

(a) **(b)**

Figure 4.7: Overall system. *a*) Produced vs required HTF mass flow rate, *b*) tanks levels.

As shown in figure 4.7, the power block completely relies on the heat storage system up to 7 am radiation conditions (600 s in the present simulation) while, proceeding throughout the day, the amount of molten salts guaranteed by the receiver is enough for both power block and heat storage filling purposes.

4.3 Clouds complex scenario

Up to now transient phenomena have been analysed only for the case of a single cloud passage. In this way, it was possible to design a suitable control system and investigate receiver characteristics according to different radiation boundary conditions. By the way, the main receiver function is to guarantee power block performances even in case of prolonged partial radiation conditions. Tanks are in fact exploited as thermal storage system in order to collect receiver excess production and make it available to the power block system when needed. In this regard, system performances have to be analysed also in the case of multiple clouds passage in order to underline heat storage system behaviour in both charge and discharge process according to radiation availability. Note that charge and discharge terms are used from the hot tank perspective: charge process is when due to good radiation conditions the hot tank is filling up; on the other hand, discharge process is verified when the hot tank is empting due to a considerable lack of radiation. Exploiting the developed tool it is possible to investigate both these phenomena adjusting *Solar Tool 5* output and linking receiver and power block models.

4.3.1 Operating principle

In this subsection is explained the operating principle of the overall tool developed for the analysis of complex scenarios.

- First of all the scenario object of the analysis has to be defined. For this reason, a further in-house code has been developed in order to select the overall time-frame and the different clouds models that characterize the scenario. Once defined these compiler parameters, the code launches *Solar Tool 5* and build the heat flux map for each time-step of the entire scenario according to the radiation conditions imposed by clouds passage. In this regard no clouds overlapping has been considered by assumption: each cloud shadows and unshadows completely the field before that the successive one reaches the power plant.

- According to the radiation map the receiver performances are computed through the transient model with the feed back controller regulations.

- Receiver and power block results are linked together and attention is shifted to tanks level. For sake of simplicity heat storage systems are assumed adiabatic and, as a consequence, thermal losses are neglected.

- According to HTF mass flow rate produced by the receiver and required by the power block, the tanks level variation is computed according to the variation

of the HTF stored volume. In a later stage, results are graphically shown for each time-step of the considered scenario. Hot and cold tanks are designed as cylinders characterised by a 10 meters height and 23 meters of diameter ([44]).

4.3.2 Hot tank charge simulation

Using the explained methodology both charge and discharge processes have been analysed at tank level. The environmental boundary conditions for the former are set on 21^{th} March at 12 am (design conditions), describing a typical spring day in Andalusia when sun rays are only interrupted by small and sporadic clouds.

In this regard, a time-frame horizon of approximately 30 minutes (1691 seconds) has been proposed characterizing a sequence of six clouds according to the following order.

Partial shadow left	*Small clouds*	*Two small clouds*	*Small cloud*	*Small cloud*	*Small cloud*

Table 4.3: Charge process: clouds sequence.

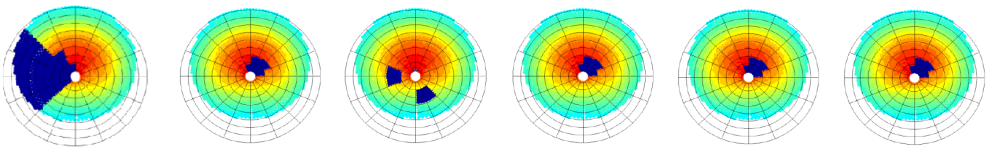

Figure 4.8: Charge process: clouds sequence with respect to heliostats field.

Simulation results are hereabove represented for both the overall HTF mass flow rate produced and tanks levels. As shown in both figures 4.9 *a*) and *b*), small clouds do not sensibly affect the system performances. A part from the first 200 seconds in which the heat flux map imposed by *Partial shadow left* stops the hot tank filling process, the overall HTF mass flow rate produced is in fact always greater than the value required by the power block. As a consequence, the slope of the real filling process (red continuous line in figure 4.9 *b*)) presents the same trend with respect to the ideal one based on the hypothesis of perfect radiation and clouds absence during the whole scenario (red dotted line in the same graph).

An overall 6% hot tank level increase is evidenced in the 30 minutes time-frame. As a consequence, enlarging the considered time-frame up to 9 hours (from 9 am to 18 pm) with the same radiation conditions as in the simulated case, it is possible to

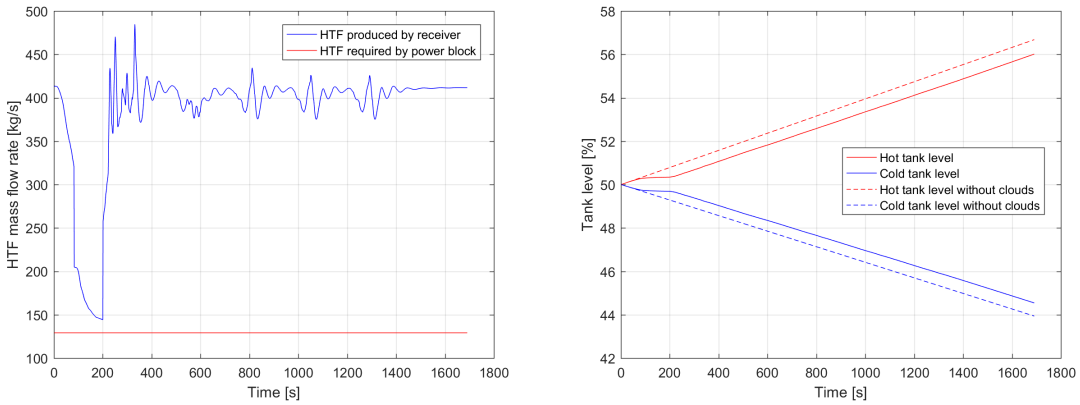

(a) **(b)**

Figure 4.9: Charge process: *a*) HTF mass flow rate produced and required, *b*) tanks levels.

affirm that the HTF mass flow rate produced by the receiver at the desired conditions results to be enough to completely fill up the hot tank (108%), guaranteeing at the same time the nominal work conditions of the power block. Of course this is only a consideration and not a rigorous demonstration: neither sun movement nor the heat flux values changing on time due to the different solar height throughout the day were considered. By the way, this analysis demonstrate the effectiveness of the heat storage system.

4.3.3 Hot tank discharge simulation

Hot tank discharge process has been analysed using the same methodology as in the previous case. The environmental boundary conditions for this case of study are set on 21^{th} December at 9 am (lowest radiation conditions), describing a winter day in which sun rays are continuously blocked by clouds.

In this regard, a time-frame horizon of approximately 30 minutes (1725 seconds) has been proposed characterizing a sequence of five clouds according to the following order.

Total shadow	*Total shadow*	*Total shadow as PS10*	*Total shadow*	*Total shadow*	*Total shadow*

Table 4.4: Discharge process: clouds sequence.

As reported in figure 4.11 *a*), the extended clouds considered in this analysis strongly affect the system causing prolonged stops in the HTF production. As

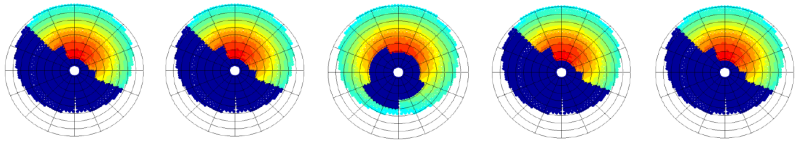

Figure 4.10: Discharge process: clouds sequence with respect to heliostats field.

a consequence, hot tank has to provide the amount of molten salts required by the power block nominal working conditions. Note that among the passages of two consecutive clouds a complete radiation period is still present due to the non-overlapping assumption. In this regard, the approximation is the main cause of the not appreciable decreasing trend in the hot tank level and, as a consequence, the simulation is not accurate.

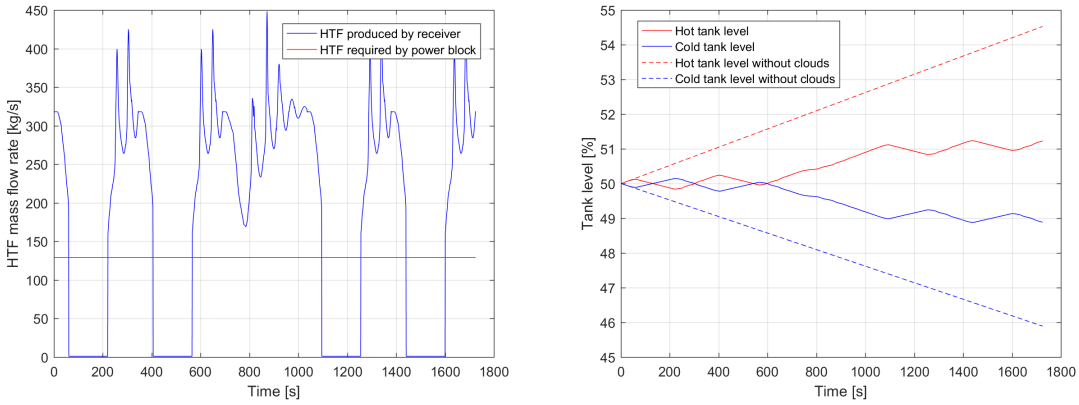

(a) **(b)**

Figure 4.11: Discharge process: *a*) HTF mass flow rate produced and required, *b*) tanks levels.

Conclusions and future works

Conclusions

In this thesis is presented the analysis of a commercial Solar Tower power plants (Gemasolar) characterised by off-design working conditions due to cloudy weather. The starting point was constituted by two previous dissertations (De Giorgi and Crespi-Zani) in which the various aiming strategies and the clouds modelling have been analysed according to different cases. The main result of the first thesis was a strategy able to reduce the peak fluxes on the receiver, without a strong reduction of the overall thermal power (aiming strategy 6). On the other hand, Crespi-Zani's work provided a tool able to simulate radiation conditions changing on time according to six clouds models.

Exploiting this technical background, the main result of the present dissertation is a complete model for the simulation of the power plant dynamic performances in case of real weather conditions. First of all, a time-scale analysis was developed according to the characteristic time-frame of a cloud passage, focusing the attention on all the equipment constituting the power plant. In this regard, power block system resulted not affected by perturbations thanks to the damping function of the heat storage system while, on the other hand, solar tower receiver was demonstrated to be the most important element from a dynamic response perspective. According to the considered time-frame it is in fact the element characterised by the same order of magnitude response time and, as a consequence, it was analysed in details through the development of a transient model.

In a later stage, the solar tower receiver was built using the geometrical informations available in literature and different pipes structures were designed. The whole receiver was modelled according to a suitable discretisation, trade off between computational cost and results accuracy. Successively a steady state model was developed using *Matlab* as compiler and two different configurations were tested. An 18 pipes panels - 2 HTF paths receiver was demonstrated to be the best option according to the safety working conditions imposed by the use of molten salts as thermal fluid. The developed stationary tool was then used to analyse the system according to different periods of the year and the available aiming strategies. In this

regard, aiming strategy 6 resulted to be the best solution also for a steady-state perspective guaranteeing a higher HTF production rate and a better receiver thermal efficiency (roughly +1% for both values).

After that, simplifying assumptions based on the heat capacities of both HTF and pipe were introduced for the transient problem characterisation and the dynamic performances of the system were modelled using *Matlab PDEPE* function and an in-house iterative code as solving tools. In particular, attention was focused on the molten salts inertial term while the pipe wall structure was considered in a quasi-steady state. At this stage, a sophisticated controller was required by the system in order to guarantee stability conditions and preserve the HTF from degradation issues. In this regard, the detected problem was the thin temperatures band in which the system could operate respecting the upper degradation limit and the lower one represented by the minimum temperature accepted by the storage system. In between feed back and feed forward the former case, enriched with variable coefficients, was demonstrated to be the most suitable solution for the control of the system. Thanks to under-relaxation factors variable with respect to the obtained error, the controller resulted more flexible accomplishing all the limits requirements guaranteeing also lowest temperatures gradient in the pipe walls.

Through the complete dynamic model of the receiver, all the available clouds were then analysed and compared in order to underline the different ways in which they affect the system from HTF production rate, HTF temperatures and pipe wall thermal gradient perspectives. Big clouds such as *Total shadow* and *Partial shadow left* were determined as the most problematic. The field shadowing imposed by these clouds determines in fact a complete stops in the HTF production rate and provokes a 30°C higher temperatures gradient in the pipes wall causing additional stress issues in the receiver. On the other hand, small clouds models slightly influence the system behaviour due to the small portion of the solar field that they shadow. As a results, they only decrease temporally the HTF production rate but they do not destabilize the system. Once analysed the power block in its nominal conditions, the whole power plant model was finally designed linking the receiver and the power block trough the two tanks and the HTF-steam heat exchanger. The overall system performances were simulated in both the best (21^{st} March 12 am) and worst radiation conditions (21^{st} December 9 am) underlining the heat storage importance. In this regard, tank charge process was analysed and an appreciable 6% hot tank level increase in the 30 minutes time-frame was obtained. On the other hand, the basic assumptions on the radiation map building did not allow to properly simulate the storage system discharge process.

Once summarized the work proposed and the results obtained, an analysis on the approach validity is hereunder proposed. Through the tanks level simulation

has been demonstrated how the main hypothesis of considering the power plant always working in nominal conditions was a suitable one. In fact, it is sufficient a low tanks level in order to guarantee the HTF supply required by the power block. On the other hand, the oversized receiver is able to fill the storage system with a considerable velocity.

The propose receiver structure was verified to guarantee HTF limit conditions in both stationary and transient conditions tanks to a suitable distribution of the paths with respect to the incoming radiation map.

Quasi-steady state approximation is the only assumption that cannot be verified through the obtained results. In this regard, future works are required to investigate the truthfulness of this assumption. In case this will not be verified it will be mandatory to develop a more accurate transient model.

The final outcome of this analysis is that heat storage system is the fundamental element in the overall power plant framework. Through the transient analysis of the receiver it is in fact demonstrated that big clouds passage completely stops HTF production shadowing the heliostats field and blocking the incoming solar radiation. Without an apposite storage system, this phenomenon would affect the power block system causing off-design working conditions for turbine and heat exchanger. The electrical production rate would decrease as a consequence and the same trend would be verified for the plant economic incomes. Furthermore, due to the transient operating conditions further thermal stresses would affect the power block requiring additional maintenance activities and causing, at the end, a lifetime reduction of the overall plant. On the other hand, exploiting the storage system filtering function all the perturbation effects are stopped at receiver level and power block keeps working in nominal conditions. In particular, the receiver excess production is conserved in tanks and is exploited later on in case of partial radiation.

In case of a sunny day with good radiation value the oversized receiver guarantees an excess amount of molten salts that can be exploited to extend electricity production also during the night. In this way, the equivalent working hours of Gemasolar power plant could be higher than any other traditional concentrated solar plant (Spanish *PS10* for instance).

From a general perspective, through the heat storage system a concentrated solar plant is partially released from the source unpredictability and, as a consequence, its power block can be managed as the one of a traditional plant. In this regard, plant performances are improved deciding a priori the best working conditions according to the amount of HTF stored in the tanks.

As final consideration, nowadays CSP technology coupled with heat storage system represents the state of the art for solar thermal energy exploitation.

Future works

This work is particularly useful because of the development of an algorithm able to evaluate the performances of a CSP power plant coupled with a heat storage system for both stationary and transient state according to real weather conditions. The developed tool can be the starting point for a multitude of further studies regarding both thermal and economic perspectives. Some of these possibilities are hereunder proposed.

- Thermal stresses evaluation

  A program to compute heat flux maps and related thermal maps has been developed in this work. A step forward in the evaluation of the impact that a transient process has on a solar receiver, is to study the real thermal stresses produced. Thermal gradient values and local peak flux variations are not enough to appreciate the receiver response; a deep study on the material properties subjected to high temperatures and mechanical stresses has to be done and later implemented in the model.

- System optimisation

  It would be interesting to optimise both the tanks and the solar field dimensions as trade off between the additional working hours of production that they can guarantee and the thermal losses to which they are subjected. An economic evaluation can be also modelled in order to underline additional incomes that an enlarged storage system can provide to the power plant with respect to the maintenance activities and the initial cost that it requires. Beside an analysis on the effects of an increase of the solar multiple factor (SM) with respect to the receiver and heat storage system has to be developed in order to complete the optimisation study.

- Power block off-design analysis

  In the present work the power block is assumed to work always at nominal conditions. By the way it would be interesting to design a model able to describe transient off-design conditions for the power block, analysing the case of plant start-up in which no HTF is available in the hot tank or simulating a storage system malfunctioning that requires extraordinary maintenance activities.

On the other hand, additional attention can be focused on the optimization of the present tool, improving the thermal model and reducing the number of simplifying assumptions in order to obtain more realistic results. In this regard, it is suggested to:

- Introduce thermal losses at tanks level;
- Consider pipe wall dynamic behaviour instead of the proposed quasi-steady state;
- Consider the heat exchanged in between two adjacent pipes in the same panel;
- Consider heat losses from the pipes to the internal structure of the tower receiver;
- Consider clouds overlapping in the complex scenario radiation map in order to simulate more realistic weather conditions;
- Improve the accuracy of the transient problem by consider a radiation map that change for each time-step of the considered time-frame. This aspect would require also an improvement in the heliostats field modelling increasing the number of flux units. The solar field has to be subdivided in more zones, in order to have a more defined shape of the clouds and thus define a more precise trajectory of the latter.
- Improve cloud shadowing effect. In this thesis, when a cloud passes over a mirror, the DNI sudden drops to zero. In reality, depending on its nature, a cloud leads to a variable reduction of DNI. For this reason, it is suggested to implement the code considering also the case in which a cloud reduces only partially the solar radiation. This increases for sure the precision of the simulation.
- Improve the control system method. In the present work feed back control system was selected as receiver controller methodology. By the way other possibility can be designed for the same purpose. The first idea could be to use the same method as for the HRSG attempering, where a cold amount of fluid is injected in between two section of the heat exchanger in order to properly control the steam temperatures conditions. In this regard, for the Gemasolar case the control system could manage two or more injection points between two consecutive pipes panels and it would have to compute the correct amount of HTF introduced to keep the fluid temperature among the fixed limits. Another options could be to design an overdumped controller that would be able to better control maximum peaks in the HTF mass flow rate curve.

Appendix A

Receiver stationary model

Listing A.1: Script for the receiver thermal model according to steady-state conditions. West path case

```
%% SOLUTION - WEST PATH

load initial_data

while error_mass_w>1e-1 %m_tot_fluid error
    m_fluid_tot_w=m_fluid_tot_w*(1+0.2*k_mass_w);

    error=100;
    while error>1e-2
        Tw_ext_old_w=Tw_ext_w;

        for p=1:M/2
            m_fluid_w(p)=m_fluid_tot_w/24;
            for j=1:N
                if j==1
                    if p==1
                        T_fluid_w(j,p)=T_inlet;
                        ent_fluid_w(j,p)=ent_in;
                    else
                        T_fluid_w(j,p)=T_fluid_w(end,p-1);
                        ent_fluid_w(j,p)=interp2(salts_pressure_prop,
                            salts_temperature_prop,salts_enthalpy_prop,P_fluid_w(
                            end,p-1),T_fluid_w(end,p-1));
                    end
                    %Fluid properties & h_conv_int
                    rho_fluid_w(j,p)=spline(salts_temperature_prop,
                        salts_density_prop,T_fluid_w(j,p));
                    my_fluid_w(j,p)=spline(salts_temperature_prop,
                        salts_dynamicviscosity_prop,T_fluid_w(j,p));
                    cp_fluid_w(j,p)=spline(salts_temperature_prop,salts_cp_prop,
                        T_fluid_w(j,p));
                    k_fluid_w(j,p)=spline(salts_temperature_prop,
                        salts_conductivity_prop,T_fluid_w(j,p));
                    vel_fluid_w(j,p) = m_fluid_w(p)/(rho_fluid_w(j,p)*A_pipe);

                    Pr_w(j,p) = my_fluid_w(j,p)*cp_fluid_w(j,p)/k_fluid_w(j,p);
                    Re_w(j,p) = vel_fluid_w(j,p)*d_int*rho_fluid_w(j,p)/my_fluid_w(
                        j,p);
```

```
32                  f_w(j,p) = (0.79*log(Re_w(j,p)) -1.64)^(-2);
33                  Nu_w(j,p) = ((f_w(j,p)/8)*(Re_w(j,p)-1000)*Pr_w(j,p))/(1+12.7*(
                        f_w(j,p)/8)^0.5*(Pr_w(j,p)^(2/3)-1));
34                  h_int_w(j,p) = Nu_w(j,p)*k_fluid_w(j,p)/d_int;
35
36                  DeltaP_w(j,p) = (f_w(j,p)*4*d_x*(0.5*vel_fluid_w(j,p)^2*
                        rho_fluid_w(j,p))/d_int)/(1e5);
37                  R_int_w(j,p) = 8/(h_int_w(j,p)*pi*2*r_int*d_x);
38                  R_tot_w(j,p) = R_int_w(j,p); %hp negligible conductance
                        resistance
39
40                  k_T_w(:,j,p)=0;
41                  error_w(:,j,p)=100;
42
43                  for i = 1:8
44                      if i==1
45                          %PARAMETRI CONV. NATURALE
46                          T_film_w(i,j,p)=(Tw_ext_w(i,j,p)+T_amb)/2;
47                          beta_w(i,j,p)=1/T_film_w(i,j,p);
48                          Gr_w(i,j,p)=(g*beta_w(i,j,p)*(Tw_ext_w(i,j,p)-T_amb)*(
                                d_x)^3)/(nu_air_w(i,j,p))^2;
49                          Ra_w(i,j,p)=Gr_w(i,j,p)*Pr_air_w(i,j,p);
50                          Nu_w(i,j,p)=0.68+(0.67*Ra_w(i,j,p)^0.25)/(1+(0.492/
                                Pr_air_w(i,j,p))^0.5625)^0.444; % --------
                                Churchill e Chun
51                          h_nat_w(i,j,p)=Nu_w(i,j,p)*k_air_w(i,j,p)/(d_x);
52
53                          %PERDITE TERMICHE
54                          q_abs_w(i,j,p) = q_rad_west(j,p)*d_x*r_ext*pi/4*cos(
                                teta(i));
55                          q_conv_w(i,j,p) = (h_forced(i,j,p)+h_nat_w(i,j,p))*(
                                Tw_ext_w(i,j,p)-T_amb)*d_x*r_ext*pi/4;
56                          q_rifl_w(i,j,p) = refl*q_abs_w(i,j,p);
57                          q_emes_w(i,j,p) = (d_x*r_ext*pi/4)*sigma*eps*F(i)*(
                                Tw_ext_w(i,j,p)^4 -T_sky^4);
58
59                          %SCAMBI TERMICI INTERNI
60                          q_trans_w(i,j,p) = q_abs_w(i,j,p) -q_conv_w(i,j,p) -
                                q_rifl_w(i,j,p) - q_emes_w(i,j,p);
                                                        q_tg_w(8,j,p) = (
                                Tw_ext_w(8,j,p) - Tw_ext_w(i,j,p)) / (R_sub);
61                          q_tg_w(8,j,p) = (Tw_ext_w(8,j,p) - Tw_ext_w(i,j,p)) / (
                                R_sub);
62                          q_tg_w(i,j,p) = (Tw_ext_w(i,j,p) - Tw_ext_w(i+1,j,p)) /
                                 (R_sub);
63                          q_lat_w(i,j,p) = (Tw_ext_w(i,j+1,p) - Tw_ext_w(i,j,p))
                                / R_lat;
64                          q_eff_w(i,j,p) = q_trans_w(i,j,p) - q_tg_w(i,j,p) +
                                q_tg_w(8,j,p) + q_lat_w(i,j,p);
65
66                          %CALCOLO NUOVA T
67                          Tw_ext_w(i,j,p) = T_fluid_w(j,p) + q_eff_w(i,j,p)*
                                R_tot_w(j,p);
68
69                      end
70                      if (i>=2) && (i<=4)
71                          %PARAMETRI CONV. NATURALE
72                          T_film_w(i,j,p)=(Tw_ext_w(i,j,p)+T_amb)/2;
73                          beta_w(i,j,p)=1/T_film_w(i,j,p);
```

```
74                          Gr_w(i,j,p)=(g*beta_w(i,j,p)*(Tw_ext_w(i,j,p)-T_amb)*(
                                d_x)^3)/(nu_air_w(i,j,p))^2;
75                          Ra_w(i,j,p)=Gr_w(i,j,p)*Pr_air_w(i,j,p);
76                          Nu_w(i,j,p)=0.68+(0.67*Ra_w(i,j,p)^0.25)/(1+(0.492/
                                Pr_air_w(i,j,p))^0.5625)^0.444; % --------
                                Churchill e Chun
77                          h_nat_w(i,j,p)=Nu_w(i,j,p)*k_air_w(i,j,p)/(d_x); %
                                --------------------------------- Churchill e Chun
78
79                          %PERDITE TERMICHE
80                          q_abs_w(i,j,p) = q_rad_west(j,p)*d_x*r_ext*pi/4*cos(
                                teta(i));
81                          q_conv_w(i,j,p) = (h_forced(i,j,p)+h_nat_w(i,j,p))*(
                                Tw_ext_w(i,j,p)-T_amb)*d_x*r_ext*pi/4;
82                          q_rifl_w(i,j,p) = refl*q_abs_w(i,j,p);
83                          q_emes_w(i,j,p) = (d_x*r_ext*pi/4)*sigma*eps*F(i)*(
                                Tw_ext_w(i,j,p)^4 -T_sky^4);
84
85                          %SCAMBI TERMICI INTERNI
86                          q_trans_w(i,j,p) = (q_abs_w(i,j,p) -q_conv_w(i,j,p) -
                                q_rifl_w(i,j,p) - q_emes_w(i,j,p));
87                          q_tg_w(i-1,j,p) = (Tw_ext_w(i-1,j,p) - Tw_ext_w(i,j,p))
                                 / (R_sub);
88                          q_tg_w(i,j,p) = (Tw_ext_w(i,j,p) - Tw_ext_w(i+1,j,p)) /
                                 (R_sub);
89                          q_lat_w(i,j,p) = (Tw_ext_w(i,j+1,p)-Tw_ext_w(i,j,p))/
                                R_lat;
90                          q_eff_w(i,j,p) = q_trans_w(i,j,p) + q_tg_w(i-1,j,p) -
                                q_tg_w(i,j,p) + q_lat_w(i,j,p);
91
92                          %CALCOLO NUOVA T
93                          Tw_ext_w(i,j,p) = T_fluid_w(j,p) + q_eff_w(i,j,p)*
                                R_tot_w(j,p);
94
95                      end
96                      if (i>=5) && (i<=7);
97                          %SCAMBI TERMICI INTERNI
98                          q_tg_w(i-1,j,p) = (Tw_ext_w(i-1,j,p) - Tw_ext_w(i,j,p))
                                 / (R_sub);
99                          q_tg_w(i,j,p) = (Tw_ext_w(i,j,p) - Tw_ext_w(i+1,j,p)) /
                                 (R_sub);
100                         q_lat_w(i,j,p) = (Tw_ext_w(i,j+1,p)-Tw_ext_w(i,j,p))/
                                R_lat;
101                         q_eff_w(i,j,p) = q_tg_w(i-1,j,p) - q_tg_w(i,j,p) +
                                q_lat_w(i,j,p);
102
103                         %CALCOLO NUOVA T
104                         Tw_ext_w(i,j,p) = T_fluid_w(j,p) + q_eff_w(i,j,p)*
                                R_tot_w(j,p);
105
106                     end
107                     if i==8
108                         %SCAMBI TERMICI INTERNI
109                         q_tg_w(i,j,p) = (Tw_ext_w(i,j,p) - Tw_ext_w(1,j,p)) / (
                                R_sub);
110                         q_tg_w(i-1,j,p) = (Tw_ext_w(i-1,j,p) - Tw_ext_w(i,j,p))
                                 / (R_sub);
111                         q_lat_w(i,j,p) = (Tw_ext_w(i,j+1,p)-Tw_ext_w(i,j,p))/
                                R_lat;
```

```
112                         q_eff_w(i,j,p) = q_tg_w(i-1,j,p)-q_tg_w(i,j,p) +
                                q_lat_w(i,j,p);
113
114                         %CALCOLO NUOVA T
115                         Tw_ext_w(i,j,p) = T_fluid_w(j,p) + q_eff_w(i,j,p)*
                                R_tot_w(j,p);
116
117                     end
118
119                     T_mean_w(j,p) = mean(Tw_ext_new_w(1:4,j,p));
120                     T_film2_w(j,p) = (T_mean_w(j,p)+T_amb)/2;
121
122                     for i=1:4
123                         nu_air_w(i,j,p)=interp2(air_pressure_prop,
                                air_temperature_prop,air_kinematic_viscosity_prop,
                                P_amb,T_film2_w(j,p),'spline');
124                         Pr_air_w(i,j,p)=interp2(air_pressure_prop,
                                air_temperature_prop,air_prandtl_prop,P_amb,
                                T_film2_w(j,p),'spline');
125                         k_air_w(i,j,p)=interp2(air_pressure_prop,
                                air_temperature_prop,air_conductivity_prop,P_amb,
                                T_film2_w(j,p),'spline');
126                     end
127                 end
128
129                 if p==1
130                     P_fluid_w(j,p)=P_in;
131                 else
132                     P_fluid_w(j,p)=P_fluid_w(end,p-1);
133                 end
134                 q_TOT_w(j,p)=(Tw_ext_w(1,j,p)-T_fluid_w(j,p))/R_tot_w(j,p)+(
                        Tw_ext_w(2,j,p)-T_fluid_w(j,p))/R_tot_w(j,p)+(Tw_ext_w(3,j,
                        p)-T_fluid_w(j,p))/R_tot_w(j,p)+(Tw_ext_w(4,j,p)-T_fluid_w(
                        j,p))/R_tot_w(j,p)...
135                         +(Tw_ext_w(5,j,p)-T_fluid_w(j,p))/R_tot_w(j,p)+(Tw_ext_w(6,
                            j,p)-T_fluid_w(j,p))/R_tot_w(j,p)+(Tw_ext_w(7,j,p)-
                            T_fluid_w(j,p))/R_tot_w(j,p)+(Tw_ext_w(8,j,p)-T_fluid_w
                            (j,p))/R_tot_w(j,p);
136
137                 T_fluid_w(j+1,p)= q_TOT_w(j,p) / (m_fluid_w(p)*cp_fluid_w(j,p))
                         + T_fluid_w(j,p);
138                 P_fluid_w(j+1,p) = P_fluid_w(j,p) - DeltaP_w(j,p);
139                 ent_fluid_w(j+1,p)=interp2(salts_pressure_prop,
                        salts_temperature_prop,salts_enthalpy_prop,P_fluid_w(j+1,p)
                        ,T_fluid_w(j+1,p));
140
141             elseif (j>=2) && (j<=N-1)
142                 %Fluid properties & h_conv_int
143                 rho_fluid_w(j,p)=spline(salts_temperature_prop,
                        salts_density_prop,T_fluid_w(j,p));
144                 my_fluid_w(j,p)=spline(salts_temperature_prop,
                        salts_dynamicviscosity_prop,T_fluid_w(j,p));
145                 cp_fluid_w(j,p)=spline(salts_temperature_prop,salts_cp_prop,
                        T_fluid_w(j,p));
146                 k_fluid_w(j,p)=spline(salts_temperature_prop,
                        salts_conductivity_prop,T_fluid_w(j,p));
147                 vel_fluid_w(j,p) = m_fluid_w(p)/(rho_fluid_w(j,p)*A_pipe);
148
149                 Pr_w(j,p) = my_fluid_w(j,p)*cp_fluid_w(j,p)/k_fluid_w(j,p);
```

```
150                     Re_w(j,p) = vel_fluid_w(j,p)*d_int*rho_fluid_w(j,p)/my_fluid_w(
                            j,p);
151                     f_w(j,p) = (0.79*log(Re_w(j,p)) -1.64)^(-2);
152                     Nu_w(j,p) = ((f_w(j,p)/8)*(Re_w(j,p)-1000)*Pr_w(j,p))/(1+12.7*(
                            f_w(j,p)/8)^0.5*(Pr_w(j,p)^(2/3)-1));
153                     h_int_w(j,p) = Nu_w(j,p)*k_fluid_w(j,p)/d_int;
154
155                     DeltaP_w(j,p) = (f_w(j,p)*4*d_x*(0.5*vel_fluid_w(j,p)^2*
                            rho_fluid_w(j,p))/d_int)/(1e5);
156                     R_int_w(j,p) = 8/(h_int_w(j,p)*pi*2*r_int*d_x);
157                     R_tot_w(j,p) = R_int_w(j,p); %hp negligible conductance
                            resistance
158
159                     k_T_w(:,j,p)=0;
160                     error_w(:,j,p)=100;
161
162                     for i = 1:8
163                         if Tw_ext_w(i,j,p)<T_amb
164                             Tw_ext_w(i,j,p) = T_amb +5;
165                         end
166
167                         if i==1
168                             %PARAMETRI CONV. NATURALE
169                             T_film_w(i,j,p)=(Tw_ext_w(i,j,p)+T_amb)/2;
170                             beta_w(i,j,p)=1/T_film_w(i,j,p);
171                             Gr_w(i,j,p)=(g*beta_w(i,j,p)*(Tw_ext_w(i,j,p)-T_amb)*(
                                    d_x)^3)/(nu_air_w(i,j,p))^2;
172                             Ra_w(i,j,p)=Gr_w(i,j,p)*Pr_air_w(i,j,p);
173                             Nu_w(i,j,p)=0.68+(0.67*Ra_w(i,j,p)^0.25)/(1+(0.492/
                                    Pr_air_w(i,j,p))^0.5625)^0.444; % --------
                                    Churchill e Chun
174                             h_nat_w(i,j,p)=Nu_w(i,j,p)*k_air_w(i,j,p)/(d_x); %
                                    ---------------------------------- Churchill e Chun
175
176                             %PERDITE TERMICHE
177                             q_abs_w(i,j,p) = q_rad_west(j,p)*d_x*r_ext*pi/4*cos(
                                    teta(i));
178                             q_conv_w(i,j,p) = (h_forced(i,j,p)+h_nat_w(i,j,p))*(
                                    Tw_ext_w(i,j,p)-T_amb)*d_x*r_ext*pi/4;
179                             q_rifl_w(i,j,p) = refl*q_abs_w(i,j,p);
180                             q_emes_w(i,j,p) = (d_x*r_ext*pi/4)*sigma*eps*F(i)*(
                                    Tw_ext_w(i,j,p)^4 -T_sky^4);
181
182                             %SCAMBI TERMICI INTERNI
183                             q_trans_w(i,j,p) = (q_abs_w(i,j,p) -q_conv_w(i,j,p) -
                                    q_rifl_w(i,j,p) - q_emes_w(i,j,p));
184                             q_tg_w(i,j,p) = (Tw_ext_w(i,j,p) - Tw_ext_w(i+1,j,p)) /
                                     (R_sub);
185                             q_tg_w(8,j,p) = (Tw_ext_w(8,j,p) - Tw_ext_w(i,j,p)) / (
                                    R_sub);
186                             q_lat_w(i,j-1,p) = (Tw_ext_w(i,j,p)-Tw_ext_w(i,j-1,p))/
                                    R_lat;
187                             q_lat_w(i,j,p) = (Tw_ext_w(i,j+1,p)-Tw_ext_w(i,j,p))/
                                    R_lat;
188                             q_eff_w(i,j,p) = q_trans_w(i,j,p) - q_tg_w(i,j,p) +
                                    q_tg_w(8,j,p) + q_lat_w(i,j,p) - q_lat_w(i,j-1,p);
189
190                             %CALCOLO NUOVA T
```

```
191                         Tw_ext_w(i,j,p) = T_fluid_w(j,p) + q_eff_w(i,j,p)*
                                R_tot_w(j,p);
192
193                     end
194                     if (i>=2) && (i<=4)
195                         %PARAMETRI CONV. NATURALE
196                         T_film_w(i,j,p)=(Tw_ext_w(i,j,p)+T_amb)/2;
197                         beta_w(i,j,p)=1/T_film_w(i,j,p);
198                         Gr_w(i,j,p)=(g*beta_w(i,j,p)*(Tw_ext_w(i,j,p)-T_amb)*(
                                d_x)^3)/(nu_air_w(i,j,p))^2;
199                         Ra_w(i,j,p)=Gr_w(i,j,p)*Pr_air_w(i,j,p);
200                         Nu_w(i,j,p)=0.68+(0.67*Ra_w(i,j,p)^0.25)/(1+(0.492/
                                Pr_air_w(i,j,p))^0.5625)^0.444; % --------
                                Churchill e Chun
201                         h_nat_w(i,j,p)=Nu_w(i,j,p)*k_air_w(i,j,p)/(d_x); %
                                -------------------------------- Churchill e Chun
202
203                         %PERDITE TERMICHE
204                         q_abs_w(i,j,p) = q_rad_west(j,p)*d_x*r_ext*pi/4*cos(
                                teta(i));
205                         q_conv_w(i,j,p) = (h_forced(i,j,p)+h_nat_w(i,j,p))*(
                                Tw_ext_w(i,j,p)-T_amb)*d_x*r_ext*pi/4;
206                         q_rifl_w(i,j,p) = refl*q_abs_w(i,j,p);
207                         q_emes_w(i,j,p) = (d_x*r_ext*pi/4)*sigma*eps*F(i)*(
                                Tw_ext_w(i,j,p)^4 -T_sky^4);
208
209                         %SCAMBI TERMICI INTERNI
210                         q_trans_w(i,j,p) = (q_abs_w(i,j,p) -q_conv_w(i,j,p) -
                                q_rifl_w(i,j,p) - q_emes_w(i,j,p));
211                         q_tg_w(i-1,j,p) = (Tw_ext_w(i-1,j,p) - Tw_ext_w(i,j,p))
                                 / (R_sub);
212                         q_tg_w(i,j,p) = (Tw_ext_w(i,j,p) - Tw_ext_w(i+1,j,p)) /
                                 (R_sub);
213                         q_lat_w(i,j-1,p) = (Tw_ext_w(i,j,p)-Tw_ext_w(i,j-1,p))/
                                R_lat;
214                         q_lat_w(i,j,p) = (Tw_ext_w(i,j+1,p)-Tw_ext_w(i,j,p))/
                                R_lat;
215                         q_eff_w(i,j,p) = q_trans_w(i,j,p) + q_tg_w(i-1,j,p) -
                                q_tg_w(i,j,p) + q_lat_w(i,j,p) - q_lat_w(i,j-1,p);
216
217                         %CALCOLO NUOVA T
218                         Tw_ext_w(i,j,p) = T_fluid_w(j,p) + q_eff_w(i,j,p)*
                                R_tot_w(j,p);
219
220                     end
221                     if (i>=5) && (i<=7);
222                         %SCAMBI TERMICI INTERNI
223                         q_tg_w(i-1,j,p) = (Tw_ext_w(i-1,j,p) - Tw_ext_w(i,j,p))
                                 / (R_sub);
224                         q_tg_w(i,j,p) = (Tw_ext_w(i,j,p) - Tw_ext_w(i+1,j,p)) /
                                 (R_sub);
225                         q_lat_w(i,j-1,p) = (Tw_ext_w(i,j,p)-Tw_ext_w(i,j-1,p))/
                                R_lat;
226                         q_lat_w(i,j,p) = (Tw_ext_w(i,j+1,p)-Tw_ext_w(i,j,p))/
                                R_lat;
227                         q_eff_w(i,j,p) = q_tg_w(i-1,j,p) - q_tg_w(i,j,p) +
                                q_lat_w(i,j,p) - q_lat_w(i,j-1,p);
228
229                         %CALCOLO NUOVA T
```

```
230                         Tw_ext_w(i,j,p) = T_fluid_w(j,p) + q_eff_w(i,j,p)*
                                R_tot_w(j,p);
231
232                     end
233                     if i==8
234                         %SCAMBI TERMICI INTERNI
235                         q_tg_w(i-1,j,p) = (Tw_ext_w(i-1,j,p) - Tw_ext_w(i,j,p))
                                / (R_sub);
236                         q_tg_w(i,j,p) = (Tw_ext_w(i,j,p) - Tw_ext_w(1,j,p)) / (
                                R_sub);
237                         q_lat_w(i,j-1,p) = (Tw_ext_w(i,j,p)-Tw_ext_w(i,j-1,p))/
                                R_lat;
238                         q_lat_w(i,j,p) = (Tw_ext_w(i,j+1,p)-Tw_ext_w(i,j,p))/
                                R_lat;
239                         q_eff_w(i,j,p) = q_tg_w(i-1,j,p) - q_tg_w(i,j,p) +
                                q_lat_w(i,j,p) - q_lat_w(i,j-1,p);
240
241                         %CALCOLO NUOVA T
242                         Tw_ext_w(i,j,p) = T_fluid_w(j,p) + q_eff_w(i,j,p)*
                                R_tot_w(j,p);
243
244                     end
245
246                     T_mean_w(j,p) = mean(Tw_ext_new_w(1:4,j,p));
247                     T_film2_w(j,p) = (T_mean_w(j,p)+T_amb)/2;
248
249                     for i=1:4
250                         nu_air_w(i,j,p)=interp2(air_pressure_prop,
                                air_temperature_prop,air_kinematic_viscosity_prop,
                                P_amb,T_film2_w(j,p),'spline');
251                         Pr_air_w(i,j,p)=interp2(air_pressure_prop,
                                air_temperature_prop,air_prandtl_prop,P_amb,
                                T_film2_w(j,p),'spline');
252                         k_air_w(i,j,p)=interp2(air_pressure_prop,
                                air_temperature_prop,air_conductivity_prop,P_amb,
                                T_film2_w(j,p),'spline');
253                     end
254                 end
255                 q_TOT_w(j,p)=(Tw_ext_w(1,j,p)-T_fluid_w(j,p))/R_tot_w(j,p)+(
                        Tw_ext_w(2,j,p)-T_fluid_w(j,p))/R_tot_w(j,p)+(Tw_ext_w(3,j,
                        p)-T_fluid_w(j,p))/R_tot_w(j,p)+(Tw_ext_w(4,j,p)-T_fluid_w(
                        j,p))/R_tot_w(j,p)...
256                     +(Tw_ext_w(5,j,p)-T_fluid_w(j,p))/R_tot_w(j,p)+(Tw_ext_w(6,
                        j,p)-T_fluid_w(j,p))/R_tot_w(j,p)+(Tw_ext_w(7,j,p)-
                        T_fluid_w(j,p))/R_tot_w(j,p)+(Tw_ext_w(8,j,p)-T_fluid_w
                        (j,p))/R_tot_w(j,p);
257
258                 T_fluid_w(j+1,p)= q_TOT_w(j,p) / (m_fluid_w(p)*cp_fluid_w(j,p))
                        + T_fluid_w(j,p);
259                 P_fluid_w(j+1,p) = P_fluid_w(j,p) - DeltaP_w(j,p);
260                 ent_fluid_w(j+1,p)=interp2(salts_pressure_prop,
                        salts_temperature_prop,salts_enthalpy_prop, P_fluid_w(j+1,p
                        ),T_fluid_w(j+1,p));
261
262             else %caso j==N
263                 %Fluid properties & h_conv_int
264                 rho_fluid_w(j,p)=spline(salts_temperature_prop,
                        salts_density_prop,T_fluid_w(j,p));
```

```
265                 my_fluid_w(j,p)=spline(salts_temperature_prop,
                        salts_dynamicviscosity_prop,T_fluid_w(j,p));
266                 cp_fluid_w(j,p)=spline(salts_temperature_prop,salts_cp_prop,
                        T_fluid_w(j,p));
267                 k_fluid_w(j,p)=spline(salts_temperature_prop,
                        salts_conductivity_prop,T_fluid_w(j,p));
268                 vel_fluid_w(j,p) = m_fluid_w(p)/(rho_fluid_w(j,p)*A_pipe);
269
270                 Pr_w(j,p) = my_fluid_w(j,p)*cp_fluid_w(j,p)/k_fluid_w(j,p);
271                 Re_w(j,p) = vel_fluid_w(j,p)*d_int*rho_fluid_w(j,p)/my_fluid_w(
                        j,p);
272                 f_w(j,p) = (0.79*log(Re_w(j,p)) -1.64)^(-2);
273                 Nu_w(j,p) = ((f_w(j,p)/8)*(Re_w(j,p)-1000)*Pr_w(j,p))/(1+12.7*(
                        f_w(j,p)/8)^0.5*(Pr_w(j,p)^(2/3)-1));
274                 h_int_w(j,p) = Nu_w(j,p)*k_fluid_w(j,p)/d_int;
275
276                 DeltaP_w(j,p) = (f_w(j,p)*4*d_x*(0.5*vel_fluid_w(j,p)^2*
                        rho_fluid_w(j,p))/d_int)/(1e5);
277                 R_int_w(j,p) = 8/(h_int_w(j,p)*pi*2*r_int*d_x);
278                 R_tot_w(j,p) = R_int_w(j,p); %hp negligible conductance
                        resistance
279
280                 k_T_w(:,j,p)=0;
281                 error_w(:,j,p)=100;
282
283                 for i = 1:8
284                     if Tw_ext_w(i,j,p)<T_amb
285                         Tw_ext_w(i,j,p) = T_amb +5;
286                     end
287
288                     if i==1
289                         %PARAMETRI CONV. NATURALE
290                         T_film_w(i,j,p)=(Tw_ext_w(i,j,p)+T_amb)/2;
291                         beta_w(i,j,p)=1/T_film_w(i,j,p);
292                         Gr_w(i,j,p)=(g*beta_w(i,j,p)*(Tw_ext_w(i,j,p)-T_amb)*(
                                d_x)^3)/(nu_air_w(i,j,p))^2;
293                         Ra_w(i,j,p)=Gr_w(i,j,p)*Pr_air_w(i,j,p);
294                         Nu_w(i,j,p)=0.68+(0.67*Ra_w(i,j,p)^0.25)/(1+(0.492/
                                Pr_air_w(i,j,p))^0.5625)^0.444; % --------
                                Churchill e Chun
295                         h_nat_w(i,j,p)=Nu_w(i,j,p)*k_air_w(i,j,p)/(d_x); %
                                --------------------------------- Churchill e Chun
296
297                         %PERDITE TERMICHE
298                         q_abs_w(i,j,p) = q_rad_west(j,p)*d_x*r_ext*pi/4*cos(
                                teta(i));
299                         q_conv_w(i,j,p) = (h_forced(i,j,p)+h_nat_w(i,j,p))*(
                                Tw_ext_w(i,j,p)-T_amb)*d_x*r_ext*pi/4;
300                         q_rifl_w(i,j,p) = refl*q_abs_w(i,j,p);
301                         q_emes_w(i,j,p) = (d_x*r_ext*pi/4)*sigma*eps*F(i)*(
                                Tw_ext_w(i,j,p)^4 -T_sky^4);
302
303                         %SCAMBI TERMICI INTERNI
304                         q_trans_w(i,j,p) = (q_abs_w(i,j,p) -q_conv_w(i,j,p) -
                                q_rifl_w(i,j,p) - q_emes_w(i,j,p));
305                         q_tg_w(i,j,p) = (Tw_ext_w(i,j,p) - Tw_ext_w(i+1,j,p)) /
                                 (R_sub);
306                         q_tg_w(8,j,p) = (Tw_ext_w(8,j,p) - Tw_ext_w(i,j,p)) / (
                                R_sub);
```

```
307                         q_lat_w(i,j-1,p) = (Tw_ext_w(i,j,p)-Tw_ext_w(i,j-1,p))/
                                R_lat;
308                         q_eff_w(i,j,p) = q_trans_w(i,j,p) - q_tg_w(i,j,p) +
                                q_tg_w(8,j,p) - q_lat_w(i,j-1,p);
309
310                         %CALCOLO NUOVA T
311                         Tw_ext_w(i,j,p) = T_fluid_w(j,p) + q_eff_w(i,j,p)*
                                R_tot_w(j,p);
312
313                     end
314                     if (i>=2) && (i<=4)
315                         %PARAMETRI CONV. NATURALE
316                         T_film_w(i,j,p)=(Tw_ext_w(i,j,p)+T_amb)/2;
317                         beta_w(i,j,p)=1/T_film_w(i,j,p);
318                         Gr_w(i,j,p)=(g*beta_w(i,j,p)*(Tw_ext_w(i,j,p)-T_amb)*(
                                d_x)^3)/(nu_air_w(i,j,p))^2;
319                         Ra_w(i,j,p)=Gr_w(i,j,p)*Pr_air_w(i,j,p);
320                         Nu_w(i,j,p)=0.68+(0.67*Ra_w(i,j,p)^0.25)/(1+(0.492/
                                Pr_air_w(i,j,p))^0.5625)^0.444; % --------
                                Churchill e Chun
321                         h_nat_w(i,j,p)=Nu_w(i,j,p)*k_air_w(i,j,p)/(d_x); %
                                --------------------------------- Churchill e Chun
322
323                         %PERDITE TERMICHE
324                         q_abs_w(i,j,p) = q_rad_west(j,p)*d_x*r_ext*pi/4*cos(
                                teta(i));
325                         q_conv_w(i,j,p) = (h_forced(i,j,p)+h_nat_w(i,j,p))*(
                                Tw_ext_w(i,j,p)-T_amb)*d_x*r_ext*pi/4;
326                         q_rifl_w(i,j,p) = refl*q_abs_w(i,j,p);
327                         q_emes_w(i,j,p) = (d_x*r_ext*pi/4)*sigma*eps*F(i)*(
                                Tw_ext_w(i,j,p)^4 -T_sky^4);
328
329                         %SCAMBI TERMICI INTERNI
330                         q_trans_w(i,j,p) = (q_abs_w(i,j,p) -q_conv_w(i,j,p) -
                                q_rifl_w(i,j,p) - q_emes_w(i,j,p));
331                         q_tg_w(i-1,j,p) = (Tw_ext_w(i-1,j,p) - Tw_ext_w(i,j,p))
                                 / (R_sub);
332                         q_tg_w(i,j,p) = (Tw_ext_w(i,j,p) - Tw_ext_w(i+1,j,p)) /
                                 (R_sub);
333                         q_lat_w(i,j-1,p) = (Tw_ext_w(i,j,p)-Tw_ext_w(i,j-1,p))/
                                R_lat;
334                         q_eff_w(i,j,p) = q_trans_w(i,j,p) + q_tg_w(i-1,j,p) -
                                q_tg_w(i,j,p) - q_lat_w(i,j-1,p);
335
336                         %CALCOLO NUOVA T
337                         Tw_ext_w(i,j,p) = T_fluid_w(j,p) + q_eff_w(i,j,p)*
                                R_tot_w(j,p);
338
339                     end
340                     if (i>=5) && (i<=7);
341                         %SCAMBI TERMICI INTERNI
342                         q_tg_w(i-1,j,p) = (Tw_ext_w(i-1,j,p) - Tw_ext_w(i,j,p))
                                 / (R_sub);
343                         q_tg_w(i,j,p) = (Tw_ext_w(i,j,p) - Tw_ext_w(i+1,j,p)) /
                                 (R_sub);
344                         q_lat_w(i,j-1,p) = (Tw_ext_w(i,j,p)-Tw_ext_w(i,j-1,p))/
                                R_lat;
345                         q_eff_w(i,j,p) = q_tg_w(i-1,j,p) - q_tg_w(i,j,p) -
                                q_lat_w(i,j-1,p);
```

```
346
347                         %CALCOLO NUOVA T
348                         Tw_ext_w(i,j,p) = T_fluid_w(j,p) + q_eff_w(i,j,p)*
                                R_tot_w(j,p);
349
350                     end
351                     if i==8
352                         %SCAMBI TERMICI INTERNI
353                         q_tg_w(i-1,j,p) = (Tw_ext_w(i-1,j,p) - Tw_ext_w(i,j,p))
                                 / (R_sub);
354                         q_tg_w(i,j,p) = (Tw_ext_w(i,j,p) - Tw_ext_w(1,j,p)) / (
                                R_sub);
355                         q_lat_w(i,j-1,p) = (Tw_ext_w(i,j,p)-Tw_ext_w(i,j-1,p))/
                                R_lat;
356                         q_eff_w(i,j,p) = q_tg_w(i-1,j,p) - q_tg_w(i,j,p) -
                                q_lat_w(i,j-1,p);
357
358                         %CALCOLO NUOVA T
359                         Tw_ext_w(i,j,p) = T_fluid_w(j,p) + q_eff_w(i,j,p)*
                                R_tot_w(j,p);
360
361                     end
362
363                     T_mean_w(j,p) = mean(Tw_ext_new_w(1:4,j,p));
364                     T_film2_w(j,p) = (T_mean_w(j,p)+T_amb)/2;
365
366                     for i=1:4
367                         nu_air_w(i,j,p)=interp2(air_pressure_prop,
                                air_temperature_prop,air_kinematic_viscosity_prop,
                                P_amb,T_film2_w(j,p),'spline');
368                         Pr_air_w(i,j,p)=interp2(air_pressure_prop,
                                air_temperature_prop,air_prandtl_prop,P_amb,
                                T_film2_w(j,p),'spline');
369                         k_air_w(i,j,p)=interp2(air_pressure_prop,
                                air_temperature_prop,air_conductivity_prop,P_amb,
                                T_film2_w(j,p),'spline');
370                     end
371                 end
372                 q_TOT_w(j,p)=(Tw_ext_w(1,j,p)-T_fluid_w(j,p))/R_tot_w(j,p)+(
                        Tw_ext_w(2,j,p)-T_fluid_w(j,p))/R_tot_w(j,p)+(Tw_ext_w(3,j,
                        p)-T_fluid_w(j,p))/R_tot_w(j,p)+(Tw_ext_w(4,j,p)-T_fluid_w(
                        j,p))/R_tot_w(j,p)...
373                     +(Tw_ext_w(5,j,p)-T_fluid_w(j,p))/R_tot_w(j,p)+(Tw_ext_w(6,
                        j,p)-T_fluid_w(j,p))/R_tot_w(j,p)+(Tw_ext_w(7,j,p)-
                        T_fluid_w(j,p))/R_tot_w(j,p)+(Tw_ext_w(8,j,p)-T_fluid_w
                        (j,p))/R_tot_w(j,p);
374
375                 T_fluid_w(j+1,p)= q_TOT_w(j,p) / (m_fluid_w(p)*cp_fluid_w(j,p))
                         + T_fluid_w(j,p);
376                 P_fluid_w(j+1,p) = P_fluid_w(j,p) - DeltaP_w(j,p);
377                 ent_fluid_w(j+1,p)=interp2(salts_pressure_prop,
                        salts_temperature_prop,salts_enthalpy_prop,P_fluid_w(j+1,p)
                        ,T_fluid_w(j+1,p));
378             end
379         end
380     end
381     error_it=max(max(max(abs(Tw_ext_w(:,:,:)-Tw_ext_old_w(:,:,:)))));
382     error(k)=error_it;
383 end
```

```
384     h_fluid_out_w=ent_fluid_w(29,9);
385     k_mass_w=h_fluid_out_w/h_out_target-1;
386     error_mass_w=100*abs(k_mass_w)
387 end
```

Appendix B

Receiver dynamic model

Listing B.1: Script for the receiver thermal model according to transient conditions. West path case

```
clc
close
clear all
load results1secMarch12h
global T_fluid_ini T_inlet T_wall m_fluid k A_pipe d_int xmesh_aux

%% Radiazione
load q_rad_west
load q_rad_east
t_frame=size(q_rad_west,3);
h_forced=0.1967*w_speed^1.849*ones(4,N,M/2,t_frame);

%% Control system method selection
control_system=input('Insert "1" for the FEED BACK control method, "2" for the FEED FORWARD one:');

%% WEST TRANSIENT
m_fluid_tot_w=ones(1,t_frame);
m_fluid_tot_w(1)=206.5; %206.5 solved as nominal case for March12h
T_out_target=T_fluid_w(end,end,1);
T_fluid_out_w(1)=T_out_target;
error_mass_w(1)=0;
der_error_w(1)=0;
int_error_w=0;
k_mass_w(1)=0;

for k=2:t_frame
    % CONTROL SYSTEM:
    if control_system==1 %FEED BACK CONTROL METHOD
        p1=0.09;
        p2=0.05;
        p3=0;

        if T_fluid_out_w(k-1)<290+273.15
            break
            disp('ALARM: T_fluid_out lower then T_in. System has to be switched off.')
        end
```

```
37          if T_fluid_out_w(k-1)>=580+273.15
38              p1=0.5;
39              p2=0.25;
40          end
41          if T_fluid_out_w(k-1)<580+273.15
42              p1=0.09;
43              p2=0.05;
44          end
45
46          Proportional=p1*k_mass_w(k-1)
47          Derivative=p2*der_error_w(k-1)*sign(k_mass_w(k-1))
48          Integral=p3*int_error_w;
49          m_fluid_tot_w(k)=m_fluid_tot_w(k-1)*(1+p1*k_mass_w(k-1)+p2*der_error_w(k-1)
                *sign(k_mass_w(k-1))+p3*int_error_w);
50
51          if T_fluid_out_w(k-1)<500+273.15
52              m_fluid_tot_w(k)=m_fluid_tot_w(k-1);
53              disp('ALARM: T_fluid_out too low, the flow has to be sent back to the
                    cold tank')
54          end
55
56          disp(['m_fluid_tot_west = ',num2str(m_fluid_tot_w(k)),' kg/s'])
57
58      elseif control_system==2 %FEED FORWARD CONTROL METHOD
59          Irr(k)=mean(mean(q_rad_west(:,:,k)))/1000; %[kW/m2]
60          p1=2;
61          p2=0.5;
62          m_fluid_tot_w(k)=(0.4563*Irr(k)-13.387)*(1+p1*k_mass_w(k-1)+p2*der_error_w(
                k-1)*sign(k_mass_w(k-1)));
63          disp(['m_fluid_tot = ',num2str(m_fluid_tot_w(k)),' kg/s'])
64
65          if T_fluid_out_w(k-1)<500+273.15
66              m_fluid_tot_w(k)=m_fluid_tot_w(k-1);
67              disp('ALARM: T_fluid_out too low, the flow has to be sent back to the
                    cold tank')
68          end
69
70      else
71          disp ('Please select an available control system');
72          break
73      end
74
75      % START TRANSIENT COMPUTATION
76      m_fluid_w(1:9,k)=m_fluid_tot_w(k)/24;
77
78      for p=1:9
79          for j=1:28
80              R_int_w(j,p,k)=R_int_w(j,p,k-1);
81              cp_fluid_w(j,p,k)=cp_fluid_w(j,p,k-1);
82              rho_fluid_w(j,p,k)=rho_fluid_w(j,p,k-1);
83              vel_fluid_w(j,p,k) = m_fluid_w(p,k)/(rho_fluid_w(j,p,k)*A_pipe);
84              for i=1:8
85                  Tw_ext_w(i,j,p,k)=Tw_ext_w(i,j,p,k-1);
86              end
87          end
88      end
89      error_mass_w(k)=100;
90      k_mass_w(k)=0;
91      it(k)=0;
```

```
92      error(k)=100;
93      toll(k)=1e-1;
94      while error(k)>toll
95
96          Tw_ext_w_old=Tw_ext_w;
97
98          %PDEPE solution
99          xmesh_aux=linspace(1,145,253);
100         T_inlet=563.15; %constant
101
102         %initialize T_fluit for PDEPE
103         T_fluid_ini=[];
104         T_fluid_ini=[T_fluid_ini (T_fluid_w(1:end,1,k-1))'];
105         for p=2:9
106             T_fluid_ini=[T_fluid_ini (T_fluid_w(2:end,p,k-1))'];
107         end
108
109         %initialize T_wall for PDEPE
110         for p=1:9
111             for j=1:28
112                 Tw_mean_section(j,p,k)=mean(Tw_ext_w(:,j,p,k));
113             end
114         end
115         Tw_mean=[];
116         for p=1:9
117             Tw_mean=[Tw_mean (Tw_mean_section(1:end,p,k))']; %Twall(1,252)
                    @computed at the middle of each tube section
118         end
119         T_wall(1)=Tw_mean(1);
120         for jj=2:252
121             T_wall(jj)=(Tw_mean(jj)+Tw_mean(jj-1))/2;
122         end
123         T_wall(253)=Tw_mean(end); %T_wall(1,253) @computed at the extreme of each
                tube section
124         m_fluid=m_fluid_w;
125
126         T_fluid_pdepe=real(pde_fluid);
127
128         T_fluid_w(:,:,k)=[T_fluid_pdepe(1:29)' T_fluid_pdepe(29:57)' T_fluid_pdepe
                (57:85)' T_fluid_pdepe(85:113)' T_fluid_pdepe(113:141)' T_fluid_pdepe
                (141:169)' T_fluid_pdepe(169:197)' T_fluid_pdepe(197:225)'
                T_fluid_pdepe(225:253)'];
129         T_fluid_out_w(k)=T_fluid_w(end,end,k);
130
131         %--------------------------%
132         % STEADY-STATE THERMAL MODEL
133         %--------------------------%
134
135         error_it=max(max(max(abs(Tw_ext_w(:,:,:,k)-Tw_ext_w_old(:,:,:,k)))));
136         error(k)=error_it;
137         it(k)=it(k)+1;
138
139     end
140
141     k_mass_w(k)=T_fluid_out_w(k)/T_out_target-1;
142     error_mass_w(k)=100*abs(k_mass_w(k));
143     der_error_w(k)=error_mass_w(k)-error_mass_w(k-1);
144     int_error_w=(int_error_w+sign(k_mass_w(k))*error_mass_w(k)/2+sign(k_mass_w(k-1)
            )*error_mass_w(k-1)/2);
```

```
145
146     T_fluid_out_deg_AUX=T_fluid_out_w(k)-273.15;
147     disp(['T_fluid_out_west = ',num2str(T_fluid_out_deg_AUX),' C'])
148     disp(['Time_solved_west = ',num2str(k),' sec'])
149 end
150
151 %% TANK LEVEL ANALYSIS
152
153 %Whole amount of molten salts produced in the receiver for each second
154 t_frame=650;
155 m_fluid_produced=ones(1,t_frame);
156 for k=1:t_frame
157     if T_fluid_out_w(k)>500+273.15 && T_fluid_out_e(k)>500+273.15
158         m_fluid_produced(k)=m_fluid_tot_w(k)+m_fluid_tot_e(k);
159     elseif T_fluid_out_w(k)>500+273.15
160         m_fluid_produced(k)=m_fluid_tot_w(k);
161     elseif T_fluid_out_e(k)>500+273.15
162         m_fluid_produced(k)=m_fluid_tot_e(k);
163     end
164 end
165
166 %Tank dimension (hot: HOT TANK , cold:COLD TANK)
167 d_tank=23; %[m]
168 h_tank=10; %[m]
169 V_tank=0.25*(pi*d_tank^2)*h_tank; %[m^3]
170 rho_fluid_hot=-0.642*(565+273.15)+2266.3; %fluid density in the hot tank
171 rho_fluid_cold=-0.642*(290+273.15)+2266.3;%fluid density in the cold tank
172
173 %Tank levels
174 level_start_percentage=input('Please insert the percentage of both tank level as
        the starting condition of this analyis [ex: press"60" for 60%]: ');
175 level_start_percentage=50;
176 level_start=h_tank*(level_start_percentage/100);
177 level_cold_percentage(1)=level_start_percentage/100;
178 level_hot_percentage(1)=level_start_percentage/100;
179 level_cold_percentage_noclouds(1)=level_cold_percentage(1);
180 level_hot_percentage_noclouds(1)=level_hot_percentage(1);
181
182 m_salts_required=129.16; %[kg/s]
183 V_salts_in_hot=m_fluid_produced./rho_fluid_hot; %[m3/s]
184 V_salts_out_hot(1:t_frame)=m_salts_required/rho_fluid_hot;
185 V_salts_in_cold(1:t_frame)=m_salts_required/rho_fluid_cold;
186 V_salts_out_cold=m_fluid_produced./rho_fluid_cold;
187
188 V_hot_tank(1)=level_start*0.25*(pi*d_tank^2);
189 V_cold_tank(1)=level_start*0.25*(pi*d_tank^2);
190 V_hot_tank_noclouds(1)=V_hot_tank(1);
191 V_cold_tank_noclouds(1)=V_cold_tank(1);
192 V_salts_in_hot_noclouds=m_fluid_produced(1)/rho_fluid_hot;
193 V_salts_out_hot_noclouds=m_salts_required/rho_fluid_hot;
194 V_salts_in_cold_noclouds=m_salts_required/rho_fluid_cold;
195 V_salts_out_cold_noclouds=m_fluid_produced(1)/rho_fluid_cold;
196
197 for k=2:t_frame
198     V_hot_tank(k)=V_hot_tank(k-1)+V_salts_in_hot(k)-V_salts_out_hot(k);
199     V_cold_tank(k)=V_cold_tank(k-1)+V_salts_in_cold(k)-V_salts_out_cold(k);
200     level_cold_percentage(k)=V_cold_tank(k)/V_tank;
201     level_hot_percentage(k)=V_hot_tank(k)/V_tank;
202
```

```
203     V_hot_tank_noclouds(k)=V_hot_tank_noclouds(k-1)+V_salts_in_hot_noclouds-
            V_salts_out_hot_noclouds;
204     V_cold_tank_noclouds(k)=V_cold_tank_noclouds(k-1)+V_salts_in_cold_noclouds-
            V_salts_out_cold_noclouds;
205     level_cold_percentage_noclouds(k)=V_cold_tank_noclouds(k)/V_tank;
206     level_hot_percentage_noclouds(k)=V_hot_tank_noclouds(k)/V_tank;
207 end
208
209 plot([1:t_frame], m_fluid_produced,'b',[1:t_frame], ones(t_frame)*m_salts_required,
        'r')
210 xlabel('Time [s]');
211 ylabel('HTF mass flow rate [kg/s]');
212 legend('HTF produced by receiver', 'HTF required by power block');
213 grid on
214
215 plot([1:t_frame],100*level_hot_percentage,'r-',[1:t_frame],100*
        level_cold_percentage,'b-',[1:t_frame],100*level_hot_percentage_noclouds,'r--'
        ,[1:t_frame],100*level_cold_percentage_noclouds,'b--')
216 xlabel('Time [s]');
217 ylabel('Tank level [%]');
218 legend('Hot tank level', 'Cold tank level','Hot tank level without clouds','Cold
        tank level without clouds');
219 grid on
```

List of Figures

Acronyms

CSP	Concentrated Solar Power
RES	Renewable Energy Sources
PDC	Parabolic Dish Collector
LFC	Linear Fresnell collectors Collector
CTS	Central Tower Systems
PTC	Parabolic Through Collectors
USA	Unites State of America
DoE	Department of Energy (of the USA)
HRSG	Heat Recovery Steam Generator
CRTF	Central Receiver Test Facility
SEDC	Solar Energy Development Center
DNI	Direct Normal Irradiation
FWH	Feed Water Heater
HTF	Heat Thermal Fluid
STP	Standard Temperature and Pressure
HX	Heat Exchanger
ASME	American Society of Mechanical Engineers
EES	Engineering Equation Software
HP	High Pressure
ACC	Air Cooled Condenser

CFD	Computational Fluid Dynamics
PDE	Partial Differential Equation
PDEPE	Partial Differential Equation Parabolic and Elliptic
PID	Proportional Integral Derivative (controller)
TIT	Turbine Inlet Temperature
SH	Superheated (steam cycle)
RH	Reheated (steam cycle)
STR	Solar Tower Receiver
HRSG	Heat Recovery Steam Generation
SM	Solar Multiple

Bibliography

References quoted in the text

Publications and manuals

[1] *A User's Manual for DELSOL3: A Computer Code for Calculating the Optical Performance and Optimal System Design for Solar Thermal Central Receiver Plants*. 1986 (cit. on p. 18).

[2] Abengoa. *PS10, the first solar power tower worldwide report*. Technical report. Abengoa Solar, S.A.,Seville - Spain, 2007 (cit. on pp. 9, 10).

[3] Abengoa. *PS20, the largest solar power tower worldwide*. Technical report. Abengoa Solar, S.A.,Seville - Spain, 2009 (cit. on p. 9).

[4] International Renewable Energy Agency, ed. *Renewable Technologies: Cost Analysis Series - Concentrating Solar Power. Technical Report 2*. 2012 (cit. on p. 7).

[5] Kyoungkwan Ahn and Shinichi Yokota. "Intelligent switching control of pneumatic actuator using on/off solenoid valves". In: *Mechatronics* 15.6 (2005), pp. 683–702 (cit. on p. 34).

[6] M Araki. "PID control". In: *Control Systems, Robotics and Automation: System Analysis and Control: Classical Approaches II, Unbehauen, H.(Ed.). EOLSS Publishers Co. Ltd., Oxford, UK., ISBN-13: 9781848265912* (2009), pp. 58–79 (cit. on p. 86).

[7] G. Augsburger. "Thermo-economic optimisation of large solar tower power plants". PHD Thesis. Ecole Polythechnique Fédéral de Lausanne, 2013 (cit. on pp. 8, 11).

[8] BrightSource. *Coalinga Chevron/BrightSource Solar-to-Steam Demonstration Facility*. Technical report. BrightSource Energy, Oakland - California - USA, 2011 (cit. on p. 9).

[9] B. Timothy e C. Judith. "Characteristics of small tropical cumulus clouds and their impact on the environment". In: *Journal of Geophysical Research*. 1998, pp. 28,753–28,767 (cit. on p. 22).

[10] Enrico Casalini. "Storage system for wind power enhancement: modelling of the application on two existing plants". Master Thesis-Energy Engineering. Politecnico di Milano (cit. on pp. 2, 8).

[11] Davide Castelli. "Sviluppo del modello termico di un ricevitore solare a torre con fluido termovettore monofase". Tesi di Laurea Magistrale-Ingegneria Energetica. Politecnico di Milano (cit. on pp. 43, 70–72).

[12] Ali Chaibakhsh and Ali Ghaffari. "Steam turbine model". In: *Simulation Modelling Practice and Theory* 16.9 (2008), pp. 1145 –1162. ISSN: 1569-190X. URL: http://www.sciencedirect.com/science/article/pii/S1569190X08001196 (cit. on p. 27).

[13] Stuart W. Churchill and Humbert H.S. Chu. "Correlating equations for laminar and turbulent free convection from a horizontal cylinder". In: *International Journal of Heat and Mass Transfer* 18.9 (1975), pp. 1049 –1053. ISSN: 0017-9310. URL: http://www.sciencedirect.com/science/article/pii/0017931075902227 (cit. on p. 55).

[14] "Concentratig Solar Power - Global Outlook 09 - Why Renewable Energy is Hot. Technical Report". In: *SolarPACES* (2009) (cit. on p. 7).

[15] David H Cooke. "Modeling of off-design multistage turbine pressures by Stodola's ellipse". In: *Energy Incorporated PEPSE User's Group Meeting, Richmond, VA, Nov*. 1983, pp. 2–3 (cit. on p. 34).

[16] L.F. Drbal et al. *Power Plant Engineering*. IFAC proceedings series. Springer, 1996. ISBN: 9780412064012. URL: https://books.google.es/books?id=4ewKE8MZAZIC (cit. on p. 108).

[17] ESolar. *Sierra SunTower*. Technical report. ESolar Avenue, Burbank - California - USA, 2009 (cit. on p. 9).

[18] K. Hoopes B. Choi N. Kuek F. Crespi D. Sanchez, ed. *The Conductance Ratio Method For Off-Design Heat Exchanger modeling and its impact On an sCO_2 recompression cycle*. 2017 (cit. on p. 27).

[19] Paolo Zani Francesco Crespi. "Best aiming strategy definition for off-design conditions due to passage of clouds in a Solar Tower". Master Thesis-Energy Engineering. Politecnico di Milano (cit. on pp. 2, 5, 18).

[20] D. Alpert G. Kolb and C. Lopez. “Insights from the operation of Solar One and their implications for future central receiver plants”. In: *Solar Energy*. 1991, pp. 39–47 (cit. on p. 8).

[21] Randall S. Gemmen. “Dynamic Modeling of Fuel Cells”. In: *Modeling Solid Oxide Fuel Cells: Methods, Procedures and Techniques*. Ed. by Roberto Bove and Stefano Ubertini. Dordrecht: Springer Netherlands, 2008, pp. 269–322 (cit. on p. 29).

[22] Paolo de Giorgi. “Software analysis and development for aiming strategies optimization in Solar Tower power plants”. Master Thesis-Energy Engineering. Politecnico di Milano, 2013 (cit. on p. 18).

[23] T. Teolan e H. Maire. *Dynamic properties of clouds Cumulus humilis and Cumulus fractus*. 2011 (cit. on p. 22).

[24] Kon Hisashi. *he Horizontal Movement Speed of Cumulus Clouds in a Shear Flow: A Two-Dimensional Numerical Experiment*. Hokkaido University, 1981 (cit. on p. 22).

[25] M. Thomas K. Gregory H. Clifford and G. Jesse. “Power Tower Technology Roadmap and Cost Reduction Plan”. In: *SANDIA Report* (cit. on p. 54).

[26] Edward Wilson Kimbark. *Power system stability*. Vol. 1. John Wiley & Sons, 1995 (cit. on p. 33).

[27] K.S. *Solar Energy Engineering - Processes and Systems*. Academic Press. 2009 (cit. on p. 8).

[28] G. Lozza and S.E. Esculapio. *Turbine a Gas e Cicli Combinati:* Esculapio, 2016. ISBN: 9788874889341. URL: https://books.google.es/books?id=nqxyCwAAQBAJ (cit. on p. 108).

[29] V. M. Manuel. *Analisis de las direcciones de los vientos en Andalucia*. 1998 (cit. on p. 20).

[30] NREL. *SunShot Vision Study*. Technical report. National Renewable Energy Laboratory, U.S. Department of Energy, Office of Energy Efficiency and Renewable Energy, 2012 (cit. on p. 8).

[31] Izuchukwu F. Okafor, Jaco Dirker, and Josua P. Meyer. “Influence of circumferential solar heat flux distribution on the heat transfer coefficients of linear Fresnel collector absorber tubes”. In: *Solar Energy* 107 (2014), pp. 381 –397. ISSN: 0038-092X. URL: http://www.sciencedirect.com/science/article/pii/S0038092X14002394 (cit. on p. 44).

[32] Paolo Pini. "Influence of cloud passing on the dynamic thermal performance of central receivers in tower CSP plants". Politecnico di Milano (cit. on pp. 26, 51).

[33] Altes Buch Queralt. "Dynamic modeling of a steam Rankine Cycle for concentrated solar power applications". Licenciate Thesis-Industrial Engineering. University of Liege (cit. on p. 28).

[34] María Reyes Rodríguez-Sánchez et al. "Comparison of simplified heat transfer models and {CFD} simulations for molten salt external receiver". In: *Applied Thermal Engineering* 73.1 (2014), pp. 993 –1005. ISSN: 1359-4311. URL: http://www.sciencedirect.com/science/article/pii/S1359431114007686 (cit. on pp. 70, 71).

[35] M.R. Rodríguez-Sánchez et al. "New Designs of Molten-salt Tubular-receiver for Solar Power Tower". In: *Energy Procedia* 49 (2014), pp. 504 –513. ISSN: 1876-6102. URL: http://www.sciencedirect.com/science/article/pii/S1876610214005086 (cit. on p. 72).

[36] M.R. Rodríguez-Sánchez et al. "Thermal design guidelines of solar power towers". In: *Applied Thermal Engineering* 63.1 (2014), pp. 428 –438. ISSN: 1359-4311. URL: http://www.sciencedirect.com/science/article/pii/S1359431113008028 (cit. on pp. 43, 70–72).

[37] M.R. Rodriguez-Sanchez, A. Sanchez-Gonzalez, and D. Santana. "Revised receiver efficiency of molten-salt power towers". In: *Renewable and Sustainable Energy Reviews* 52 (2015), pp. 1331 –1339. ISSN: 1364-0321. URL: http://www.sciencedirect.com/science/article/pii/S1364032115008461 (cit. on p. 72).

[38] Javier Samanes and Javier Garcia-Barberena. "A model for the transient performance simulation of solar cavity receivers". In: *Solar Energy* 110 (2014), pp. 789 –806. ISSN: 0038-0092. URL: http://www.sciencedirect.com/science/article/pii/S0038092X14005015 (cit. on pp. 26, 45).

[39] Peter W Sauer and MA Pai. "Power system dynamics and stability". In: *Urbana* (1998) (cit. on p. 32).

[40] Solugas. "Solar Up-scale Gas Turbine System". In: (2012) (cit. on p. 9).

[41] M Swierczynski et al. "Overview of the energy storage systems for wind power integration enhancement". In: *2010 IEEE International Symposium on Industrial Electronics*. IEEE. 2010, pp. 3749–3756 (cit. on p. 2).

[42] Institute of Technical Thermodynamics. *Concentrating Solar Power for the Mediterranean Region*. Technical report. Deutsches Zentrum für Luft- und Raumfahrt e.V. (DLR) - Stuttgart - Germany, 2005 (cit. on pp. 9, 12).

[43] Monika Topel. "Steam turbine thermal modeling for improved transient operation". Licenciate Thesis-Industrial Engineering. KTH Royal Institute of Technology, 2014 (cit. on pp. 27, 32).

[44] Torresol. *Gemasolar, the world's first solar thermal plant consisting of central tower technology and salts receiver*. Technical report. Torresol Energy Investments,, S.A., Fuentes de Andalucía - Seville - Spain, 2011 (cit. on pp. 9, 16, 20, 108, 117).

[45] Zhen Yang and Suresh V. Garimella. "Thermal analysis of solar thermal energy storage in a molten-salt thermocline". In: *Solar Energy* 84.6 (2010), pp. 974 –985. ISSN: 0038-092X. URL: http://www.sciencedirect.com/science/article/pii/S0038092X10001118 (cit. on p. 78).

Online resources

[46] *ASME section I and section VIII fundamentals*. 2012. URL: http://www.pdhonline.com/courses/m398/m398content.pdf (cit. on pp. 32, 43).

[47] *Calculate wind profile according to Hellman's equation*. URL: https://artax.karlin.mff.cuni.cz/r-help/library/bReeze/html/profile.html (cit. on p. 21).

[48] *Concentrated Solar Power (CSP) - How it Works*. 2013. URL: http://www.helioscsp.com/ (cit. on pp. 9–11).

[49] *Concentrating solar power from research to implementation*. 2014. URL: http://ec.europa.eu (cit. on p. 17).

[50] *Danger of solidification in the molten salt for CSP*. 2014. URL: http://www.energynews.es/english/peligro-de-solidificaci-n-en-las-sales-fundidas-para-csp-1357109850/ (cit. on p. 42).

[51] *EES - Engineering Equation Software*. URL: http://www.fchart.com/ees/ (cit. on p. 42).

[52] *GeoModelSolar, world map of direct normal irradiation*. 2014. URL: http://solargis.info (cit. on p. 12).

[53] *Pdepe function*. URL: https://it.mathworks.com/help/matlab/ref/pdepe.html (cit. on p. 79).

[54] *Solar energy overview*. 2016. URL: http://www.solar-tower.org.uk/quick-start.php (cit. on p. 7).

[55] *South Africa Solar plants*. 2014. URL: http://www.abengoasolar.com/web/en/plantas_solares/plantas_propias/sudafrica/#seccion_2 (cit. on p. 9).

[56] *South Africa Solar plants*. 2014. URL: http://www.abengoasolar.com/web/en/plantas_solares/plantas_propias/sudafrica/#seccion_2 (cit. on p. 9).

[57] *Wind profile chart*. 2014. URL: http://aviador.es (cit. on pp. 20, 21).

[58] *XSteam tool*. URL: https://it.mathworks.com/matlabcentral/fileexchange/9817-x-steam--thermodynamic-properties-of-water-and-steam (cit. on p. 108).

B.1 Other material

Publications and manuals

[59] E. Britannica. *Different types of clouds form at different heights*. 2012.

[60] José M. Rodríguez et al. "Techno-economic assessment of thermal energy storage solutions for a 1 MWe CSP-ORC power plant". In: *Solar Energy* 140 (2016), pp. 206 –218. ISSN: 0038-092X. URL: http://www.sciencedirect.com/science/article/pii/S0038092X16305230.

[61] R.Penrose. "Meteorology at the Millennium". In: *Academic Press* (2002).